AFRL-ML-WP-TR-1998-4128
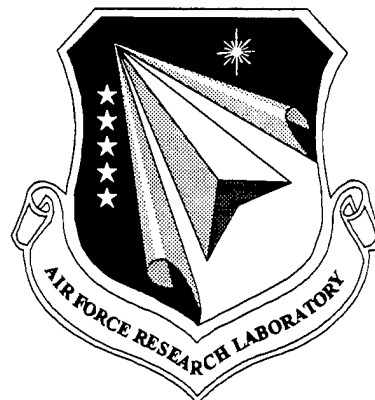
LARGE AREA COMPOSITE INSPECTION SYSTEM

Thomas E. Drake

Lockheed Martin Tactical Aircraft Systems
PO Box 748 MZ 6852
Fort Worth TX 76101-0748

JUNE 1998

FINAL REPORT FOR PERIOD OCTOBER 1992 – JUNE 1998

19980915 129

Approved for public release; distribution unlimited

This material may be reproduced by or for the U.S. Government pursuant to the copyright license under the clause at DFARS 252.227-7013 (October 1988)

MATERIALS & MANUFACTURING DIRECTORATE
AIR FORCE RESEARCH LABORATORY
AIR FORCE MATERIEL COMMAND
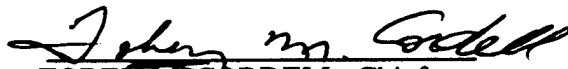WRIGHT-PATTERSON AIR FORCE BASE, OH 45433-7734

NOTICE

WHEN GOVERNMENT DRAWINGS, SPECIFICATIONS, OR OTHER DATA ARE USED FOR ANY PURPOSE OTHER THAN IN CONNECTION WITH A DEFINITELY GOVERNMENT-RELATED PROCUREMENT, THE UNITED STATES GOVERNMENT INCURS NO RESPONSIBILITY OR ANY OBLIGATION WHATSOEVER. THE FACT THAT THE GOVERNMENT MAY HAVE FORMULATED OR IN ANY WAY SUPPLIED THE SAID DRAWINGS, SPECIFICATIONS, OR OTHER DATA, IS NOT TO BE REGARDED BY IMPLICATION OR OTHERWISE IN ANY MANNER CONSTRUED, AS LICENSING THE HOLDER OR ANY OTHER PERSON OR CORPORATION, OR AS CONVEYING ANY RIGHTS OR PERMISSION TO MANUFACTURE, USE, OR SELL ANY PATENTED INVENTION THAT MAY IN ANY WAY BE RELATED THERETO.

THIS REPORT IS RELEASABLE TO THE NATIONAL TECHNICAL INFORMATION SERVICE (NTIS). AT NTIS, IT WILL BE AVAILABLE TO THE GENERAL PUBLIC, INCLUDING FOREIGN NATIONS.

THIS TECHNICAL REPORT HAS BEEN REVIEWED AND IS APPROVED FOR PUBLICATION.

CURTIS J. FIEDLER, Project Engineer
Nondestructive Evaluations Branch
Metals, Ceramics & NDE Division

TOBEY M. CORDELL, Chief
Nondestructive Evaluations Branch
Metals, Ceramics & NDE Division

GERALD J. PETRAK, Acting Asst Chief
Metals, Ceramics & NDE Division
Materials & Manufacturing Directorate

IF YOUR ADDRESS HAS CHANGED, IF YOU WISH TO BE REMOVED FROM OUR MAILING LIST, OR IF THE ADDRESSEE IS NO LONGER EMPLOYED BY YOUR ORGANIZATION, PLEASE NOTIFY, AFRL/MLLP, WRIGHT-PATTERSON AFB OH 45433-7817 AT 59819 TO HELP US MAINTAIN A CURRENT MAILING LIST.

COPIES OF THIS REPORT SHOULD NOT BE RETURNED UNLESS RETURN IS REQUIRED BY SECURITY CONSIDERATIONS, CONTRACTUAL OBLIGATIONS, OR NOTICE ON A SPECIFIC DOCUMENT.

REPORT DOCUMENTATION PAGE	FORM APPROVED OMB NO. 0704-0188

Public reporting burden for this collection of information is estimated to average 1 hour per response, including the time for reviewing instructions, searching existing data sources, gathering and maintaining the data needed, and completing and reviewing the collection of information. Send comments regarding this burden estimate or any other aspect of this collection of information, including suggestions for reducing this burden, to Washington Headquarters Services, Directorate for Information Operations and Reports, 1215 Jefferson Davis Highway, Suite 1204, Arlington, VA 22202-4302 and to the Office of Management and Budget, Paperwork Reduction Project (0704-0188), Washington, DC 20503.

1. AGENCY USE ONLY (Leave blank)	2. REPORT DATE 8 June 1998	3. REPORT TYPE AND DATES COVERED Final Rep from Oct 1992 to June 1998

4. TITLE AND SUBTITLE Large Area Composite Inspection System	5. FUNDING NUMBERS C - F33615-92-C-5981 PE - 63112F PR - 3153 TA - 00 WU - 12
6. AUTHOR(S) Thomas E. Drake	

7. PERFORMING ORGANIZATION NAMES(S) AND ADDRESS(ES) Lockheed Martin Tactical Aircraft Systems P O BOX 748, MZ 6852 Fort Worth, TX 76101-0748	8. PERFORMING ORGANIZATION REPORT NUMBER FZM-8250-19

9. SPONSORING/MONITORING AGENCY NAMES(ES) AND ADDRESS(ES) Materials & Manufacturing Directorate Air Force Research Laboratory Air Force Materiel Command Wright-Patterson Air Force Base, OH 45433-7734 POC: Curtis J. Fiedler, AFRL/MLLP, 937-255-9797	10. SPONSORING/MONITORING AGENCY REPORT NUMBER AFRL-ML-WP-TR-1998-4128

11. SUPPLEMENTARY NOTES

12a. DISTRIBUTION/AVAILABILITY STATEMENT Approved for public release; distribution is unlimited	12b. DISTRIBUTION CODE

13. ABSTRACT (Maximum 200 words)

The Large Area Composite Inspection System (LACIS) successfully proved that Laser Ultrasonic Testing (UT) will meet the future needs of both Air Logisitics Centers (ALC's) and aerospace contractors. Many significant advances in laser ultrasonic technology were demonstrated with the prototype system. Highlights of the program accomplishments are: large area complex composite structures were tested with Laser UT for the first time; rapid and accurate optical scanning was achieved; improved defect detection and signal-to-noise ratio was accomplished; and, advanced data analysis capabilities were demonstrated. Laser UT reduceds the capital investment and lowers the labor cost of testing composite structures. The LACIS program conclusively demonstrated the superiority of Laser UT for testing large complex aerospace composite materials. Laser UT will be an important manufacturing and in-service method for Quality Assurance of next generation of advanced aircraft.

14. SUBJECT TERMS Laser Ultrasonic Testing, Large Area Composite Inspection, Data Acquisition			15. NUMBER OF PAGES 160
			16. PRICE CODE

17. SECURITY CLASSIFICATION OF REPORT Unclassified	18. SECURITY CLASSIFICATION OF THIS PAGE Unclassified	19. SECURITY CLASSIFICATION OF ABSTRACT Unclassified	20. LIMITATION OF ABSTRACT SAR

NSN 7540-01-280-5500   COMPUTER GENERATED

STANDARD FORM 298 (Rev. 2-89)
Prescribed by ANSI Std. Z39-18
298-102

TABLE OF CONTENTS

LIST OF FIGURES

1.0 EXECUTIVE SUMMARY

The Large Area Composite Inspection System (LACIS) program was an Air Force Wright Laboratory sponsored research and development effort for advancing the state-of-the-art in laser ultrasonic testing (Laser UT) of complex composite aerospace structures. This final report describes the work performed by Lockheed Martin Tactical Aircraft System (LMTAS) in Fort Worth, Texas under the direction of Thomas E. Drake with the oversight of Dr. Curtis J. Fiedler of the Non Destructive Evaluation (NDE) Branch, Wright Laboratory Materials Directorate.

The long-term objective of this research is to improve the quality and lower the cost of testing composite aircraft structures. Specifically, the approach was to demonstrate the ability of a Laser UT system to test large aerospace composite structures more rapidly than conventional automated ultrasonic systems while achieving equivalent or superior defect detection sensitivity. The LACIS program successfully proved that Laser UT will meet the future needs of both Air Logistics Centers (ALC) and aerospace contractors. Many significant advances in laser ultrasonic technology were demonstrated with the prototype system. Highlights of the program accomplishments are summarized as follows:

- **First to Test Large Area Complex Composite Structures with Laser UT**- This program was the first to test a wide variety of large area composite structures and materials using Laser UT. As part of the system development process, system performance evaluation, and program technology transition, many different types of composite structures and materials were inspected. Tests on composite structures provided by programs such as the F-16, F-22, and Joint Strike Fighter (JSF) proved that Laser UT: 1) provides at least an **order of magnitude savings** in inspection time/cost over conventional automated techniques, 2) has equivalent or superior defect detection sensitivity compared to conventional automated techniques, and 3) is a practical technology for both factory and depot environments. During the testing phase of the program one particular example truly established the credibility of the technology. The time required to test an F-22 inlet section was reduced from 24 hours with our conventional production system to about 2 hours with the Laser UT system. This order of magnitude decrease in inspection time, when combined with the projected growth in composite usage (Figure 1-1), will save hundreds of millions of dollars in inspection costs and reduce the need for buying additional conventional inspection units.

- **Rapid and Accurate Optical Scanning** - The LACIS development system successfully scanned composite structures at rates as high as **100 ft.^{2}/hr.** All testing was performed

without the use of any surface coatings to enhance or modify system performance. This system will automatically adjust to the changing needs of a dark bare composite or a bright "high-gloss" painted material. A "fire on target" scanning technique was implemented so that the lasers fire and the system acquires data over a pre-calculated grid which covers the target. This provides uniform scan coverage of complex contoured structures.

- **Improved Defect Detection and Signal-to-Noise Ratio** - Many design features significantly increased the system sensitivity and signal-to-noise ratio (SNR) and improved the system defect detection capability. A large aperture collector and high power pulsed laser increased the detection light collection efficiency over previous generation systems. Low-noise optical detectors were designed to handle the increased amount of detection light and performed at theoretical limits. A custom dual-differential confocal Fabry-Perot interferometer was designed to remove common-mode noise. This advancement allows the use of all the detection light collected by the system, **improving defect detection sensitivity by a factor of 10 over previous designs**.

- **Advanced Data Analysis Capabilities** - The LACIS development software demonstrated full digital acquisition and storage of all data waveforms with an interactive graphical user interface. Typical ultrasonic A-scan, B-scan, and C-scan representations were incorporated into the software. A unique powerful analysis tool, called **slice imaging** was developed in which the user can peel away layers of the part to reveal subtle features. Because all waveform data is retained, the user can apply any number of C-scan extraction algorithms after the scan is complete without loss of information. This flexibility virtually eliminates test-specific setup procedures and allows the application of more powerful analysis techniques for improved defect detection.

Laser UT will reduce the capital investment and lower the labor cost of testing composite structures. Conventional UT systems cost between $500K and $3M depending on the size and sophistication of the contour following mechanism. Laser UT systems are estimated to cost between $1M and $4M depending on the inspection envelope and computational capabilities. Thus, the capital investment is about the same for the two technologies but the tremendous capacity improvement (10x) provided by the Laser UT system makes it a superior return-on-investment.

Figure 1-1 shows an example of the projected increase in composite NDE workload at LMTAS over the next few years. This tremendous growth is driven by the anticipated production of advanced fighters which will contain large composite structures.

COMPOSITE NDE WORKLOAD
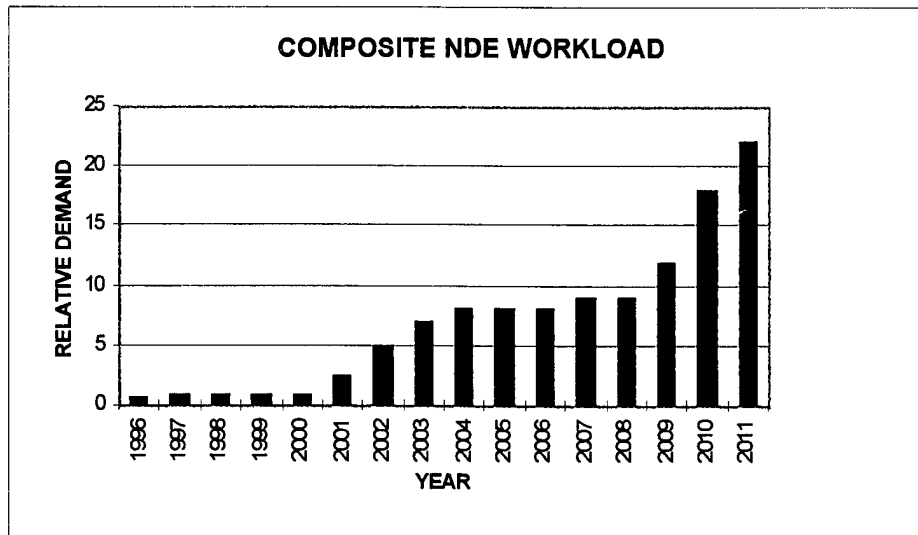
Figure 1-1 Current NDE methods may not meet future workloads.

It would be costly from both a capital investment and labor perspective to apply current conventional approaches to meet this future demand. With its increased speed, a single laser UT system will offset the need for multiple conventional systems. Another critical problem is in-service testing, an almost impossible to perform with conventional systems due to the extreme requirements for part registration and exact contour following procedures. **Laser UT may be the only cost effective way for ALC's to support advanced composite aircraft.** Laser UT will allow the Air Force to use defense contractor's Laser UT data as a baseline for comparison throughout the life of the structure as periodic evaluations are conducted with similar systems installed at the ALC's

The LACIS program conclusively demonstrated the superiority of Laser UT for testing large complex aerospace composite materials. Laser UT will be an important manufacturing and in-service method for the Quality Assurance of next generation advanced aircraft. Both the F22 and the JSF programs will benefit from the high-quality and low-cost capabilities of Laser UT. DoD and industry will realize cost savings and improved products due to this effort. Also of note is the near-term potential of even greater advances of both inspection speed and signal quality. This work will ensure Laser UT as a pervasive technology throughout DoD and industry in the next few years.

2.0 PROGRAM OVERVIEW

2.1 BACKGROUND AND BASIC THEORY

The Large Area Composite Inspection System (LACIS) program was initiated in October 1992 as an Air Force Wright Laboratory (WL/MLLP) research and development contract to advance laser ultrasonic testing (Laser UT) technology. Previous Lockheed Martin Tactical Aircraft Systems (LMTAS) prototypes had demonstrated the tremendous potential of this novel non-destructive evaluation (NDE) method. The LACIS objectives were to significantly improve the prototype and demonstrate the performance advantages of Laser UT compared to conventional UT for testing large complex composite structures. Implicit in this objective was the requirement that Laser UT results must be equivalent or superior to current conventional UT systems.

Conventional UT systems suffer from several limitations that have motivated the development of alternative approaches:

- Undesirable water couplants.
- Slow contour following manipulators.
- Expensive part fixtures.
- Labor intensive part setup procedures.
- Two-side access is often necessary.
- In-service testing of assembled vehicles may not be possible.
- Results can be operator dependent due to critical setup procedures.

Laser UT was conceived to address each of these limitations because of the explosive growth of composite usage anticipated in the next decade (Figure 1-1). The key benefits are:

- Non-contact (no water couplants).
- Fast optical scanning without contour descriptions.
- Inexpensive part fixtures.
- Simple part setup procedures.
- Only single-side is required.
- In-service testing is just as easy as component testing.
- Less operator dependence due to relaxed setup requirements.

Laser UT works by replacing the water-coupled transducers, used by conventional systems, with laser-based components. Ultrasound is induced in the composite material by the absorption of energy from a pulsed "generation" laser. This process is called thermoelastic generation and

4

essentially makes the composite surface the transducer. Thus, the induced ultrasound will propagate normal to the surface independent of the incident angle of the generation laser. A second "detection" laser beam is used to monitor the surface vibrations caused by the ultrasound. These vibrations can be extracted from the detection laser and converted into standard ultrasonic signals with an interferometer and high-speed data acquisition system. A fast optical scanner, under computer control, is used to index the two laser beams over the composite surface to produce standard C-scan images as shown schematically in Figure 2-1.
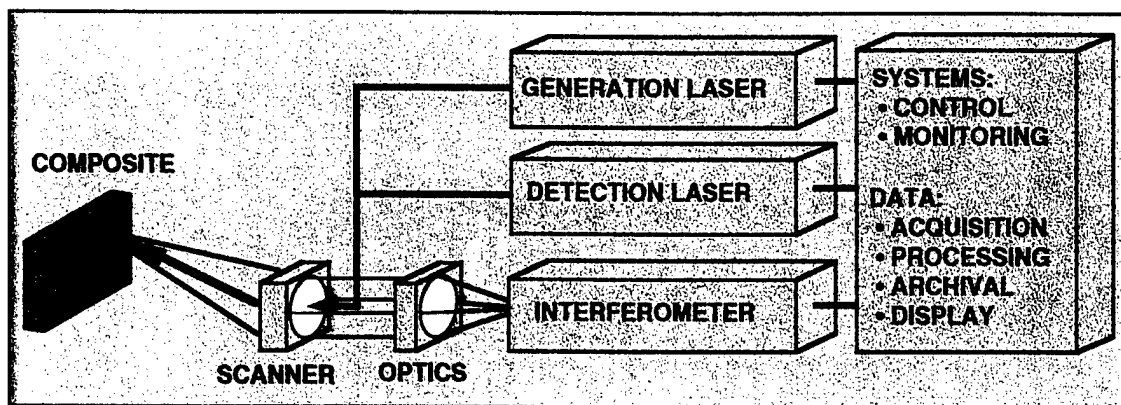
Figure 2-1 Basic components of a Laser UT system.

The obvious advantage that Laser UT offers is the ability to rapidly test a very complex contoured composite part without any prior descriptions of the surface shape. This is the single most difficult process for conventional systems; first determining the part shape, and second actually following that shape in a rapid and repeatable way. Laser UT provides the very same ultrasonic data that a conventional system does but with less time and labor expended.

It is important to understand that Laser UT is not a new testing method (it is still ultrasonics), but instead a faster and better way to perform ultrasonic testing of composite materials. No additional operator certification will be required beyond basic training with the machine because the data is interpreted in the same manner. This issue will be critical for the acceptance of Laser UT results because most facilities already have qualified personnel to operate and interpret UT data.

2.2 APPROACH

The prototype LACIS was designed, assembled, and tested by the LMTAS Laser UT team of engineers, scientists, and technical staff. This required the integration of state-of-the-art laser, optical, mechanical, electrical, and computational technologies into a unified design. Figure 2-2 shows an early version of the prototype with members of the development team. The final proto-type was a fully-functional inspection system capable of rapidly testing a broad range of compos-ite structures ten-times faster than conventional methods.
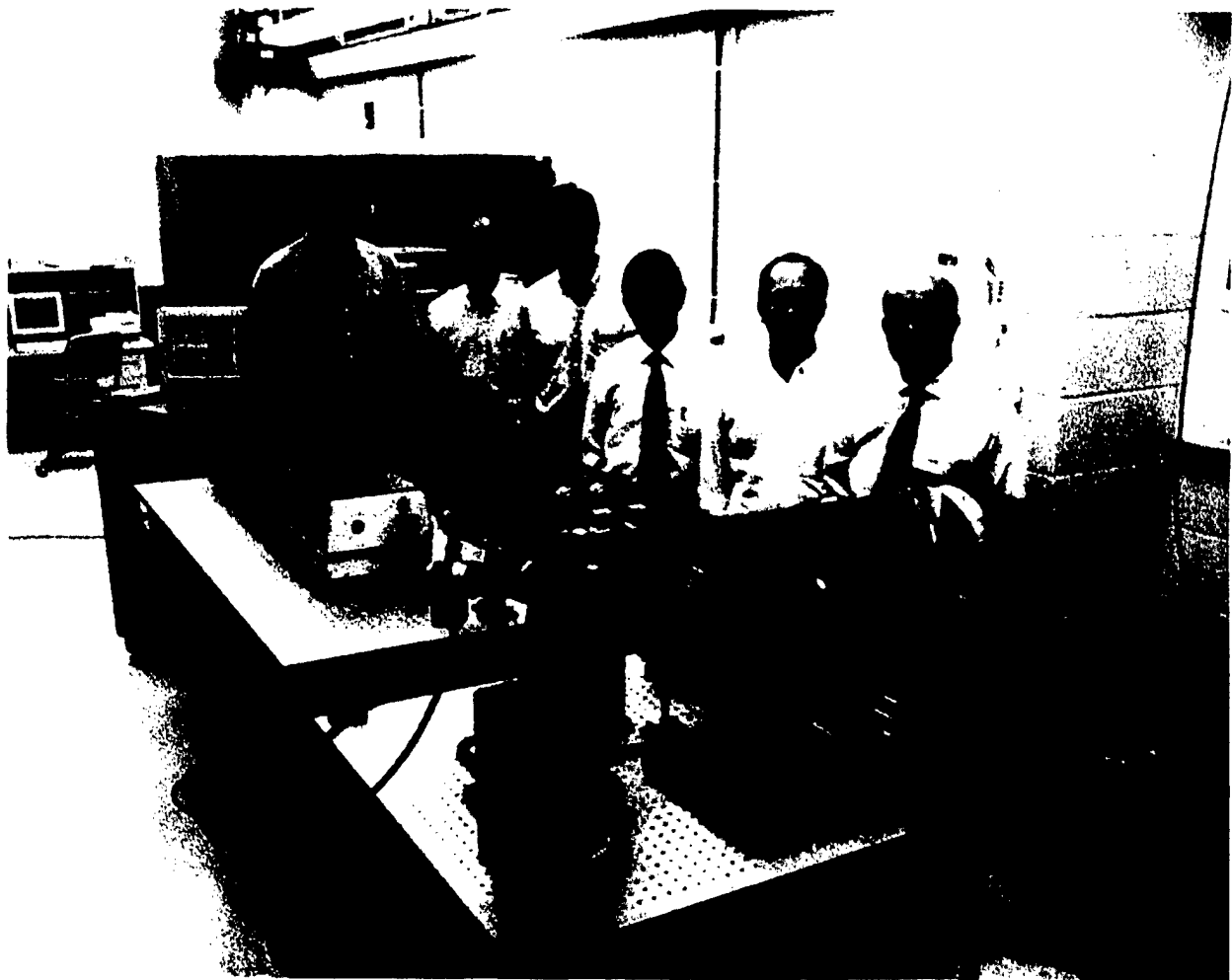
Figure 2-2 Photograph of early prototype with LMTAS Laser UT development team.

The LMTAS Laser UT development team shown above in Figure 2-2 are from left to right:

- Mark Osterkamp   Software, data acquisition, and computational methods.
- S.Y. Chuang   Physics, optical scanning methods.
- Brian Head   Electrical technician.
- Francis Chang   Physics, NDE Group Chief.
- Ken Yawn   Physics, composite manufacturing technologies.
- Tommy Drake   Engineering/Physics, NDE, laser technologies.

The performance of the system was evaluated on dozens of advanced composite structures representative of current and next-generation fighter aircraft. These efforts provided essential feedback that allowed continual system improvements during the program. As an example, the surface condition of the composite was determined to play a significant role in the performance of the system. Instead of requesting that the composite designers and manufacturers meet our preferred conditions, we improved the dynamic range of the system to meet their products. The LACIS program greatly benefited from the fact that the Laser UT system was designed inside a company that also manufactures composite structures. This provided a unique opportunity to evaluate the system performance with a large range of materials and configurations concurrent with the development efforts.

The prototype system was not intended to demonstrate the engineering of a "hardened" system, but instead prove the concept of how Laser UT systems would need to be engineered to solve realistic NDE problems for both manufacturing and in-service environments. To this end the system was extremely successful and demonstrated all of the fundamental features necessary to construct a commercial system.

2.3 TESTING

Laser UT results are material dependent. Generally, the most important issue that determines effectiveness is the type and condition of the composite surface. For the best results, the surface should have an optically opaque layer of organic material with a thickness of a at least a few thousandths of an inch. This provides sufficient material for the absorption of the CO_2 laser energy which enhances the thermoelastic generation of ultrasound. Almost all composite materials meet this criteria. Some materials are more efficient for laser generation of ultrasound than others, but most work acceptably well. Defect detection sensitivity is higher for materials with good generation efficiencies. Almost all materials evaluated could be tested up to 0.5 inches thick and in one case a 1.6 inch thick composite gave excellent results. Thicker parts were also evaluated with varying results.

The optical (visible to near infrared region) characteristics of the materials are generally less of a concern due to the large dynamic range designed into the system. An optically diffuse surface is ideal, but many components were tested with high-gloss surface conditions. The only essential requirement is that the surface not be both glossy and optically transparent. This condition can create distorted signals due to the detection system observing the ultrasound from the exterior of the part and the interior simultaneously. This is a rare occurrence, and is easily corrected with a slight buffing of the surface with a light abrasive.

Shown below in Figure 2-3 is a photograph of a very complex composite part tested with the system. This is an inlet structure from the F-22 which is about 40" tall and 40" wide and is an excellent example of the capabilities of the Laser UT system. It varies in thickness from about 0.2 inches down to 0.15 inches with short ply transition regions from one thickness to another. The initial testing time, listed in Table 2-1, was reduced from 32 hours with a conventional UT system to less than 3 hours with the Laser UT system. Also of note is that the data was of superior quality and the entire surface could be evaluated with the Laser UT system. The conventional system could not follow the ply transition regions and hand-scanning was required to complete the test which is not included in the total scan time comparisons.

Table 2-1 Laser UT is much faster than conventional UT

Inspection Task	LK-UT90 1st Test	LK-UT90 2nd Test	Laser UT 1st Test	Laser UT 2nd Test
Load part into fixture	1.0	1.5	0.1	0.1
Teach part contour	12.0	0.0	0.0	0.0
Adjust scan parameters	0.5	4.0	0.5	0.0
Scan part	18.0	18.0	1.5	1.5
Inspector evaluation	0.5	0.5	0.5	0.5
Total Inspection Time (Hours)	32.0	24.0	2.6	2.1
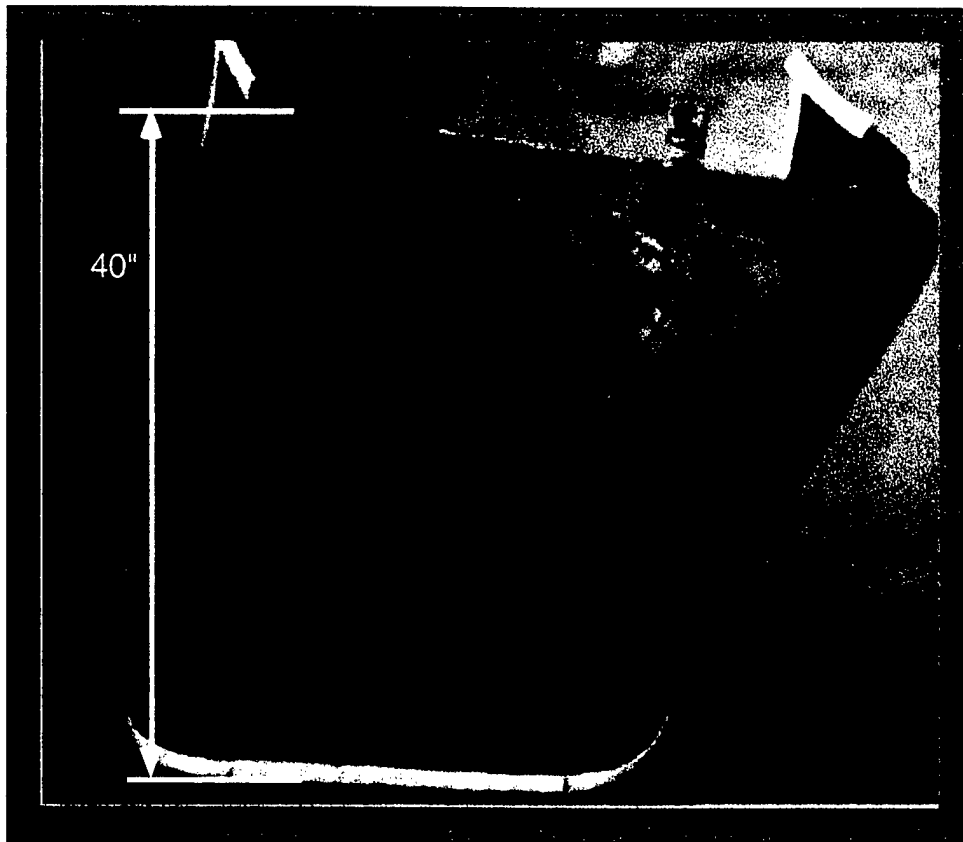
Figure 2-3 Photograph of a large and highly contoured composite test part.

Figures 2-4 and 2-5 show the results obtained from the inlet test. The depth C-scan plot clearly

shows the thickness variations across the part with no indication of the extreme contour that the Laser UT system followed during the test. The B-scan cross-section shows the thickness variations across the part and the strength of the ultrasonic signals validate the outstanding signal-to-noise-ratio (SNR) of the system.
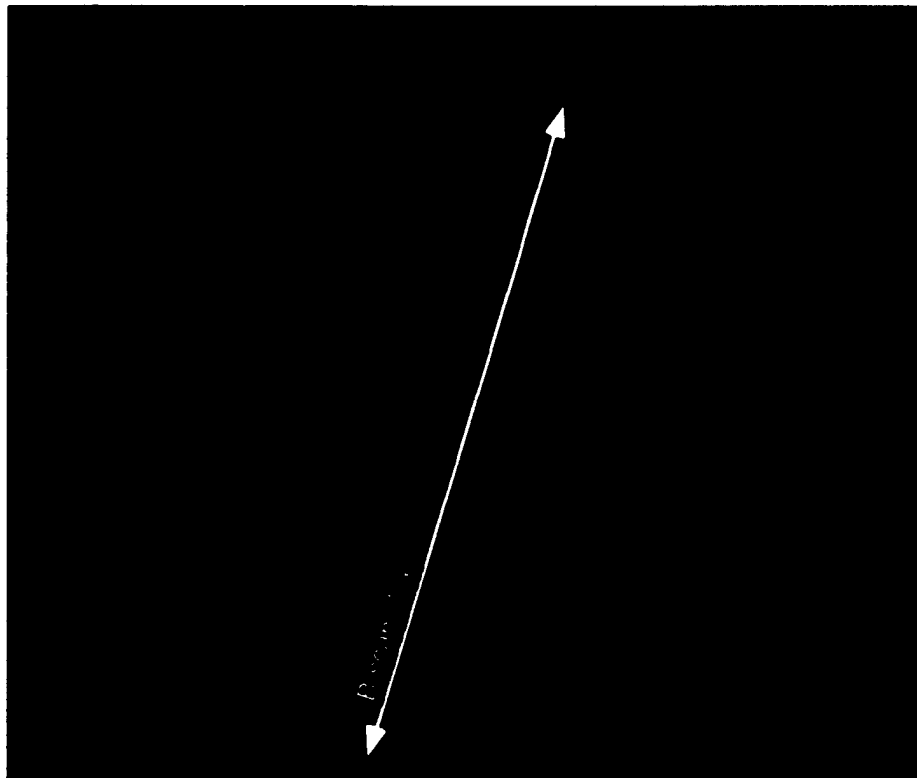
Figure 2-4 The Laser UT system reduced the testing time from 24 hours to 2.1 hours.
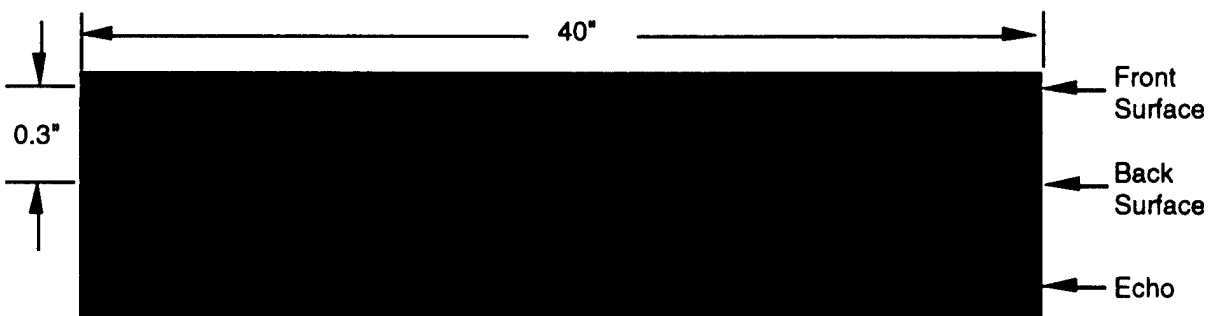
Figure 2-5 This B-scan shows the part thickness along the vertical direction.

Of particular note is that the prototype system could not test this type of material early in the development phase. This was due to the type of protective peel-ply used for this part and the relatively weak signals generated. Instead of requesting the composite designers change back to the old peel-ply system, we worked on improving the system sensitivity to meet the demands of this new material. After several months of effort, the system was improved and this type of materials is now well within the range of acceptable materials.

2.4 TECHNOLOGY TRANSITION

The objectives of technology transition efforts were twofold: first to inform various aircraft programs of the capabilities of Laser UT for rapidly and effectively testing large composite structures, and second to introduce a path for these programs to provide feedback as to what features would most benefit current and future aircraft programs. To this end, F-16, F-22, JSF, and other CR&D programs provided several different types of composite structures and materials to test using the prototype system. In some cases C-scan results from conventional squirter units were provided as a baseline along with part setup and scan times for comparison of technologies.

As an example of these efforts, a cost benefit analysis for testing the inlet section of the F-22 was conducted to determine the impact of a production Laser UT system. This analysis indicated that the F-22 program would save about $9M from the tremendous speed advantages that Laser UT offers. We anticipate that a production Laser UT system will be used to test these structures when the F-22 reaches full production in 2002.

The technologies demonstrated in the LACIS prototype are sufficiently mature that commercialization of Laser UT should become a near-term reality. Figure 2-6 below shows a conceptual view of a large commercial facility for testing detached composite components. This facility would provide the ability to translate the inspection scan head throughout a large inspection envelope. A system constructed for ALC use would be sized to fit the largest composite aircraft that might need in-situ testing. The only drawback to these facilities is the relatively large floor space required because all access to the inspection cell must be limited for laser safety reasons. Although floor space may not be a major concern for many manufacturing and ALC facilities, it is an issue that must be addressed in the design phase.
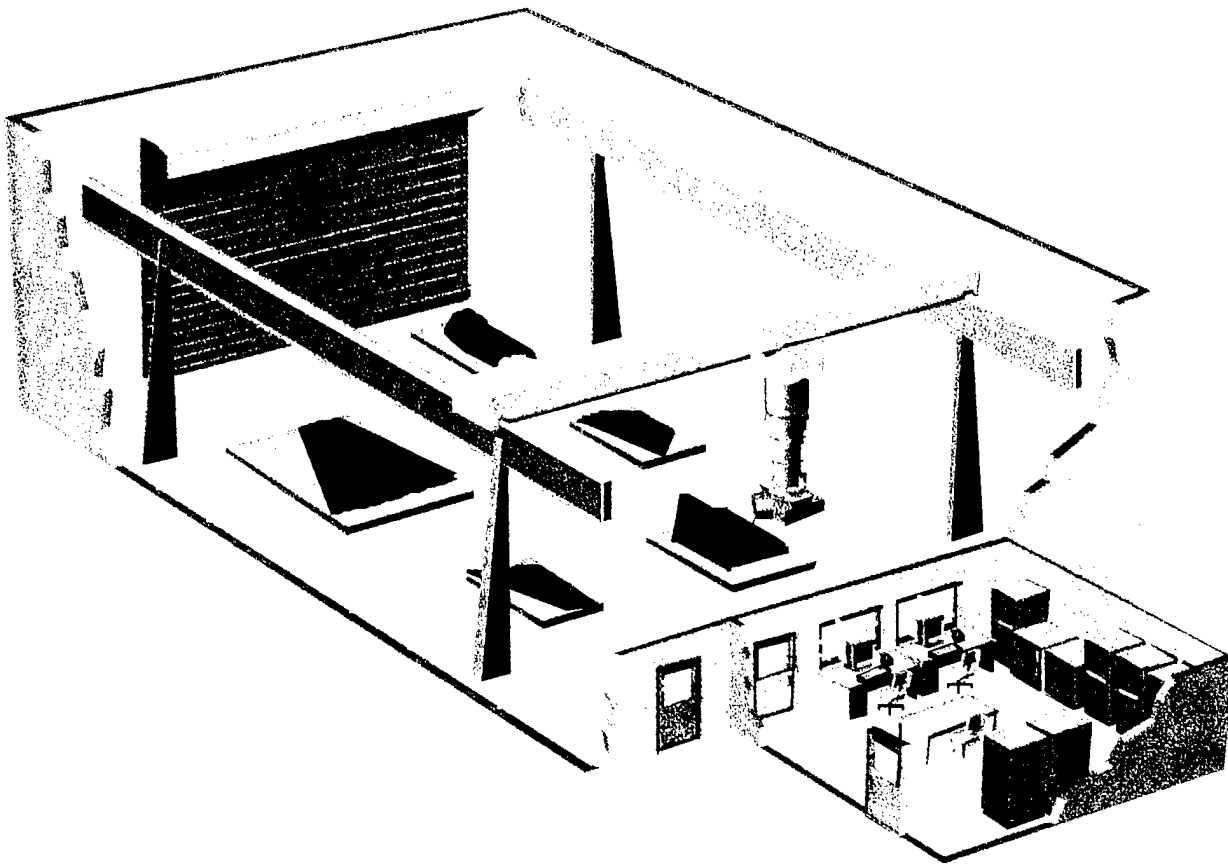
Figure 2-6 A large gantry would be used to move the Laser UT scan head.

Laser UT will transition from the laboratory to both production and in-service use as the demand for composite NDE increases. We anticipate that as current manufacturing NDE capacities are exceeded, Laser UT will be evaluated as a practical and cost-effective alternative to conventional UT systems. Airframe manufacturers will experience this growth in demand several years before the ALC's due to the time delay between initial vehicle deployment and required in-service maintenance schedules. Regardless of when the technology will move from the laboratory into daily use, it will be used initially to solve problems where current systems are inadequate. Laser UT will not be used because it is different but because it can save time and money. This will not be a transition event but instead a transition process.

2.5 COMPLIANCE WITH CONTRACT SOW

The overall objectives of the Contract Statement of Work (SOW) were achieved as described in SOW 4.1 TASK 1 Breadboard Development, and SOW 4.2 Task 2 Prototype Development and Evaluation. The LACIS program successfully progressed from the breadboard stage to the prototype level as outlined in the SOW. All of the technical objectives were met regarding the demonstration of the Laser UT system's inspection speed and sensitivity. The technique of producing multiple inspection points as described in SOW 4.2.1.2 was not implemented into the final prototype configuration due to technical reasons further discussed in sections 3.2.2.3, and 3.2.5.3. The following is a summary of system capabilities as discussed in SOW 4.2.1 and most topics are discussed in considerable detail throughout the report:

- **Image Resolution** was evaluated at spatial step sizes down to 0.025" and the system was capable of resolving thickness to better than 0.005".

- **Defect Sensitivity** was demonstrated on a wide range of materials that included delaminations, inclusions, and porosity. Most inclusion materials were detectable in composites up to 0.5" in thickness.

- **Scanning/Inspection Speed** is dependent on the spatial step size increment and was demonstrated at 100 ft.^{2}/hour for a 0.2" step increment. The inspection setup time was typically very short and almost all system features were computer automated.

- **Data Storage and Retrieval** was demonstrated with a fully digital system using the most advanced computational hardware available. All of the data was captured and stored in real-time and quickly presented to the user in an interactive environment.

- **Types of Materials** tested were representative of F-16, F-22, JSF, and other advanced programs.

- **Thickness Limitations** were determined to be primarily dependent on the type and condition of the surface. For some materials the bulk attenuation characteristics are dominate and thereby further limit the thickness that can be tested. Almost all materials could be tested if the surface had a thin top-layer of organic material for efficient thermoelastic generation of ultrasound. For these types of materials the maximum thickness range is between 0.5" and 1.5".

- **Geometric Limitations** were determined to be of minimal influence for most contoured materials. High-quality data was typically obtained at angles of incidence in excess of 45 degrees. Of note however is the unusual, but possible, situation where the material has an optically transparent layer which can produce very significant angle of incidence effects. This unusual problem is corrected by making the top-layer either opaque or optically rough.

- **Component Access on Aircraft** was not address beyond the conceptual extension of placing the Laser UT scanning head on a gantry positioning system as shown in Figure 2-6. Although shown as a detached component inspection facility the extension into an ALC would simply be to scale the gantry to an appropriate size and configuration for access to the exterior of the aircraft. No analysis was made regarding access to the interior of an assembled aircraft.

3.0 SYSTEM DESIGN

3.1 OVERVIEW OF SYSTEM

The LACIS Laser UT system is a second-generation prototype based upon experience gained while developing a similar system under Lockheed Martin Independent Research and Development (IR&D) programs. This section will discuss some of the design approaches implemented and the technical history that motivated the final design selections.

In general, the design philosophy follows our 1984 IR&D report "Preliminary Conceptual Design of a Laser Ultrasonic Inspection System". This approach identified the use of a pulsed CO_2 laser for the generation of ultrasound and a coaxial laser/interferometer system for ultrasound detection. Also outlined in that report was large area inspection coverage using an optical scanner to rapidly index the coaxial laser beams over the composite surface. A digital data acquisition approach was proposed for improved defect analysis compared with the analog data acquisition systems in use at the time.

The first-generation Laser UT system followed the plan identified in 1984 and demonstrated the potential for the technology when completed in 1987. Despite the success of this system, several known limitations would need to be corrected under the LACIS program. First, the original prototype used a low-power continuous wave (cw) detection laser which required the application of a removable retroreflective surface coating to enhance the signal-to-noise-ratio (SNR) performance. Our group knew in 1983 of the laser ultrasonics work by Krautkramer Bransom (Germany) who used a long-pulsed Nd:YAG detection laser approach to improve the SNR of data obtained from dark materials. This type of pulsed-detection laser was determined too expensive for the original prototype and an inexpensive cw-laser was used to demonstrate fundamental capabilities. The use of a surface coating to enhance system performance is a laboratory method that is generally not appropriate for production use, due to the complexity and uncertainty caused by the additional step of applying and removing the coating materials.

Changing to the long-pulsed laser detection system from the cw-laser detection system greatly

impacted the optical scanner and collection optics design. Inadequate light collection from the almost black composite surfaces required the use of a much larger 300mm gimbal-mounted single-mirror scanner over the small 50mm aperture dual-mirror galvanometer-driven scanner. In addition, the collection optics were changed from small refractive elements to large reflective elements. This increased aperture size created a smaller depth-of-field which required the use of fiber optic between the collection optics and the interferometer to decouple the scanning process and facilitate spatial imaging approaches.

We learned from developing the first-generation prototype that laser amplitude noise could prevent the system from achieving theoretical quantum-noise limited performance. This motivated IR&D work on the development of a differential confocal Fabry-Perot interferometer that could remove common-mode laser noise and provide improved defect detection sensitivity. All of this prior work significantly contributed to the successful implementation of the dual-differential confocal Fabry-Perot (DD-CFP) interferometer under this program. We have shown that SNR performance can exceed what was previously considered limited by fundamental laser noise. Continued enhancements are projected for another 10x SNR increase due to the successful implementation of common-mode noise reduction techniques.

Both the original prototype and the LACIS Laser UT system use custom-assembled digital data acquisition systems. Our design approach has always been to use high-speed digital capture, rapid digital signal processing (dsp), advanced visualization, and provide full archival of the ultrasonic data. This program benefited from considerable improvements in each of these technologies during the past ten years. A "loosely-coupled" architectural approach was selected for separating real-time operations and user interactive tasks. Tight coupling of specialized processors was used for computational intensive tasks within a particular subsystem. Of particular note in the LACIS design are: a dedicated real-time control computer, multi-channel high-speed digitizers tightly coupled to advanced dsp boards, fast intercomputer data communication using reflective memory, multiple vector processors tightly-coupled to the visualization subsystem, and interactive 3D data visualization using an SGI graphics supercomputer. Overall, the outstanding real-time control, data acquisition, and data visualization performance of this system allowed the true capabilities of the LACIS prototype to be demonstrated in a reliable and interactive environment.

3.2 LASERS AND OPTICAL SYSTEMS

3.2.1 Basic Optical Layout

Figure 3-1 is a schematic of the primary laser and optical components which are divided between scanning and detection functions. The scanning unit houses the CO_2 ($\lambda = 10.6\mu m$) generation laser and an optical breadboard that contains the large aperture scanner (LAS) and the large aperture collector (LAC). No vibration isolation is required for the scanning unit. A second optical table holds the detection laser and the interferometer (detection unit). Again, no vibration isolation is necessary. The Nd:YAG ($\lambda = 1.064\mu m$) detection laser is directly coupled to the scanning unit which required mechanically connecting the two optical tables together to assure beam pointing accuracy. A fiber optic cable transmits the light from the LAC to the interferometer. This fiber optic also helps to decouple the focus of the scanning system from the interferometer which makes alignment much less critical.
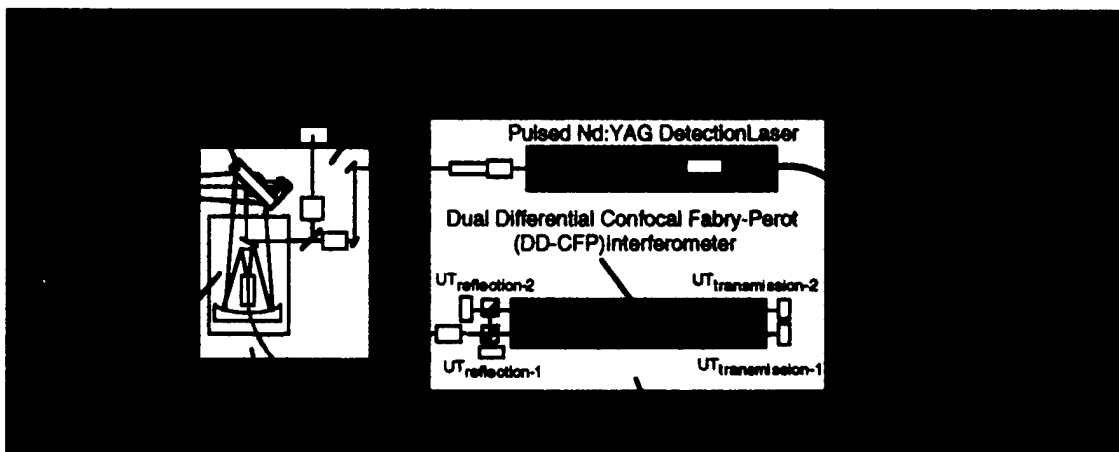
Figure 3-1 Simplified laser and optical layout.

All of the laser and optical components are located in a interlocked optics laboratory (Figure 3-2) adjacent to the computer control room. The interlock system will immediately shutdown the laser systems in the event that a door is opened. This safety system is essential because of the potential severe and irreparable eye damage that could be caused by the high power Nd:YAG laser.
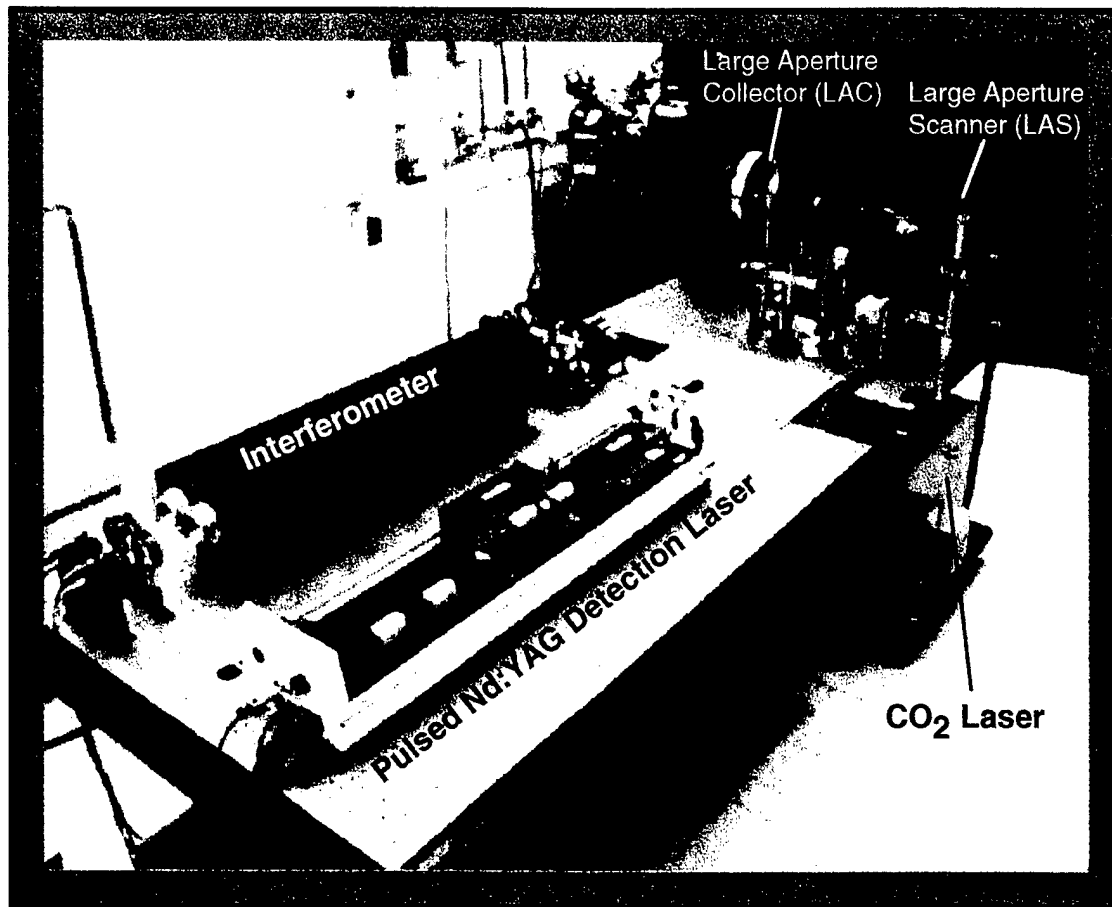
Figure 3-2 Photograph of optical and laser components (some enclosures removed).

3.2.2 Large Aperture Scanner and Large Aperture Collector

Both the large aperture scanner (LAS) and the large aperture collector (LAC) (Figure 3-3) were designed to maximize the amount of light collected from weakly scattering composite surfaces. Practical limits are imposed on the size of these components due to fabrication limits and the fundamental operation of the interferometer. This limit is established by the light gathering invariant caused by spherical aberrations of the interferometer cavity (section 3.2.5.2). The spherical aberrations could be corrected inside the interferometer if a large inspection spot was required at a close working distance, but our final design did not require this feature so no correction was necessary.
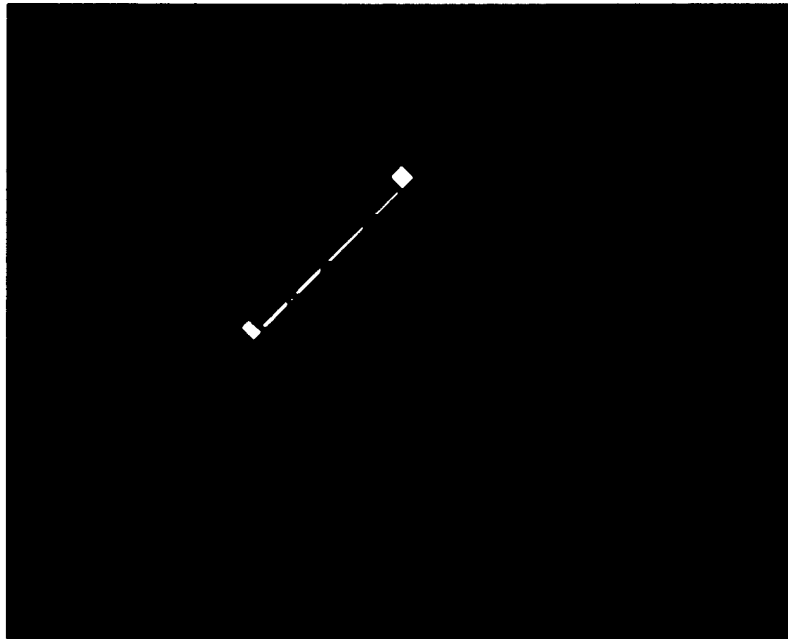
Figure 3-3 Large aperture scanner (LAS) and large aperture collector (LAC).

Photographs of the Large Aperture Collector (LAC), Large Aperture Scanner (LAS), and the LAS controller are shown in Figures 3-4 and 3-5.

The LAC is a 300mm aperture Cassegrain configuration custom designed by LMTAS. Both the 300mm primary and the 50mm secondary mirrors are non-spherical conics manufactured out of aluminum with a computer-controlled diamond-turning process. This custom design has a very large depth-of-field (DOF) that allows complex contoured surfaces to be scanned without real-time focusing in the non-imaging mode. The light collected by the LAC is focused onto an adjustable focal plane that contains the collection fiber optic. This custom fiber optic mount can accept fibers from 400μm to 1500μm in core diameter and can be moved into focus with a computer-controlled translation stage.
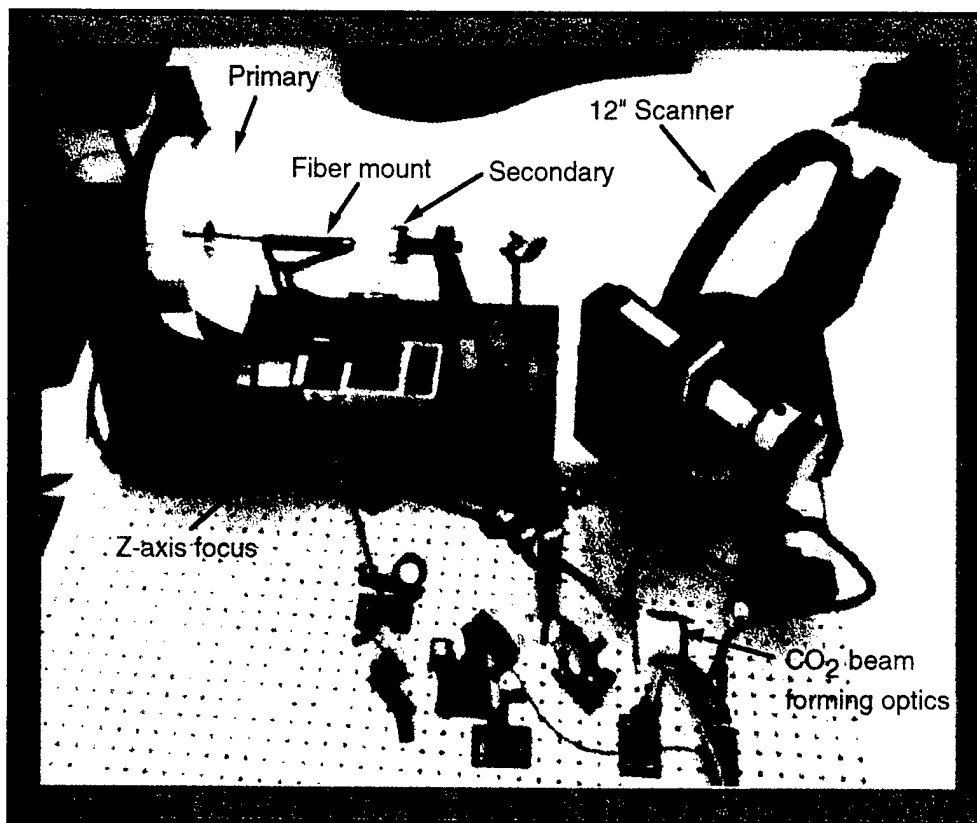
Figure 3-4 Photograph of scanner and collection optics.
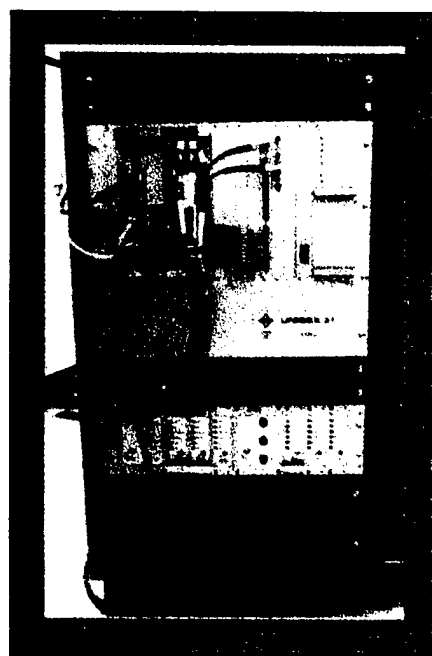
Figure 3-5 Aerotech UNIDEX 31 scanner controller.

21

The LAS is a two-axis gimbal-mounted design with a 12-inch gold-plated mirror for directing the outgoing laser beams and the incoming light scattered off the part. This design provides large light collection capability, coordinate correction software, and the ability to rapidly scan at a slew rate of 60-degrees/sec. This slew rate is more than sufficient to scan at a rate of 100 ft.^{2}/hour. All of the scanner motion control was performed by a dedicated stand-alone scanner controller unit shown in Figure 3-5.

Figure 3-6 is a schematic diagram of the scanning process. A short description is given below:

Scan parameters are entered by the user and downloaded from the SGI Control Computer to the Scanner Controller's 486DX-25 computer. This computer calculates the path for a pair of scan lines and generates a Cam Table that holds the scan points and the encoder values for the Laser Firing Card. These two tables are downloaded to the i960 Scanner Controller Processor and the Laser Firing Card, respectively. The Laser Firing Card issues a trigger out when the scanner encoders reach their specified values. The i960 processor controls the DC motors that move the scanner axes to their specified values and receives encoder information from the scanner axes and transmits that information to the Laser Firing Card. Each trigger point is reached at the specified scan rate of 100Hz for the current laser system. New Cam tables for the next pair of scan lines are computed by the 486 processor while the system is scanning the previous pair of lines, and is ready for downloading at the completion of the line. The LAS executes a smooth direction reversal at the end of each scan line in about 300ms.

Of particular note in this design is that the data trigger is issued when the scanner is exactly at the desired angular position. These triggers are sent to a custom designed I/O distribution controller responsible for maintaining the proper timing delays between the lasers and the data acquisition functions.
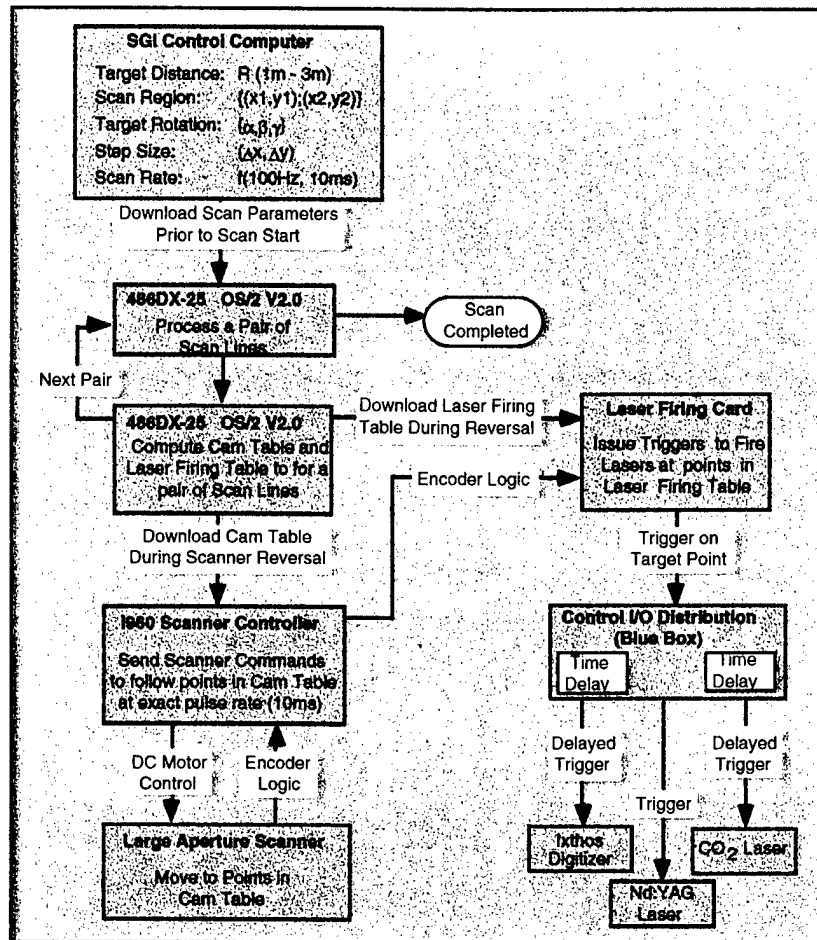
Figure 3-6 Diagram of scanner controller and laser firing card functions.

3.2.2.1 LAS Control Equations

Figure 3-7 shows the three coordinate systems associated with the fixed scanner position, the gimbal mounted mirror, and the target. The process of scanning a surface requires the precise manipulation of the two scanner axes such that the laser beam will accurately intercept the desired target position. Some detailed knowledge of the surface position and shape are necessary to scan a predefined path along the surface. This is not a requirement to assure integrity of the ultrasonic signal, but instead to correlate the data with a specific location on the surface. Our simple approach is to assume that all surfaces are flat-fields and accept the distortion. This distortion can be completely removed if range data is collected at each inspection point to map the data to a 3D surface.

The derivations and analysis below show these relationships for any generalized target surface.

{X,Y,Z}   Fixed to Scanner
{X',Y',Z'}   Local to Mirror
{x,y,z}   Target Surface
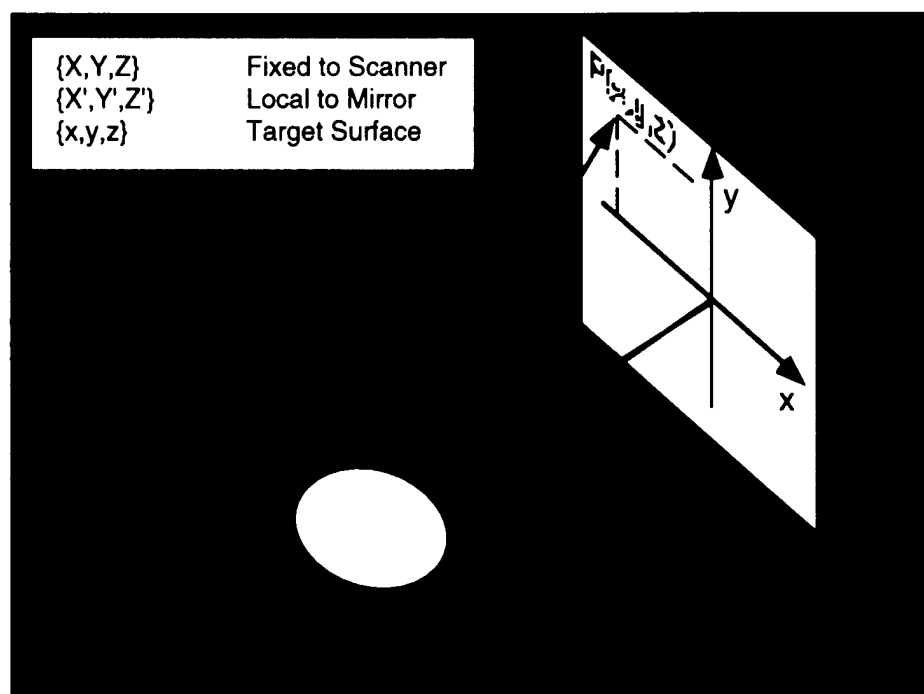
Figure 3-7 Scanner and surface coordinate system.

Definitions

- The cartesian coordinates {X,Y,Z} and {X',Y',Z'} share a common origin; the former is fixed in space and the latter rotates with the scanner mirror.
- The front surface of the mirror is defined as X'-Y' plane and its surface normal is Z'.
- The mirror rotates around the Y-axis (azimuth) and also the X'-axis (elevations).
- Θ is azimuth angle of the mirror measured between **X** and **X'**.
- Φ is the elevation angle of the mirror measured between **Y** and **Y'**.
- The target surface is located in the {x,y,z} coordinate frame.
- D is the distance between the origins of {X,Y,Z} and {x,y,z}.
- ϕ is the angle that **D** is elevated from the X-Z plane and θ is the angle between the projection of D on the X-Z plane and the Z-axis. If these angles are zero then **z** and **Z** are pointing to each other.
- **I** is the incident laser beam that intercepts the center of the mirror from a direction anti-parallel to **X**.
- **R** is the reflected laser beam that intercepts the surface at **P**(x,y,z).

24

Input Parameters

- Surface location: origin of $\{x,y,z\}$, D, θ, and ϕ.
- Desired target point on the surface: $\mathbf{P}(x,y,z)$.

Derivation of: $\Theta\,(x,y,z,D,\theta,\phi)$ and $\Phi\,(x,y,z,D,\theta,\phi)$

The incident laser beam, $\mathbf{I}$, propagates to the center of the scanner mirror anti-parallel to the fixed X-axis. The direction cosines of this incident laser beam are:

$$\cos\alpha_i = -1 \tag{3.2.2-1}$$

$$\cos\beta_i = \cos\gamma_i = 0 \tag{3.2.2-2}$$

The reflected beam, R, follows the law of reflection:

$$\hat{r} - \hat{i} = 2\hat{n}\cos\varepsilon \tag{3.2.2-3}$$

where $\mathbf{r}$ and $\mathbf{i}$ are unit vectors of the reflected and incident beam respectively. The unit vector of the mirror surface along Z' is denoted as $\mathbf{n}$. Last is ε which defines the angle between the incident beam and the mirror surface normal $\mathbf{n}$.

Expanding the vector expression of equation 3.2.2-3 into three components gives:

$$\cos\alpha_r - \cos\alpha_i = 2\cos\alpha_n\cos\varepsilon \tag{3.2.2-4}$$

$$\cos\beta_r - \cos\beta_i = 2\cos\beta_n\cos\varepsilon \tag{3.2.2-5}$$

$$\cos\gamma_r - \cos\gamma_i = 2\cos\gamma_n\cos\varepsilon \tag{3.2.2-6}$$

where we can substitute $\cos\alpha_i = -1$, $\cos\beta_i = \cos\gamma_i = 0$ and $\cos\alpha_n = \cos\varepsilon$. Next consider the equations for the direction cosines of in terms of the azimuthal and elevation angles:

$$\cos\alpha_n = \cos\Phi\cos\Theta \tag{3.2.2-7}$$

$$\cos\beta_n = \sin\Phi \tag{3.2.2-8}$$

$$\cos\gamma_n = \cos\Phi\cos\Theta. \tag{3.2.2-9}$$

25

The direction cosines for the reflected beam as function of mirror azimuthal rotation Θ, and elevation angle Φ are defined as

$$\cos\alpha_r = 2\cos^2\Phi\sin^2\Theta - 1 \qquad (3.2.2\text{-}10)$$

$$\cos\beta_r = 2\cos\Phi\sin\Phi\sin\Theta \qquad (3.2.2\text{-}11)$$

$$\cos\gamma_r = 2\cos^2\Phi\cos\Theta\sin\Theta \qquad (3.2.2\text{-}12)$$

The direction cosines of **R** can also be written in Cartesian coordinates as:

$$\cos\alpha_r = \frac{X}{\sqrt{X^2 + Y^2 + Z^2}} \qquad (3.2.2\text{-}13)$$

$$\cos\beta_r = \frac{Y}{\sqrt{X^2 + Y^2 + Z^2}} \qquad (3.2.2\text{-}14)$$

$$\cos\gamma_r = \frac{Z}{\sqrt{X^2 + Y^2 + Z^2}} \ . \qquad (3.2.2\text{-}15)$$

A target point **P**(x,y,z) can be transformed into {X,Y,Z} coordinates as **P**(X,Y,Z) with the following expressions:

$$X = D \cdot \cos\phi\sin\theta - x \qquad (3.2.2\text{-}16)$$

$$Y = D \cdot \sin\phi + y \qquad (3.2.2\text{-}17)$$

$$Z = D \cdot \cos\phi\cos\theta - z. \qquad (3.2.2\text{-}18)$$

Next substituting the above expressions into the direction cosines,

$$\cos\alpha_r = (D \cdot \cos\phi\sin\theta - x)/R \qquad (3.2.2\text{-}19)$$

$$\cos\beta_r = (y + D \cdot \sin\phi)/R \qquad (3.2.2\text{-}20)$$

$$\cos\gamma_r = (D \cdot \cos\phi\cos\theta - z)/R \qquad (3.2.2\text{-}21)$$

where,

26

$$R = \sqrt{(x - D \cdot \cos\phi\sin\theta)^2 + (y + D \cdot \sin\phi)^2 + (z - D \cdot \cos\phi\cos\theta)^2} \quad (3.2.2-22)$$

We can define the mirror azimuthal rotation Θ and elevation angle Φ as functions of target coordinates {x,y,z} and surface location parameters D, θ, and ϕ:

$$\Phi = \sin^{-1}\left[\frac{\frac{y}{R} + \frac{D}{R} \cdot \sin\phi}{\sqrt{2\left(1 - \frac{x}{R} + \frac{D}{R} \cdot \cos\phi\sin\theta\right)}}\right] \quad (3.2.2-23)$$

$$\Theta = \sin^{-1}\left[\frac{1 - \frac{x}{R} + \frac{D}{R} \cdot \cos\phi\sin\theta}{\sqrt{2 - 2\frac{x}{R} + 2\frac{D}{R} \cdot \cos\phi\sin\theta - \left(\frac{y}{R} + \frac{D}{R} \cdot \sin\phi\right)^2}}\right] \quad (3.2.2-24)$$

Flat Field Scanning

Equations 3.2.2-23 and 3.2.2-24 are general formula used to control the scanner rotations such that the projected beam will intercept any desired target point P(x,y,z) in the local coordinate system of the target surface. In the special case of a flat-field target surface we can set z=0. This allows some generalizations about the orientations of the flat surface to describe tilted and rotated local coordinates. First we define the target surface plane as x'-y' with a surface normal along z'. The α, β, γ angles are redefined here to describe the rotation of the target plane about the y-axis, z-axis, and x-axis respectively. The parameters x,y,z in equations 3.2.2-22, 3.2.2-23, and 3.2.2-24 should now be changed to:

$$x = (x'\cos\beta - y'\sin\beta)\cos\alpha \quad (3.2.2-25)$$

$$y = (x'\sin\beta - y'\cos\beta)\cos\gamma \quad (3.2.2-26)$$

$$z = -(x'\cos\beta - y'\sin\beta)\sin\alpha - (x'\sin\beta + y'\cos\beta)\sin\gamma \quad (3.2.2-27)$$

Figure 3-8 shows the scanner azimuthal and elevation angles that correspond to the desired grid of uniform target points for a flat surface 100-inches from the origin of the scanner. This plot clearly illustrates the need for precise control of the scanner motion to produce a uniform coverage of a part. Simple equal angular steps would produce substantial distortions in the inspection results.
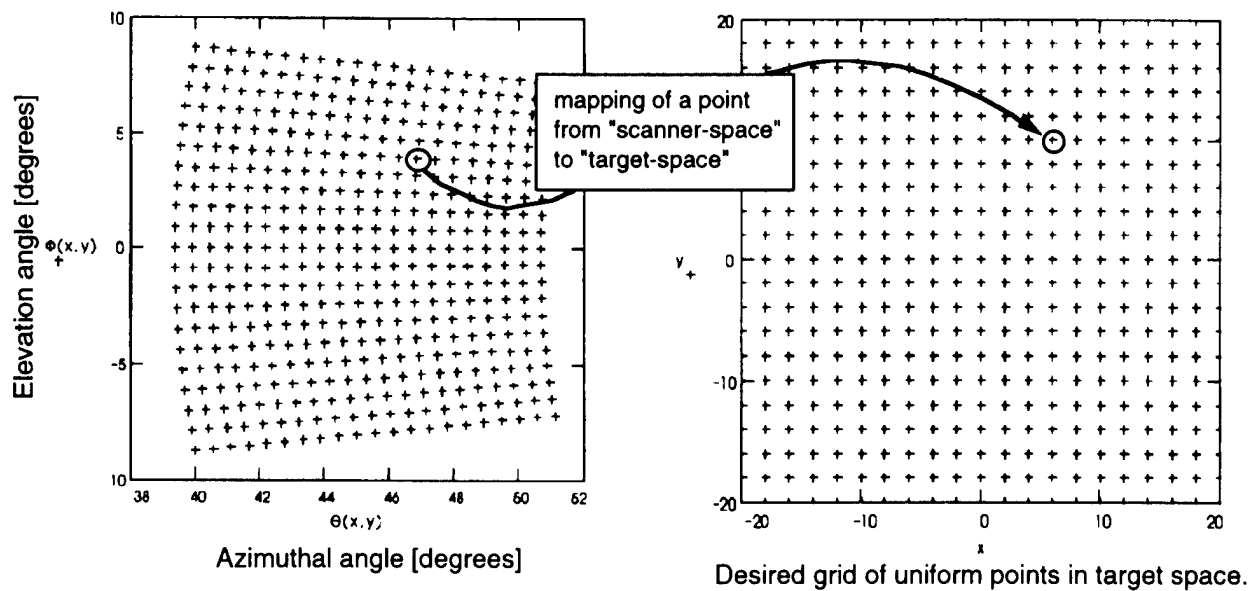
Figure 3-8 Plot of required scanner angles for a uniform grid at D=100".

3.2.2.2 Large Aperture Collector (LAC) Design and Analysis

Good performance of the LAC was critical for the success of the LACIS design. Changing from the low-power detection laser to the high-power long-pulsed detection laser would not provide enough light for the required SNR without also increasing the aperture of the system. It was determined that a 300mm aperture would be the maximum practical size. This matches the largest reasonable scanning system that could be used and the limits of the interferometer. A refractive lens design of this size would be too costly to fabricate, thus a reflective design was sought.

Before the particular design of the LAC is discussed, we fiirst review some basic requirements. The LAC must image the inspection spot at the composite surface on to the end of a collection fiber optic (Figure 3-9). This is not a zoom design, therefore the size of the image spot will vary with the distance to the target. A quick analysis will define the maximum aperture size that can be used to collect the light from the target for a given distance, fiber optic size and numerical aper-

ture (NA). The fiber NA is defined as NA $=\sin\theta$ where θ is the maximum acceptance angle of the fiber. We can also assume that the core diameter of the collection fiber will be 1mm with a NA $= 0.4$. Later sections will discuss why this is a good match for the interferometer.
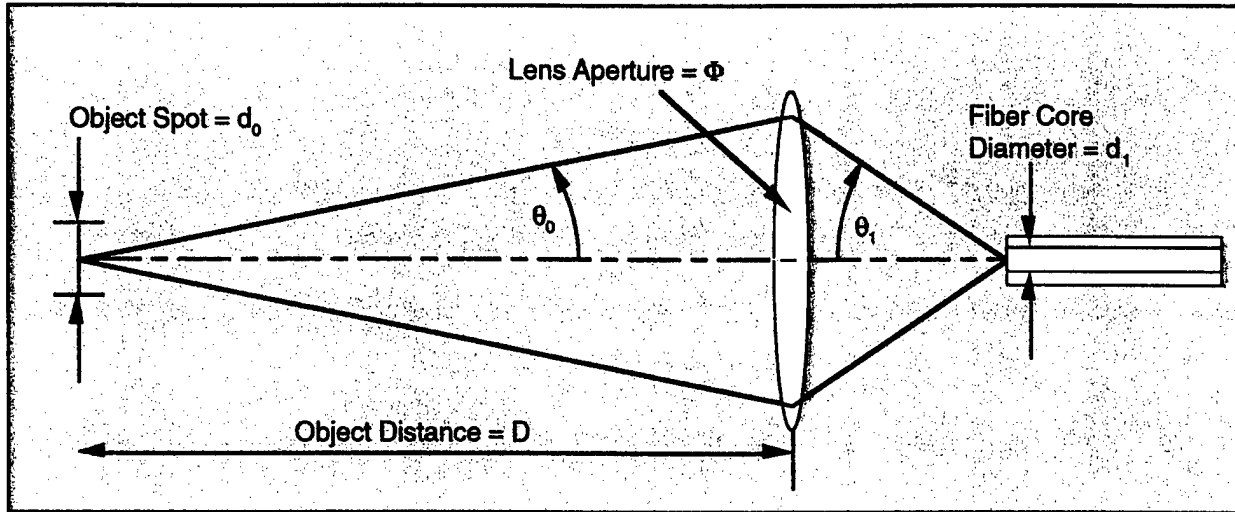
Figure 3-9 The optical invariance will help scale the LAC components.

Often the fastest and simplest method for deciding what is possible for a given set of constraints is to apply the optical invariance principle. In our case we will assume that a large NA fiber will be used to improve the compactness of the LAC, and that the object spot size is 5mm at a distance of 2m from the lens. This will provide an estimate of the largest usable aperture size. The invariance equation is given as:

$$\frac{d_0}{2} \cdot \theta_0 = \frac{d_1}{2} \cdot \theta_1 .$$

(3.2.2-1)

where the variables are defined above in Figure 3-9.

For small angles we can use the approximation $\theta_0 \approx \dfrac{\Phi}{2D}$ and $\theta_1 \approx NA$ which gives

$$\Phi_{max} \approx 2D \cdot NA \cdot \frac{d_1}{d_0} = 2 \cdot 2000mm \cdot 0.4 \cdot \frac{1mm}{5mm} = 320mm \qquad (3.2.2\text{-}2)$$

Thus we see that the 300mm aperture is slightly less than the largest size that can couple light from a 5mm spot at 2-meters (closest design condition) into the collection fiber.

Two performance issues were critical for the design of the LAC: 1) efficient power collection, and 2) imaging quality for the spatial imaging technique. It was immediately apparent that a two-mirror Cassegrain design would be the best general configuration. This is classically used at infinite conjugation ratios for imaging a planet or star with a very small field of view. It is usually constructed with a relatively large primary mirror and smaller secondary mirror in an on-axis arrangement with the secondary mirror obscuring a small portion of the primary mirror. Off-axis designs were not pursued due to the minimal obstruction caused by the secondary mirror. Our application was far from classical due to the finite conjugation ratios defined by the relatively close distance to the composite surface. This demanded a unique design solution.

We also had to select a method for changing the focus of the LAC to work at different distances from the composite surface. The two alternatives were to: 1) adjust the position of the secondary mirror to maintain the image on a fixed focal plane, or 2) move the focal plane into focus as the object distance varied. Fixed primary and secondary mirrors were selected to assure that imaging quality would not be compromised due to the complexity of moving the imaging elements relative to each other. Instead, the collection fiber optic was mounted on a motorized translation stage to provide automated focusing. The fiber was mounted to minimize any obstruction caused by the mounting bracket near the secondary mirror where the optical ray density is relatively high. The optical bracket was positioned as close as possible to the primary mirror where the ray density is low. This arrangement is shown in Figure 3-10 and a photograph of an optical fiber used to couple the light from the LAC to the interferometer is shown in Figure 3-11.
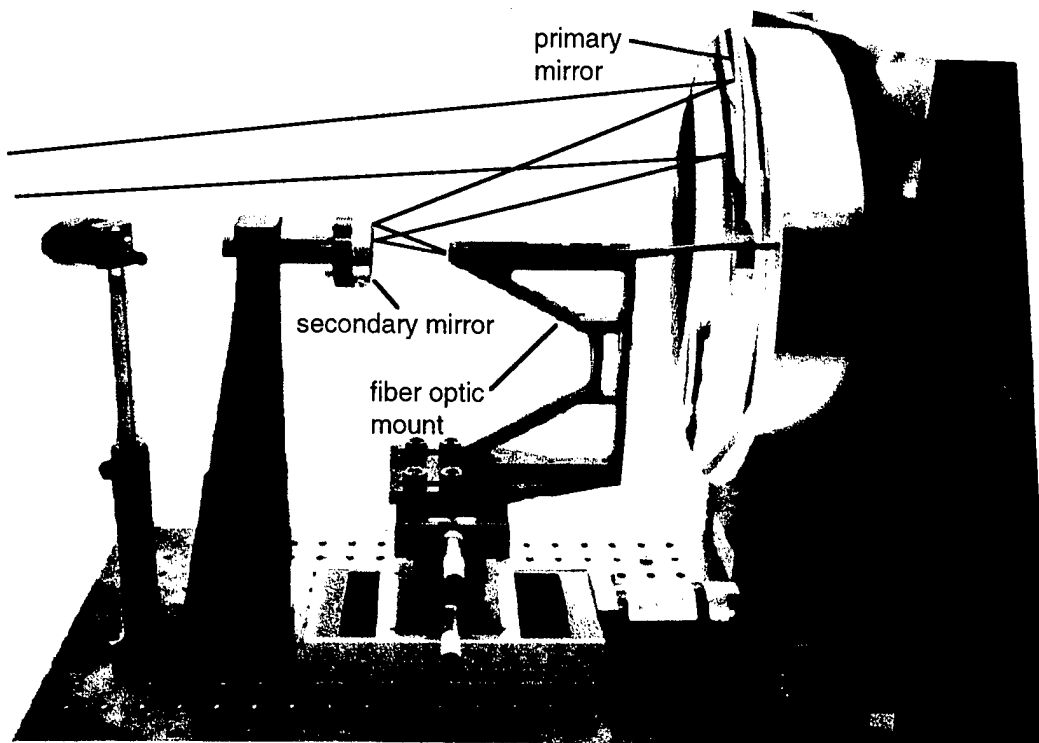
Figure 3-10 LAC shown with ray-trace into collection fiber.
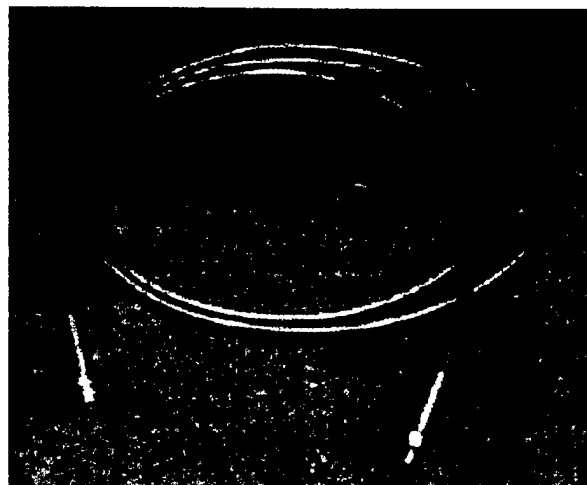
Figure 3-11 The LAC coupled light to the interferometer via an optical fiber.

The specific LAC design was obtained by optimizing a merit function in a lens design program (Zemax-EE). The merit function was constrained to have the rays at the image plane not exceed the numerical aperture of the collection fiber (about NA=0.4). The primary and secondary mirrors were given variable radii of curvature and conic constants and the rms spot size was minimized for object heights of 0, 2mm, 5mm, and 10mm. These parameters were optimized for 18 discrete object distances ranging from 1800mm to 3500mm from the LAC. This approach produced a design with balanced performance over a wide operating range. Specific design data is given in the Appendix. Figures 3-12 and 3-13 show ray trace data for an object distance of 1800mm and 3500mm respectively. Note the position of the image plane as the object distance changes and how the entrance angle into the fiber is held at almost the same value to match the numerical aperture (NA) of the collection fiber independent of the focal position.
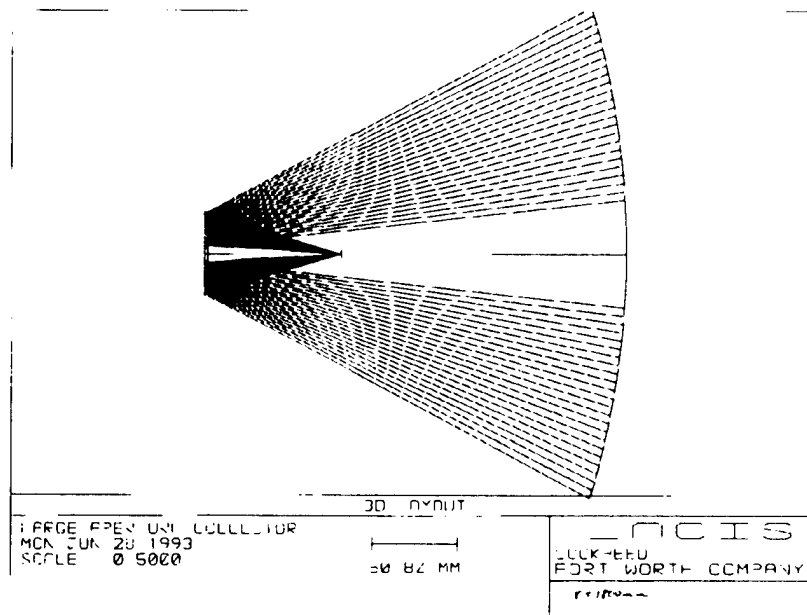
Figure 3-12 LAC ray trace for an object distance of 1800mm.
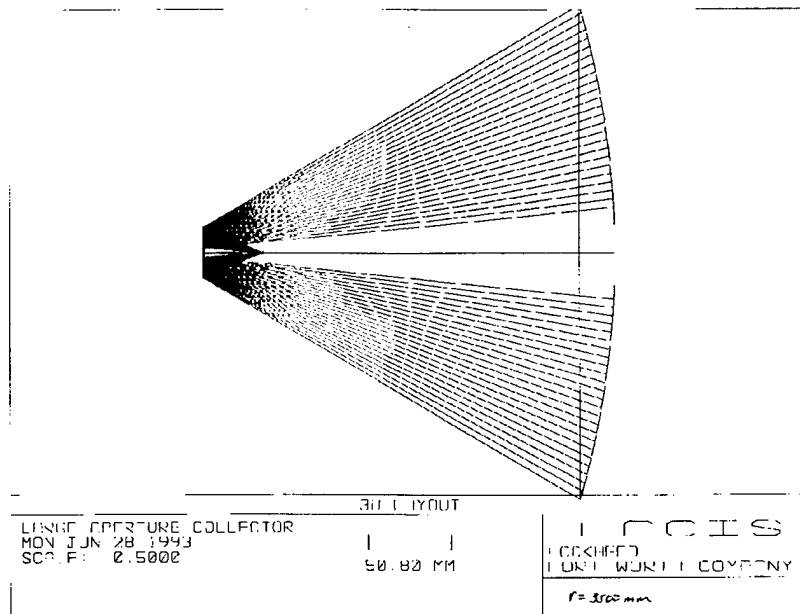
Figure 3-13 LAC ray trace for an object distance of 3500mm.

Figure 3-14 shows the predicted imaging performance of the LAC over a large range of target distances assuming some amount of decentering of the two mirrors caused by misalignment. As indicated, the LAC can resolve a 20mm object to better than 100microns over most of the working range. Also of note is the relative balance in performance over the entire operating range. This balanced performance was a significant feature of the optimization merit function; designing for a single object distance will improve (reduce) the rms spot size but gives very poor performance at other working distances.

Two separate criteria were used to predict the sensitivity of the LAC to defocusing effects caused by optically scanning an arbitrary shaped 3D surface. One was for non-imaging performance and the other was for imaging applications. The non-imaging criteria was defined as the depth-of-field (DOF) of the LAC for collecting 50% of the light from a 5mm spot into the collection fiber. This is strictly a power collection problem and the DOF is plotted as a function of object distance in Figure 3-15. The DOF relative to the focus position ranged from about +25/-50 mm at the close point to about +275/-250 mm at the far point of the design. This defines how often and accurate

33

the LAC would need to be focused on the composite surface and maintain at least a 50% collection efficiency.

Figure 3-14 Balanced optical performance is predicted by rms spot size analysis.
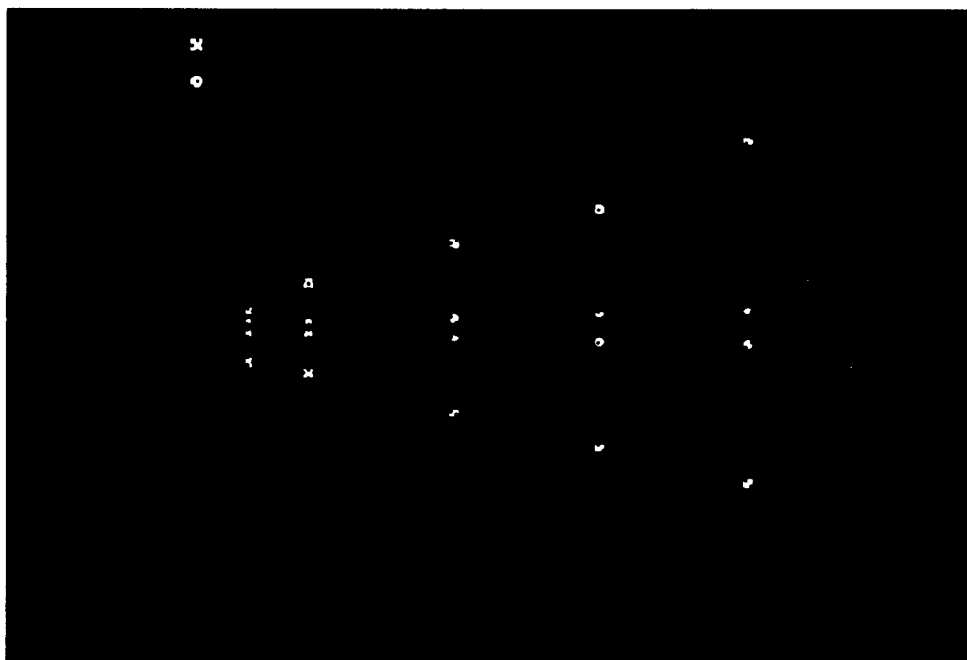
Figure 3-15 Spatial imaging approach reduces the depth of field.

The imaging application is much more sensitive to defocusing effects as indicated by the very small DOF (typically < 10mm) shown in Figure 3-15. This shows that the spatial imaging technique will require significantly more active focusing of the LAC as a complex surface is scanned.

Performance evaluations were conducted to determine if the actual LAC functioned as desired. A useful visual indication of performance can be made by projecting laser light backwards through the system. This is done by injecting visible laser light into the collection fiber and observing the image produced by the LAC on a distant target plane. The projected spot indicates how large the collection spot size is for a particular fiber core diameter and the sharpness of the image is an indicator of any distortion caused by the LAC design.

Figure 3-16 shows four photographs of the back projected spots for various fiber core sizes when the image plane is in-focus. Note that each of the images is very sharp.
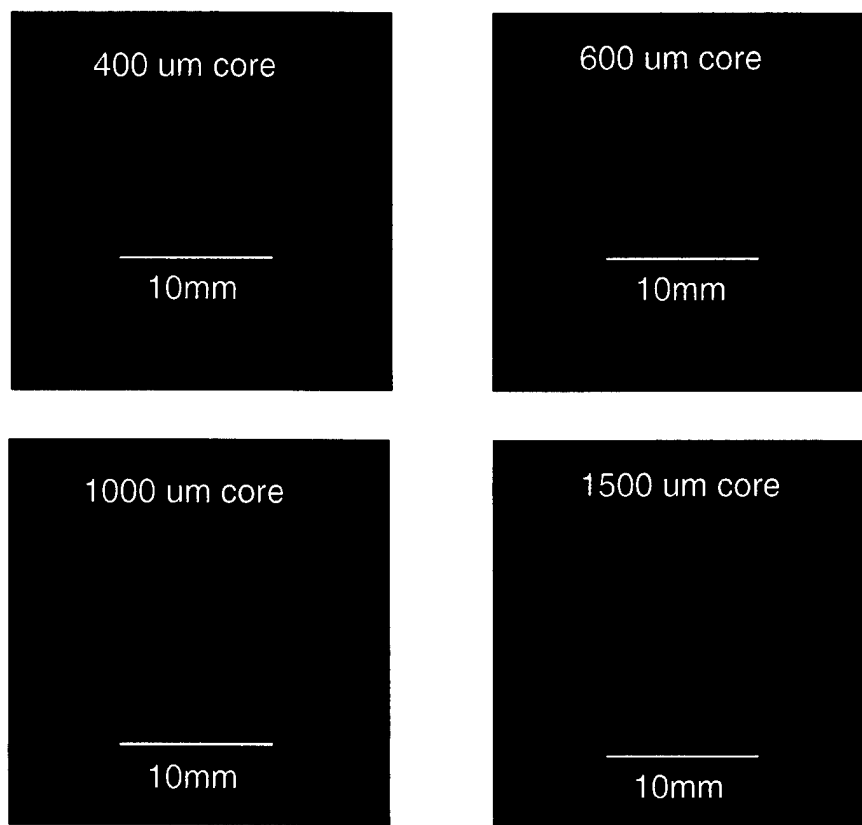
Figure 3-16 Photographs of back projected images for various fibers.

Figure 3-17 shows the effect of defocus on the image. Note the blurred edges when the image plane is moved 50mm out of focus but the spot size is approximately constant. This is an example of why a large DOF is observed for non-imaging applications.
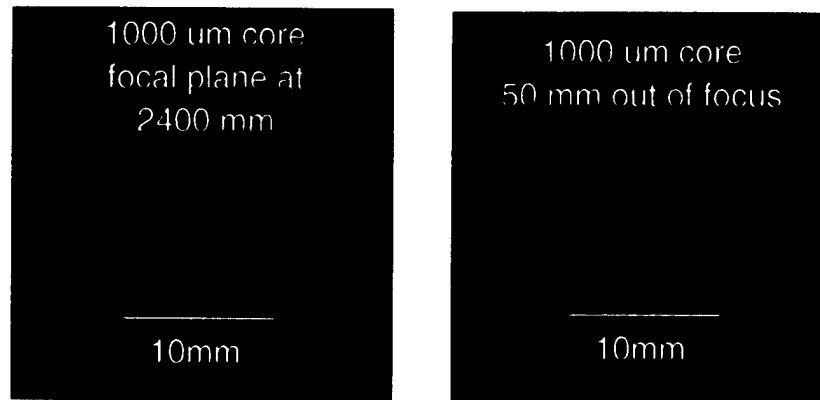
Figure 3-17 Photographs of back projection images showing focus effects.

3.2.2.3 LAC Spatial Imaging Analysis

The concept of imaging an extended area from the composite surface into the interferometer required some special considerations for the LAC. As discussed in the previous section, there is a fundamental difference between designing for power collection and preserving an image with some minimal amount of distortion. The analysis presented in Figure 3-14 showed the rms spot-size for various focal distances and object heights. To get a better idea of how this actually would affect the ultrasonic image produced, we also analyzed what the distortion would look like at different focal positions and with some amount of defocus. Figure 3-18 is a plot of the apparent image that the system could resolve at distances of 2000, 2500, and 3000 mm from the LAC. Also shown is the effect of moving the surface out of focus some small distance. This analysis combines the data presented in the previous section into a single result and illustrates the importance in maintaining the composite surface in focus during a scan. If the surface is not in focus, then the spatial imaging technique will produce ambiguous data caused by the cross-talk of the light to the different collection fibers.
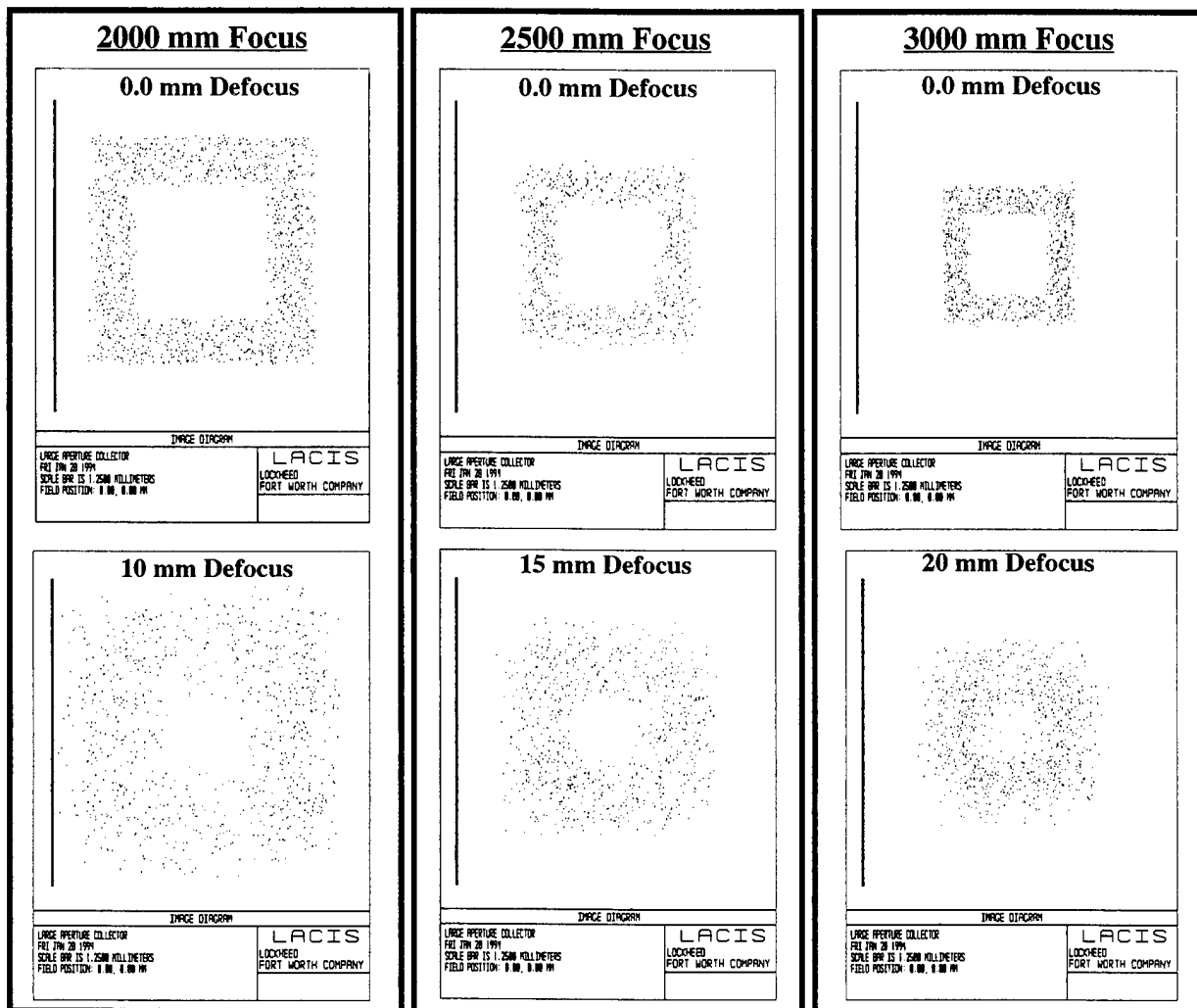
Figure 3-18 Analysis of LAC shows how image quality changes with target position.

As noted in section **2.0 PROGRAM OVERVIEW**, the spatial imaging technique was not integrated into the final LACIS prototype configuration. One of the main reasons for not implementing the technique was the much more restrictive focusing requirement compared to the nonimaging technique. In principle, it is possible to maintain the LAC focus to within 10mm in realtime using an optical ranging system with sufficient resolution. However, this increased sensitivity to the DOF was not consistent with the desire for the final design to be highly insensitive to the part geometry. The driving parameter for this problem is the large aperture of the system. The

300mm aperture caused the reduction in imaging DOF. If for example, a small 50mm aperture system was capable of collecting sufficient light, then the DOF would improve dramatically. Although the 300mm optics were capable of maintaing sufficient image quality, the desire for fast optical scanning of a complex shape without real-time focusing made the final design a non-imaging configuration.

The actual imaging performance was observed using the back projection technique described earlier. Figure 3-19 shows the four spots produced at the image plane when a visible laser beam was injected into the coherent four-fiber bundle. The imaging quality is very good for such a large aperture system. Unfortunately, as predicted, the system is not tolerant to defocusing effects as is indicated by the blurred photograph on the right (note this is only a 2% change in the image plane position). Thus the LAC performed as predicted, but the sensitivity to defocus made spatial imaging too restrictive for our current approach.
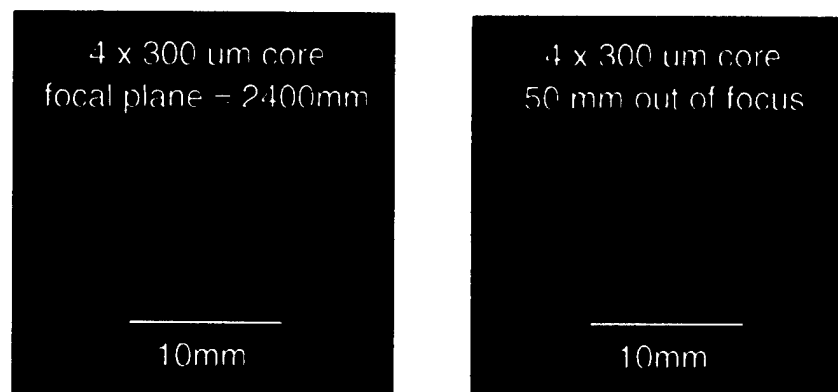
Figure 3-19 Photographs of back projected images show focus sensitivity

3.2.3 Carbon Dioxide Generation Laser

The pulsed carbon dioxide (CO_2) laser used for ultrasonic generation is a commercially available Lumonics IMPACT series 2000 laser shown in Figure 3-20. It is capable of pulsing at a rate up to 150Hz and has an average power of 50 Watts with a maximum pulse energy of 500mJ at 100Hz.

The gain-switch spike pulse duration is approximately 100ns in duration.

This laser uses a premixed gas mixture consisting of 4% CO, 8% CO_2, 16%N_2, and 28% He that can be stored either internal to the laser (for portability and system compactness) or external (to allow for a larger gas supply). The only modification to the standard laser configuration was the change from a 4-meter radius rear mirror to a 14-meter radius mirror (discussed in detail later). Beam divergence was reduced from 4 mrad down to 2 mrad, as shown below in Table 3-1. The depth-of-field of the spot at the composite surface is improved by this reduction in divergence. The mode structure of the beam was also reduced but no measurable changes in the induced ultra-sound were observed.
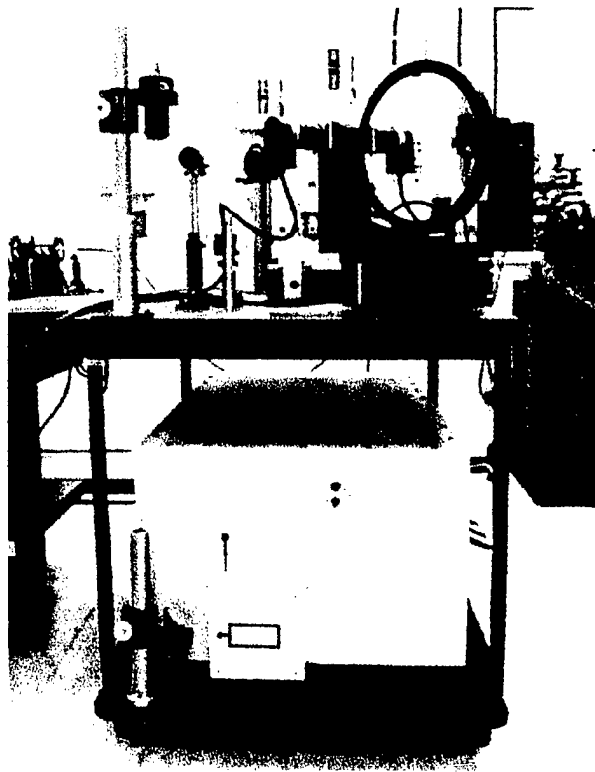
Figure 3-20 The CO_2 laser is directly coupled to the LAS.

Table 3-1 CO2 Generation Laser Beam Characteristics

Rear Optic Radius [m]	Divergence [mrad]	MODES
4m	4	6
14m	2	3

The beam forming optics consisted of a pair of Germanium lens arranged basically in a Keplerian beam expander configuration with the virtual image of a negative lens imaged by a larger positive lens. This expanded the beam from approximately from 15mm to 25mm and the separation of the two lenses was adjusted to produce the desired spot size at the composite surface (usually about 5mm). No active control of the beam spot size was necessary with the lower beam divergence of the modified laser cavity.
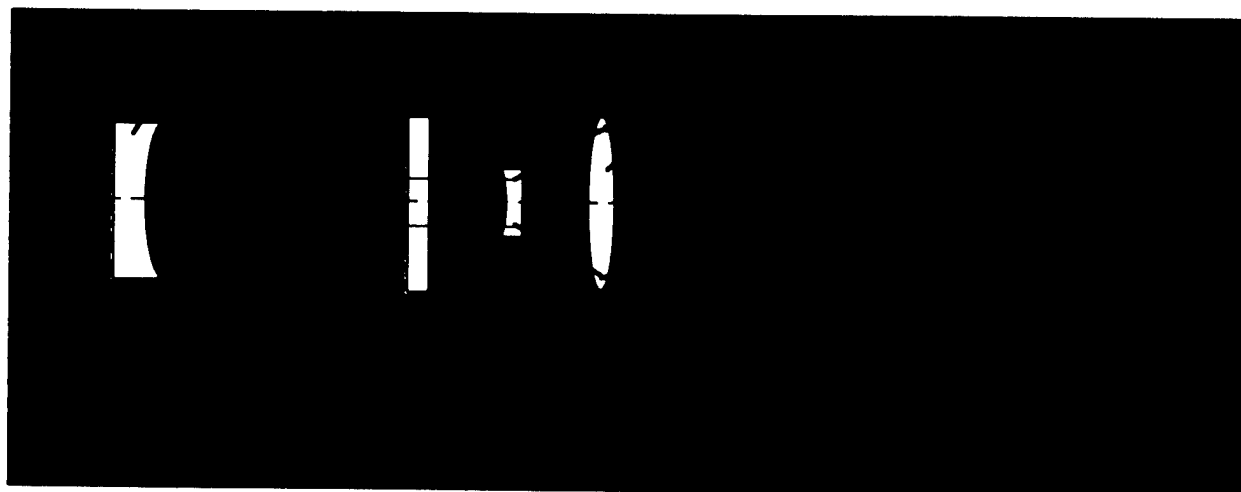
Figure 3-21 CO_2 laser cavity and beam forming optics.

Figure 3-21 shows the basic relationships between the laser cavity design and the beam forming optics. Our design uses a spherical total-reflector rear optic and a plano output coupler. Laser cavity analysis shows that the beam wavefront must match the curvatures of these two elements; thus

the beam waist must occur at the output coupler where the wavefront radius goes to infinity. The divergence (half-angle) for a TEM_{00} gaussian laser beam is given by:

$$\theta_{gaussian} = \frac{\sqrt{\lambda/4}}{\sqrt[4]{LR - L^2}},$$

(3.2.3-1)

where L is the cavity length and R is the rear mirror radius. A TEM_{00} condition is maintained only if the aperture of the beam waist is restricted to radius given by

$$\omega_0 = \sqrt{\frac{\lambda}{4}} \sqrt[4]{RL - L^2}.$$

(3.2.3-2)

For output apertures larger than ω_0, the beam structure will not be gaussian but some higher-order mode. This will also result in a larger beam divergence given by

$$\theta_N = \frac{a}{\sqrt{RL - L^2}}.$$

(3.2.3-3)

The product of the laser aperture radius and the divergence produces an optical invariant that will be maintained throughout the system. Referring back to Figure 3-21 we can equate this invariant to the aperture of the beam forming optic Φ, the focal position D, and spot size 2d.

$$\text{Optical Invariant} = \theta_N \cdot a = \frac{\Phi}{2D} \cdot d$$

(3.2.3-4)

This type of analysis is not rigorous because a gaussian beam waist does not exactly match the focal position of an image, but for this case the errors are very small and more detailed analysis will not improve system performance. We can now calculate the approximate spot size for the system by using

$$d = 2 \cdot \frac{a^2}{\sqrt{RL - L^2}} \cdot \frac{D}{\Phi}.$$

(3.2.3-5)

Our design used a = 7.5mm, R = 14m, L = 1.04m, Φ = 25mm, and D varied between 2000mm and 4000mm. For example at D = 4000mm, the spot size 2d = 5mm, which is our nominal design value for the target spot size. The energy delivered to the composite surface is typically 200mJ or less to remain below ablation thresholds for the 5mm to 10mm spot sizes. This will produce a power density between 1 MW/cm^2 and 10 MW/cm^2 for a 100ns pulse.

3.2.4 Nd:YAG Detection Laser

Optical detection of ultrasound is best summarized as an exercise in managing noise. It can be assumed that a properly designed Laser UT system will maximize signal by choosing the proper generation laser and the most sensitive interferometer design. The problem now is one of minimizing noise while maximizing signal. This will always come down to increasing the amount of light reaching the photodetectors until another noise term is dominate. This will be discussed in more detail in Section 3.2.4.1.

The objective of the detection laser is to provide an intense illumination of the inspection point while the ultrasonic wave is propagating through the material. Surface modulations will perturb the properties of the scattered light and the ultrasonic data can be demodulated with a properly constructed interferometer. This laser must be of single spatial and axial frequency for the interferometer to work.

The detection laser used for the Laser UT prototype is a master oscillator power amplifier (MOPA) configuration (Figure 3-22 and Figure 3-23).
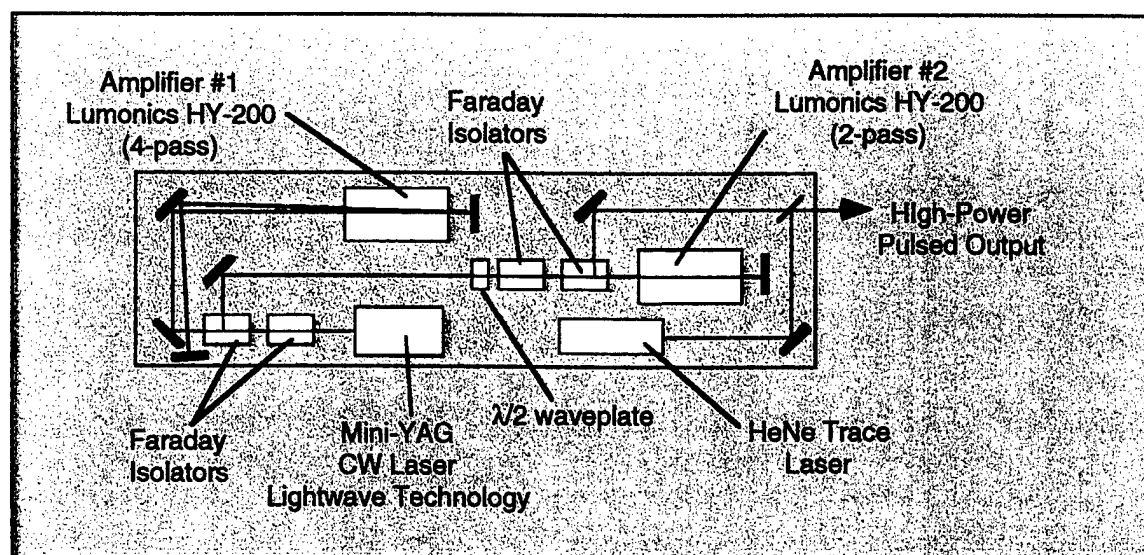
Figure 3-22 Schematic of the pulsed Nd:YAG detection laser.

The master oscillator is a single longitudinal mode (SLM) solid state diode-pumped Nd:YAG laser with a continuous wave (cw) output. The particular master oscillator laser used is manufactured by Lightwave Technologies (three different models were used at various times ranging from 4mW to 500mW). Two flash-lamp pumped Nd:YAG amplifiers are arranged in a six-pass configuration to produce a 100 microsecond pulse with approximately 1000W of peak power. The amplifier system is a HY-200 custom configuration by Lumonics (formerly JK lasers). Maximum pulse repetition is limited to 100Hz. Care must be taken in a MOPA design to reduce feedback from the power amplifiers back into the master oscillators. Faraday isolators are essential to manage this feedback problem.
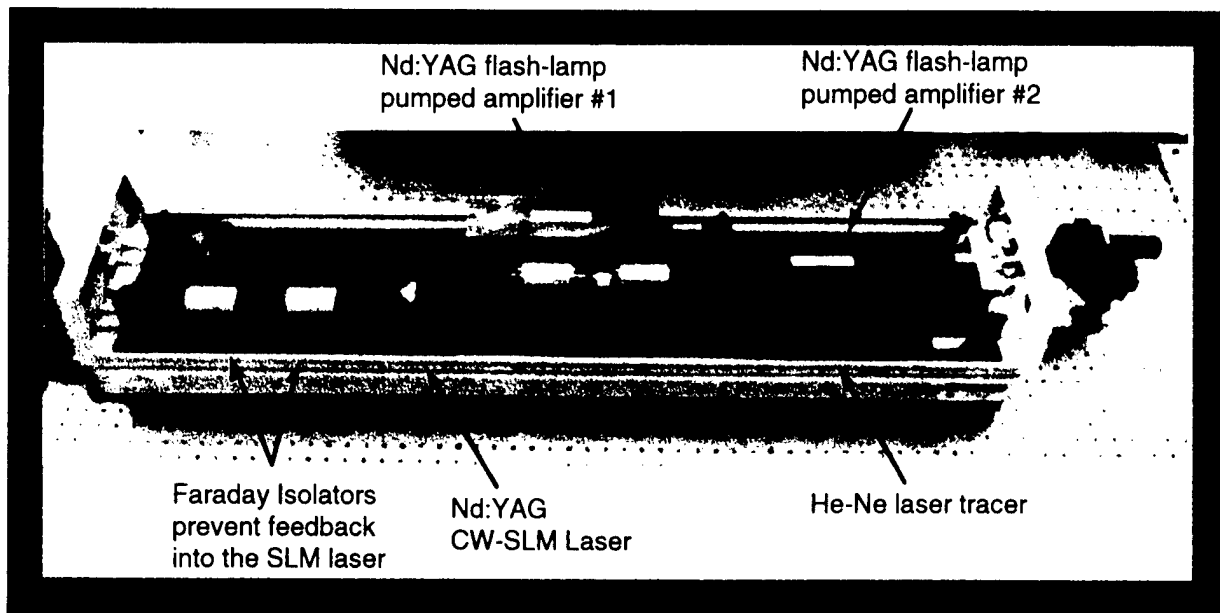
Figure 3-23 Photograph of detection laser with cover removed.

The single-pass gain (output relative to the input) is a non-linear relationship given by:

$$G = \frac{I_{out}}{I_{in}} = G_o \cdot \exp\left[-\frac{I_{out} - I_{in}}{I_{sat}}\right] \qquad (3.2.4\text{-}1)$$

where G_o is the small signal linear gain through the amplifier, and I_{sat} is the saturation intensity of the laser medium. Note that for a small input intensity the gain will be linear, but at higher lev-

els (e.g. multiple passes) the amplifier will saturate and limit the extracted power. For this reason the output power from the MOPA is nearly unchanged using a 10mW master oscillator or a 100mW master oscillator. The final pass through the second amplifier is approaching a saturated condition and limits the output power to about 1000W of peak power. Additional output cannot be obtained without using larger Nd:YAG rods with a higher saturation intensity. A typical single-pass gain profile is shown in Figure 3-24. This profile tends to get noticeably "sharper" because each pass is a multiplication procedure that preserves the peak and attenuates the edges. This is of little concern provided that the peak provides a reasonable flat region of about 20 microseconds to perform the ultrasonic test.
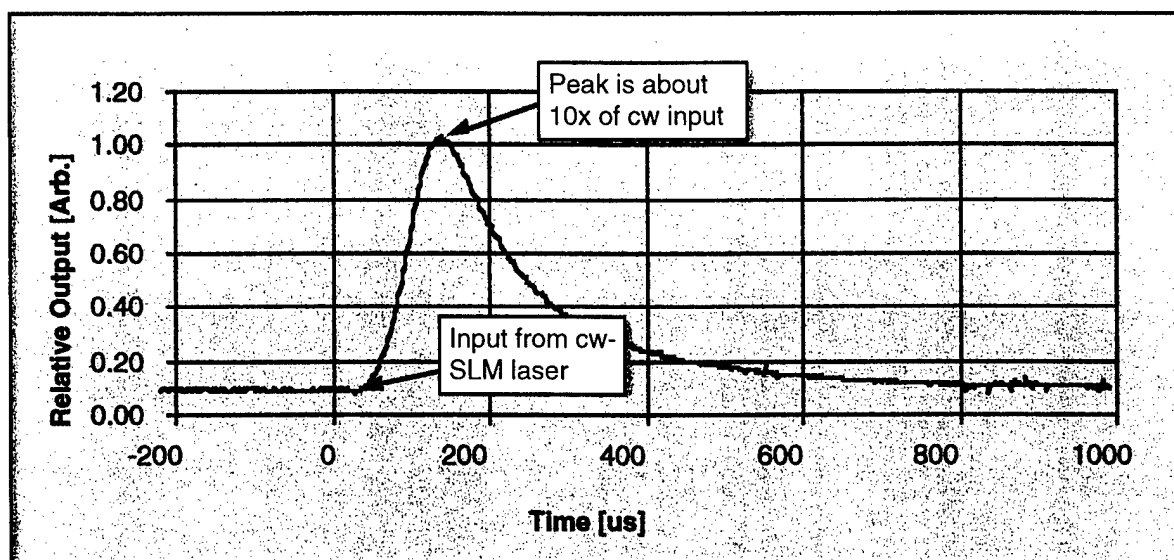
Figure 3-24 Small input single-pass amplification gain is about 10x.

3.2.4.1 Laser Noise

As noted before, the detection laser uses a small single-longitudinal-mode (SLM), continuous wave output Nd:YAG laser as the master oscillator. This laser provides the basic properties that are desirable for the interferometric detection of ultrasound but at too low a power to be practical. The optical amplifiers provide a way to increase the intensity of the laser for a shot duration thus providing a laser with much greater peak power. Unfortunately any noise on the oscillator will be

amplified as well. There are two types of noise to be concerned with: 1) laser intensity (amplitude) fluctuations that occur in the ultrasonic bandwidth, and 2) laser frequency fluctuations that occur in our bandwidth of interest. Amplitude noise is bad but frequency noise could be disastrous. With common-mode noise reduction techniques we have a chance of removing laser amplitude noise but frequency noise would be indistinguishable from the real signals.

We have had experience with both types of noise while constructing the Laser UT prototype. Any noise that is above detector shot noise is by definition measurable and is of great concern. The oscillator has a major source of narrow frequency noise around 500kHz due to relaxation oscillations. This phenomenon is present in all solid state lasers, and occurs because no pump source can be totally free of noise. If the intensity of the pump source changes, the Nd:YAG output cannot respond instantly and will overshoot the new steady state level. This give and take will occur at the characteristic frequency of the laser known as the relaxation oscillation frequency. This noise "spike" can be managed using closed-loop feedback techniques.

Although the relaxation oscillation noise is typically below our frequency of interest, it is still very important that it be managed. This is because limited dynamic range digitizers (typically only 8-bits) must faithfully sample this large noise and the small signals which are "riding" on the low-frequency noise. Analog filters can be used to discriminate out this low frequency noise but high-pass filters always suffer from some degree of undesirable ringing effects. The best approach is to reduce the noise down to the level of the broadband laser noise. Figure 3-25 shows how the characteristic relaxation oscillation "spike" appears with and without the noise reduction circuit enabled.

Range: 10 dBm   Oversweep: On   4-Dec-1995   15: 16
Res BW: 17 000 Hz   VBW: Off   Swp Time: 17.6 mSec
A: D6   Mkr   675 000 Hz   -31.15 dBm
B: D7   Mkr   675 000 Hz   -24.24 dBm

10
dBm
10
dBm
LogMag
10
dB
/div
LogMag
10
dB
/div
-90
dBm
-90
dBm

Relaxation oscillation noise
Noise caused by laser microprocessor interference
Noise reduction enabled
Shot Noise

Start: 0 Hz   Stop: 10 000 000 Hz
Start: 0 Hz   Stop: 10 000 000 Hz
AVERAGING   AVG: 10

Figure 3-25 Spectrum of laser noise (DC to 10MHz) measured at the interferometer.

Figure 3-25 also shows that the laser noise is approaching shot noise limits around 10MHz. Unfortunately, the 1MHz to 5MHz does have laser amplitude noise even with the noise reduction circuitry enabled. Another noise problem was discovered only after the laser light passed through the interferometer. This was determined to be a frequency dependent noise problem. It was evident as narrow oscillations on the interferometer signals in the 2-4MHz region. The problem was eventually traced down to the microprocessor control for the oscillator laser. Figure 3-26 shows the dramatic effect that disconnecting the microprocessor had on the noise of the laser. The manufacturer was unaware of this problem because the frequency-domain noise of the laser had never been measured. Most laser users are only concerned with intensity fluctuation and not with fre-

quency fluctuations. The microprocessor was permanently disconnected.

```
Range:   -10  dBm        Oversweep:  On              4-Dec-1995    15: 07
Res BW:  17  000  Hz     VBW:  Off                   Swp  Time:  17.6  mSec
A: D2                    Mkr             675  000  Hz       -29.42  dBm
B: D4                    Mkr             675  000  Hz       -31.44  dBm
```
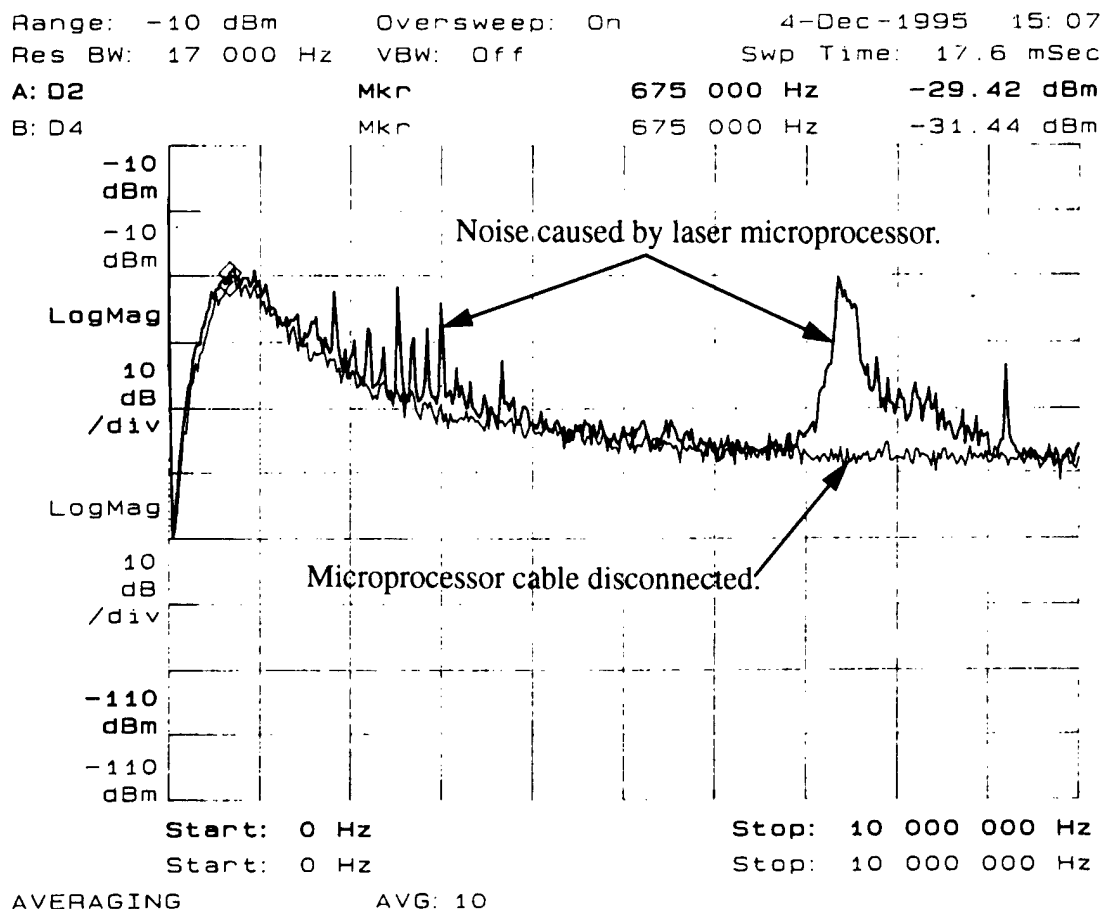
Figure 3-26 These noise spikes were only detected on interferometer signals.

3.2.4.2 Surface Reflectance and Electo-Optic Intensity Controller

There is no definition of a "typical" surface that a Laser UT system must be capable of testing. The extremes range from very dark diffuse surfaces to high-gloss painted surfaces. Each of these represents a problem that must be properly managed. The next three plots (Figures 3-27, 3-28, 3-29) show the total amount of light that is reflected from a composite surfaces when measured with an integrating sphere spectrometer. Note that they all reflect about the same amount, between 11.3% and 13.9%, independent of the condition of the surfaces.

Corrected Total Hemispherical Reflectance: Graphite Epoxy

MAX=100.00 T   MAX=100.00 T

R(1060)=11.2%

MIN=0.00 T   MIN=0.00 T
500   1000   1500   2000   NM   2500
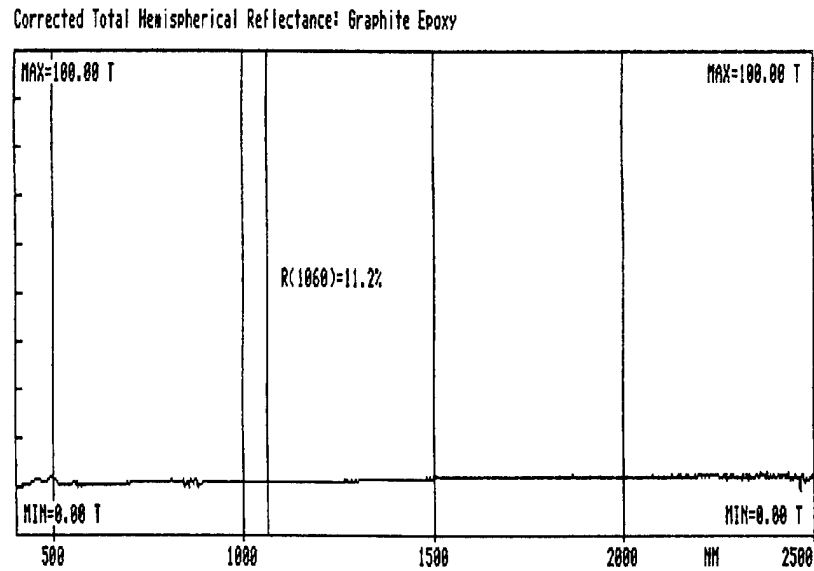
Figure 3-27 Integrating sphere reflectance for bare Gr/Ep is 11.2% for Nd:YAG.

Corrected Total Hemispherical Reflectance: Rough Peel Ply

MAX=100.00 T   MAX=100.00 T

R(1060)=12.6%

MIN=0.00 T   MIN=0.00 T
500   1000   1500   2000   NM   2500
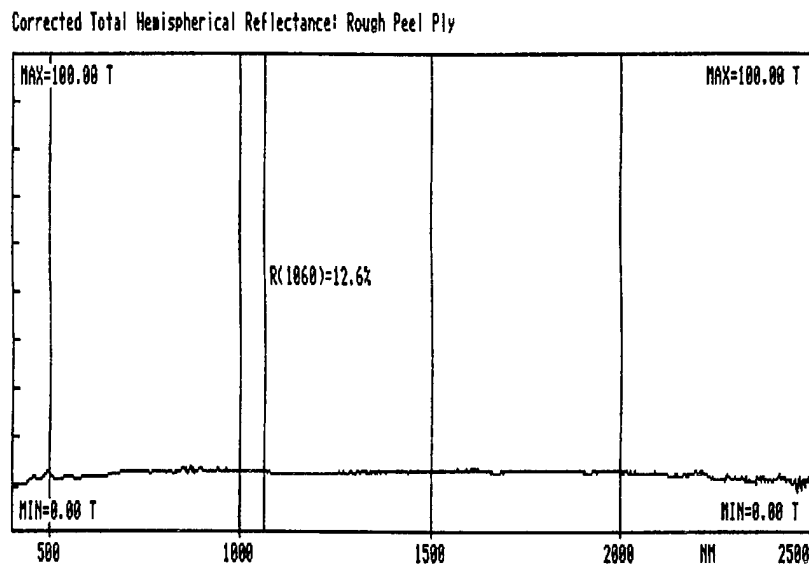
Figure 3-28 The rough peel-ply reflected 12.6% of the Nd:YAG wavelength.

49

Corrected Total Hemispherical Reflectance: Smooth Peel Ply
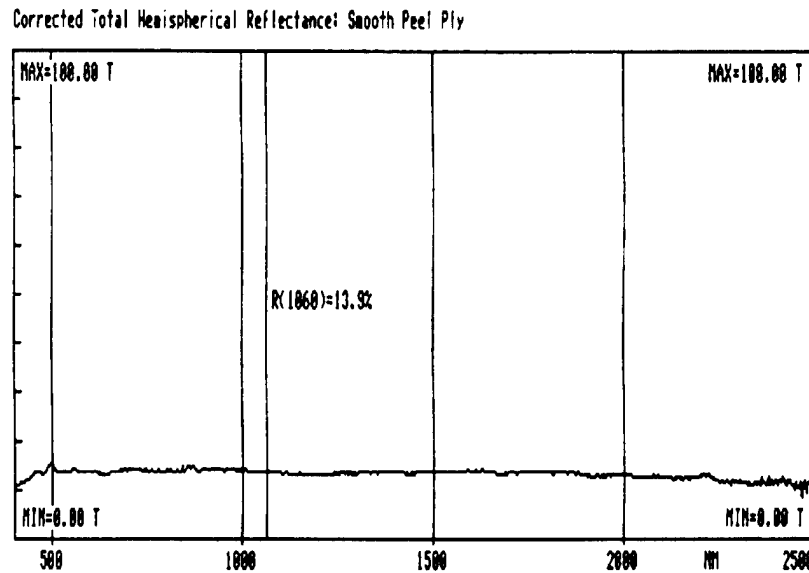
Figure 3-29 The smooth peel-ply reflected almost 14% of the light.

The amount of light collected from an ideal diffuse target can be described by:

$$I(r,\theta) = (1-A) \cdot \frac{I_0}{4} \cdot \left[\frac{\Phi}{r}\right]^2 \cos\theta \qquad (3.2.4\text{-}1)$$

where, A is the absorption of the incident laser power I_0, Φ is the collection aperture at a distance r from the surface, and θ is the angle between the optical axis and the surface normal. This ideal example has a well behaved cosine angular dependence that is rarely observed with real composite surfaces. As a starting point for understanding this problem we measured the reflectance of an ideal white diffuse target and compared the results with Equation 3.2.4-1 as plotted in Figure 3-30. This type of surface shows a characteristic gradual decrease in the amount of light gathered from the target as the angle of incidence is increased as predicted.
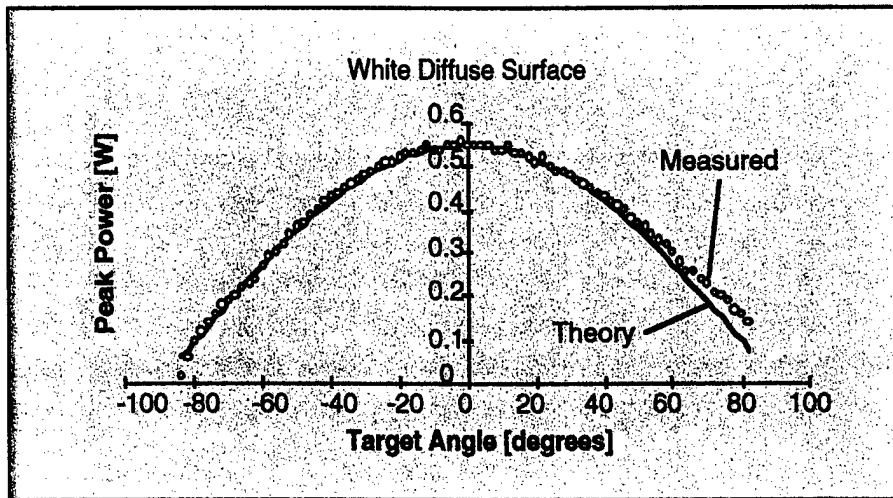
Figure 3-30 The measured reflectance of an ideal diffuse surface matches theory.

The next test was to collect light from an optically dark and rough Gr/Ep test part shown in Figure 3-31. Note that the light intensity is about a factor of 100 below the white surface. The curve still shows a gradual decrease in light collection as the angle of incidence is increased. A third test result is shown in Figure 3-32 for a Gr/Ep test part with a smooth peel ply surface. In this case note the extreme peak near the on-axis position. This is called specular (mirror-like) and is just the opposite of diffuse. In this example the on-axis specular component is about 100-times larger than the off-axis levels.

These plots indicate the large dynamic range that a laser UT system must have to accommodate the extreme changes in light levels as different surfaces are scanned. Diffuse targets are preferred because a small and gradual change in light level is experienced as the laser beams are indexed across the surface. The only concern for a diffuse surface is the absolute amount of light collected which is what scales the size of the collection aperture and power of the detection laser. Specular surfaces in comparison are very problematic. These surfaces often show very weak light intensities off-axis, often below levels found with very dark diffuse materials, and on-axis intensities so

FZM-8250-19

large that damage of the photodetectors and electronics is a possibility.
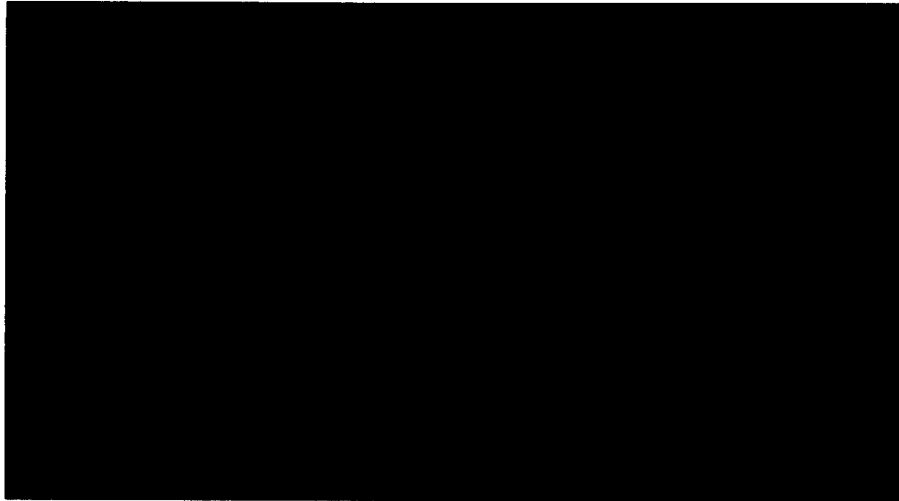
Figure 3-31 Reflectance is dominated by diffuse characteristics for "rough" surfaces.

Figure 3-32 The tool-side (smooth) surface has a very strong specular component.

These extreme surface conditions can be partially managed by using a real-time laser intensity controller to increase the intensity in dark regions and reduce the level in extremely bright conditions. This system must have the dynamic range to cover the types of materials noted and the

52

response to make adjustments at the pulse repetition frequency of 100Hz.
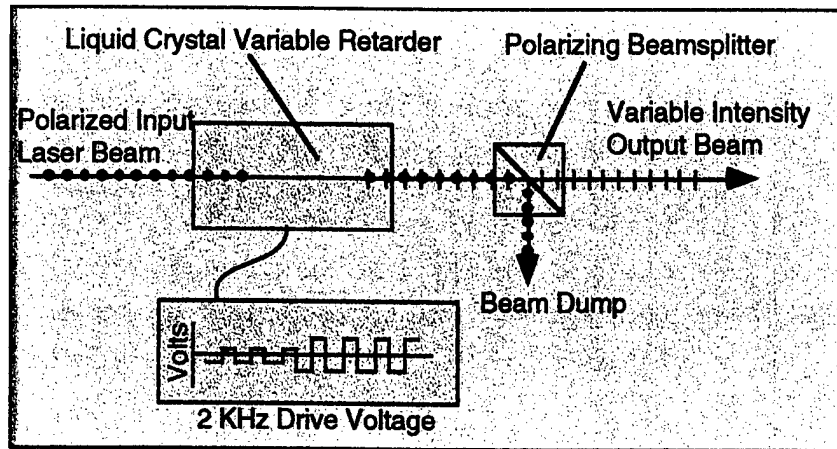
Figure 3-33 Schematic of the real-time detection laser intensity controller.

Figure 3-33 is a schematic of the intensity controller and the drive signal used for the Laser UT prototype system. This system uses a liquid crystal variable retarder (also referred to as a liquid crystal light valve LCLV) manufactured by Meadowlark Optics to rotate the plane of polarization of the input laser beam. The LCLV device retards one optical axis relative to the second axis with the application of a 2 KHz square wave voltage. This modifies the polarized input beam into any arbitrary polarization state at the output. A polarizing beamsplitter then resolves this output beam into horizontal and vertical components. The vertical part is dumped and the horizontal component is sent to the composite surface.

The actual drive voltage is a highly non-linear response curve. The desired intensity level is computed based on the level of the previous pulse and the drive voltage is adjusted to provide the proper laser intensity. The transmission function of the intensity controller arrangement must be measured to assure accuracy. The setup shown in Figure 3-34 was used to test the intensity controller arrangement. The results are shown in Figure 3-35 along with the polynomial curve fit used by the computer to control the intensity in real-time. This configuration had a measured dynamic range of 350:1 which is adequate for most materials.
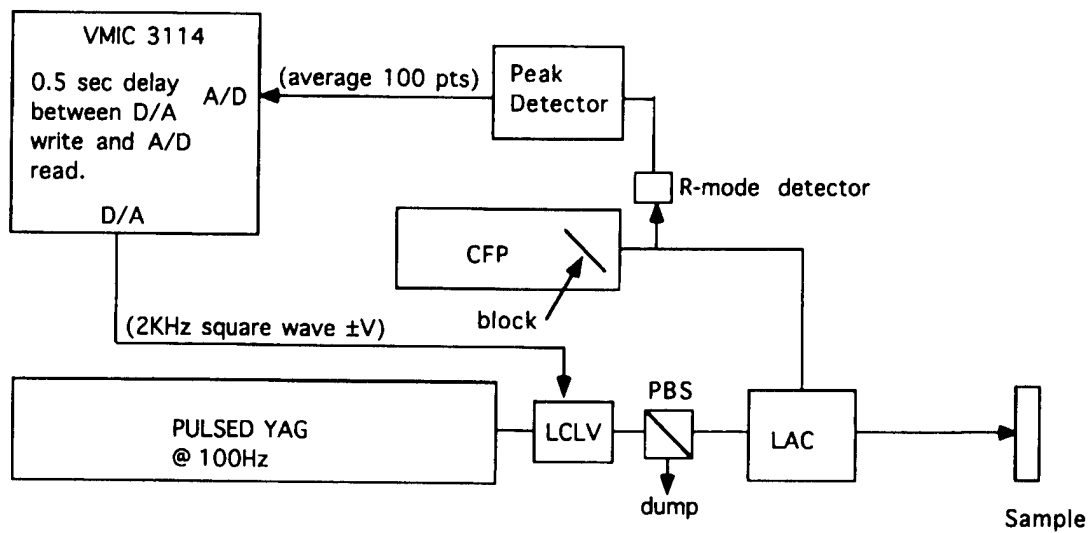
Figure 3-34 Intensity controller test arrangement.

The figure shows a graph with the equation:

$$y = -2869.907x^9 + 13522.325x^8 - 27103.017x^7 + 30153.235x^6 - 20393.656x^5 + 8649.481x^4 - 2300.762x^3 + 377.645x^2 - 38.781x + 4.887 \quad r = 0.999$$

Curve fit was limited to voltages between 1.6 and 5.0 vlots.

Normalized LCLV transmission test:
1) average of 4 tests
2) data smoothed by a 5 channel binomial function
3) normalized to max transmission value.

Y-axis: LCLV Drive Voltage [2KHz square wave: ±V]
X-axis: Transmission

Figure 3-35 Transmission is a non-linear function of drive voltage.

3.2.5 Dual-Differential Confocal Fabry-Perot (DD-CFP) Interferometer

3.2.5.1 General Design Considerations and Construction

The optical detection of ultrasound requires a very sensitive interferometric measurement system that can accept light from an optically rough target. There are only two issues that define the sensitivity performance of an interferometer for this application: 1) the absolute response function in the bandwidth of interest, and 2) the amount of light that the device can accept from a diffuse target. Most interferometers suffer from very small light gathering capacity (etendue) and are therefore unacceptable for the purpose of detecting ultrasound in an industrial environment. The SNR of the system improves as the square root of the amount of light that reaches the optical detectors. Therefore a device that can use more light will provide an improved SNR. The confocal Fabry-

Perot (CFP) can view an extended source and provide the necessary sensitivity to make the detection of ultrasound practical. In fact our modified dual-differential CFP is within a factor of two of the maximum possible sensitivity and can accept all the light that can be collected with the 300mm aperture LAC.

The LMTAS prototype uses a modified "differential" CFP (Figure 3-36) which has the distinguishing feature of improved SNR due to the rejection of common-mode noise. This design also makes use of two CFP cavities to further improve the SNR by doubling the amount of light used. This custom design is based primarily on work done under previous IR&D programs where we discovered that the amplitude noise on the detection laser can become the dominate noise term for high SNR designs. From this previous work we knew that a single CFP could be operated in a differential manner that would produce signals 180 degrees out of phase but the amplitude noise would remain in-phase. The differential signals can be subtracted to reject the common-mode laser amplitude noise.
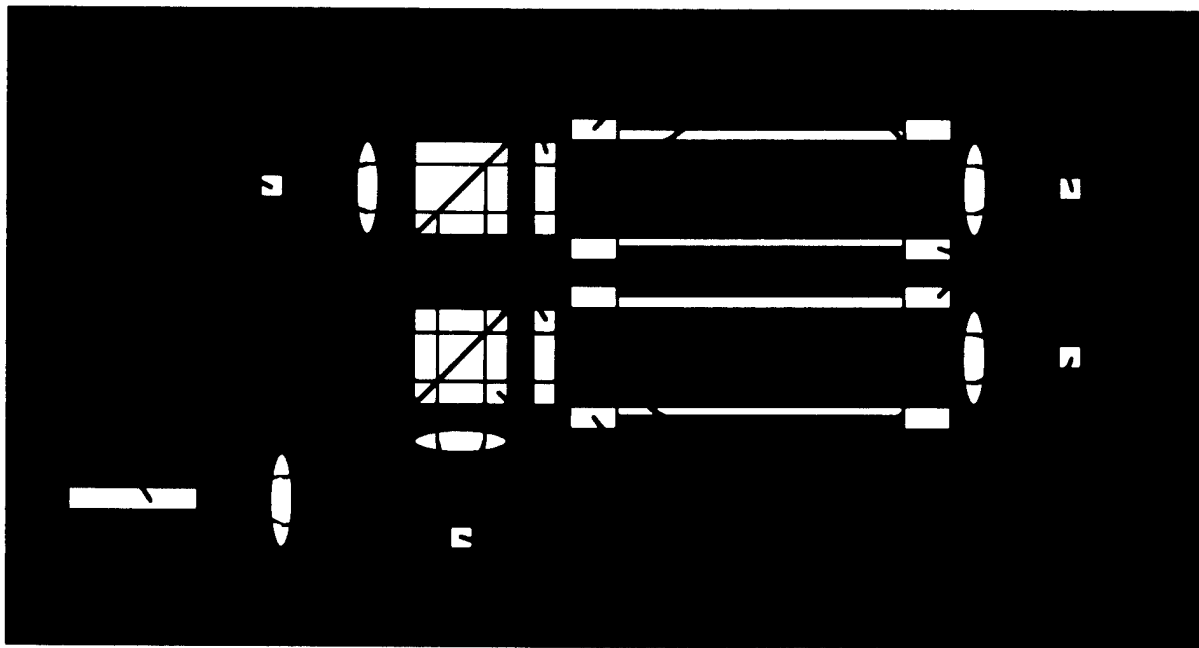
Figure 3-36 Optical configuration for the DD-CFP interferometer.

The DD-CFP was constructed to maintain the distance between the two 50mm mirrors exactly equal to their radii of curvature. This is the definition of confocal. One of the mirrors is mounted in an adjustable focus assembly so that the exact confocal condition is obtained and the second mirror is mounted in a piezoelectric mount. This second mount provides precise cavity length adjustments to a fraction of a nanometer. The DD-CFP structure (Figure 3-37) is fabricated from a combination of invar, aluminum, and phenolic materials. Vibration isolation is provided by the four rubber mounting adapters. The entire cavity is enclosed using an insulated aluminum cover to minimize external acoustical or thermal effects.

Light is coupled from the LAC to the DD-CFP with a fiber optic cable. Spherical aberrations of the CFP will limit the fiber optic core size that can be viewed. Our design can use a 1000um core fiber with a numerical aperture of 0.4 without any aberration problems. This was sufficient for the desired performance and the CFP did not require additional modifications to remove or minimize these aberrations.
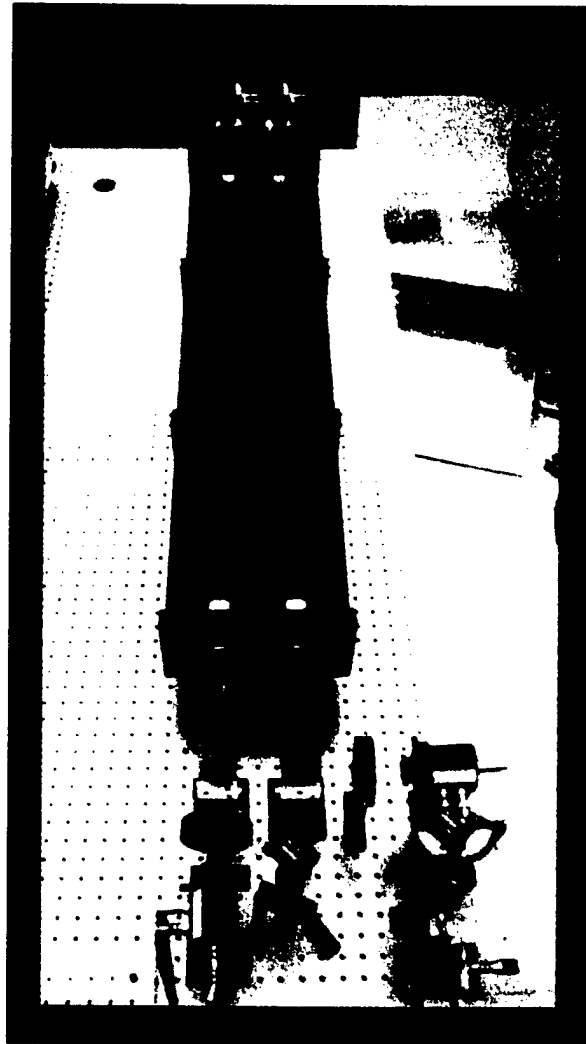
Figure 3-37 This photograph shows the interferometer without the top plate and cover.

The DD-CFP design produces four optical ports: 1) cavity-1 transmission, 2) cavity-1 reflection, 3) cavity-2 transmission, and 4) cavity-2 reflection. A photograph of the reflection side of the interferometer is shown in Figure 3-38. This shows the input fiber optic and the polarization optics necessary to extract the light from the various optical paths. The light from the four optical ports is focused onto the detectors where the stabilization information and the ultrasonic signal are extracted. Closed-loop feedback control methods maintain the length of the cavity such that it is always tuned to the frequency of the laser. The detector circuits are described in Section 3.2.5.5.
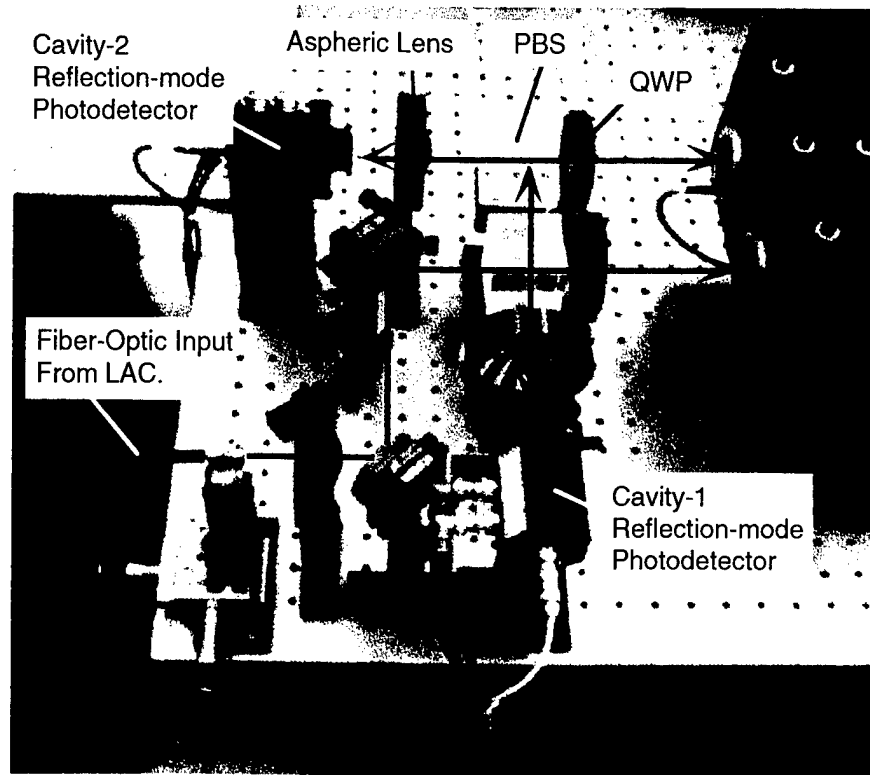
Figure 3-38 The interferometer is "decoupled" form the LAC by fiber optics.

3.2.5.2 Theory of Operation

The confocal Fabry-Perot provides a reentrant path in the paraxial approximation when the separation between the two partially reflective mirrors is exactly equal to their radii of curvature. Figure 3-39 shows the four possible paths that light can follow through the cavity. In practice the cavity length h is manually adjusted to the confocal position by observing the output as discussed later in this section. Fine length adjustments are made by mounting one of the mirrors in a piezoelectric holder that is electrically controlled. This allows real-time control of the cavity length to fractions of a nanometer. Our design uses a piezoelectric material with a sensitivity of 6nm/volt which provides a very high resolution of cavity length positioning.

Figure 3-39 Reentrant ray paths of a confocal Fabry-Perot interferometer.

First consider the electric field representation of plane wave of light as a function of time (t) and position (x) as:

$$E_{input} = E_0 \cdot e^{i(\omega t - kx)} \tag{3.2.5-1}$$

where E_0 is the amplitude of the field, ω is the angular frequency, and k is the wave vector defined as:

$$k = \frac{2\pi}{\lambda}. \tag{3.2.5-2}$$

The amount of "type-1" transmission (T1) through the interferometer will be the infinite series summation of the individual electric field amplitudes.

$$E_{T1} = \sum E_i \tag{3.2.5-3}$$

This can be expressed as follows:

$$E_{T1} = E_0 (tt') e^{i(\omega t_0 - kx_0)} + E_0 (tt') r^4 e^{i[\omega(t_0 - \tau) - kx_0]} \\ + E_0 (tt') r^8 e^{i[\omega(t_0 - 2\tau) - kx_0]} + ... \tag{3.2.5-4}$$

where t is the air-mirror transmission coefficient, t' is the mirror-air transmission coefficient, r is

the air-mirror reflection coefficient, and τ is the time delay between each transmission. Here we have assigned an arbitrary time t_0 and position x_0 to observe the total electric field amplitude. The time delay for each round trip, in the paraxial approximation, through the interferometer is defined as:

$$\tau = \frac{4(h+\varepsilon)}{c} \tag{3.2.5-5}$$

where h is the length of the cavity (e.g. 1-meter), ε is the fine length adjustment on the order of nanometers, and c is the velocity of light. For a 1-meter cavity this delay is 13.33 nanoseconds. It is important to note that the phase interference can only occur because each successive round trip through the interferometer follows exactly the same path (reentrant). This in effect mixes the light with itself but with a fixed time delay. The T1 transmission output can be expressed as the following infinite series.

$$E_{T1} = E_0(tt')\left[\sum_{n=0}^{\infty}(r^4 e^{-i\omega\tau})^n\right]e^{i(\omega t_0 - kx_0)}. \tag{3.2.5-6}$$

Recalling the binomial series

$$1 + x + x^2 + x^3 + \dots = \sum_{n=0}^{\infty} x^n = (1-x)^{-1} \qquad \text{for } (x^2 < 1) \tag{3.2.5-7}$$

reduces equation 2.2.5-6 to the following expression

$$E_{T1} = E_0(tt')[1 - r^4 e^{-i\omega\tau}]^{-1} e^{i(\omega t_0 - kx_0)}. \tag{3.2.5-8}$$

Other derivations will be simplified in notation if the equation is rewritten as:

$$E_{T1} = E_0\beta(\omega\tau) e^{i(\omega t_0 - kx_0)} \tag{3.2.5-9}$$

$$\beta(\omega\tau) = \frac{T}{1 - R^2 e^{-i\omega\tau}} \tag{3.2.5-10}$$

where T is the transmission coefficient and R is the reflection coefficient for the two mirrors, M1 and M2, which are assumed to be the same. In most cases we can substitute the expression $T = 1 - R$ if the absorption and scatter from the mirrors is sufficiently low. Also recall that τ is

not a constant but is adjustable with the fine cavity length parameter ε. We can now state the intensity observed by a photodetector will be the time average of the electric field which is simply the square of the magnitude of the T1 electric field transmitted through the interferometer.

$$I_{T1} = \left| E_{T1} \right|^2 \qquad (3.2.5\text{-}11)$$

$$I_{T1} = E_0^2 \left| \beta\,(\omega\tau) \right|^2 = E_0^2 \beta\,(\omega\tau)\,\beta^*(\omega\tau) \qquad (3.2.5\text{-}12)$$

This must be a real result (no imaginary components) and after expansion a closed-form solution for the transmitted intensity is given by:

$$I_{T1} = E_0^2 \frac{T^2}{1 + R^4 - 2R^2 \cos\,(\omega\tau)}. \qquad (3.2.5\text{-}13)$$

An analysis of the T2 transmission intensity will yield the following simple relationship:

$$I_{T2} = R^2 \cdot I_{T1}. \qquad (3.2.5\text{-}14)$$

We now have derived the total light (at a fixed frequency ω) that a photodetector would observe passing through the interferometer as a function of the mirror reflectivity and the length of the cavity.

$$I_T = I_{T1} + I_{T2} = E_0^2\,(1 + R^2)\,\left| \beta\,(\omega\tau) \right|^2. \qquad (3.2.5\text{-}15)$$

The R1 reflection out of the interferometer has a slightly different form due to the introduction of some portion of light that reflected off of the first mirror and never entered the cavity

$$E_{R1} = E_0\,[\,r'e^{i\omega t_0} + (tt')\,r^3 e^{i\omega(t_0 - \tau)} + (tt')\,r^7 e^{i\omega(t_0 - 2\tau)} + ...\,]\,. \qquad (3.2.5\text{-}16)$$

where r' denotes the mirror-air electric field reflection coefficient. We can reduce this infinite series by using the fact that there is a change in phase (sign) for the two types of reflecting interfaces.

$$E_{R1} = E_0 r'\,[\,1 - r^2 \beta\,(\omega\tau)\,e^{-i\omega\tau}\,]\,e^{-\omega t_0} \qquad \text{using: } r = -r'. \qquad (3.2.5\text{-}17)$$

Additional simplification is obtained by defining a new function

$$\gamma\,(\omega\tau) = 1 - R\beta\,(\omega\tau)\,e^{-i\omega\tau}. \qquad (3.2.5\text{-}18)$$

The intensity of the R1 reflection is defined by:

$$I_{R1} = E_0^2 R |\gamma(\omega\tau)|^2 . \tag{3.2.5-19}$$

The R2 reflection is similar to the transmission equations and the total intensity observed by a photodetector on the reflection-port of the interferometer is:

$$I_R = I_{R1} + I_{R2} = E_0^2 R [|\gamma(\omega\tau)|^2 + |\beta(\omega\tau)|^2] . \tag{3.2.5-20}$$

The total amount of light that exits out of the interferometer must equal the input intensity, and some algebra proves that:

$$I_T + I_R = E_0^2 (1 + R^2) |\beta(\omega\tau)|^2 + E_0^2 R [|\gamma(\omega\tau)|^2 + |\beta(\omega\tau)|^2] = E_0^2 \tag{3.2.5-21}$$

Figure 3-40 shows reflection and transmission intensity curves for 85 and 95 percent reflectivity mirrors
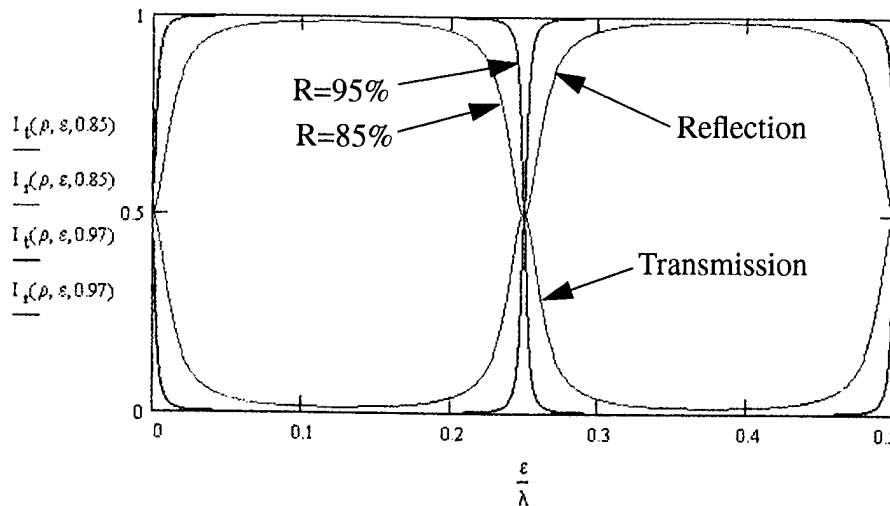
Figure 3-40 Reflection and transmission data vs. cavity length for two designs.

Spherical aberrations will cause fringes to appear in the output of the interferometer as the diameter of the mirrors increases relative to the length of the cavity. This amounts to a small phase shift in the light as a function of radial position given by:

$$\delta \approx \frac{2\pi}{\lambda} \left(\frac{\rho^4}{r^3} + 4\varepsilon \frac{\rho^2}{r^2} + 4\varepsilon \right)$$ (3.2.5-1)

where ρ is the radial position above the optical axis, r is the radius of curvature of the mirrors, and $r + \varepsilon$ is the actual separation of the two mirrors. Figure 3-41 shows the reflected and transmitted intensities as a function of mirror radial height.
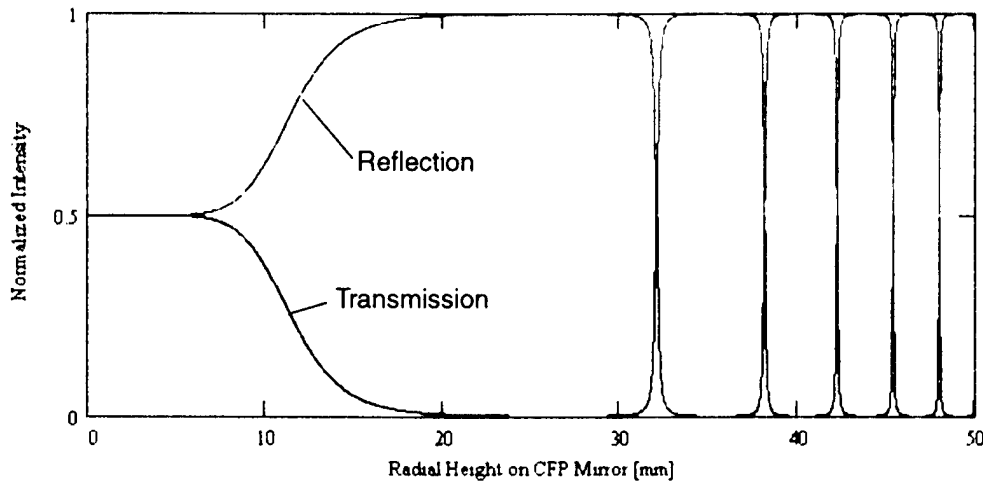
Figure 3-41 Fringe analysis shows maximum usable size of mirrors.

This analysis shows that the central fringe position extends to about 25 mm in diameter, and the next fringe would occur beyond the diameter of the 50 mm mirrors used.

All of the previous derivations have assumed that the incident electric field was not changing in amplitude, frequency or phase during time-scale of the infinite series summation process. We must next understand how a vibrating surface will modulate the scattered laser light and what designs will be most sensitive to detecting these vibrations. First, the unmodulated beam will have the following form:

$$E_{in} = E_0 e^{i(\omega t - k \cdot x)} .$$ (3.2.5-1)

where we are explicitly defining the input wave as a vector. After reflection from a surface that has a time-dependent displacement we have,

$$\boldsymbol{E}_{\text{out}} = E_0 e^{i\,[\,\omega t - \boldsymbol{k}\cdot\hat{x} + \boldsymbol{k}\cdot\hat{x} - 2k\Delta(t)\,]}\,. \tag{3.2.5-2}$$

For small surface displacements the exponential term can be approximated and the following modulation expression is obtained.

$$\boldsymbol{E}_{\text{mod}} = \boldsymbol{E}_{\text{out}} \approx E_0\,[\,1 - 2ik\Delta(t)\,]\,e^{-\omega t} \quad \text{for } \Delta_{\text{max}} \ll \lambda. \tag{3.2.5-3}$$

Following the same procedure as before, the response functions can be derived for the modulated input. The equations are more cumbersome than the previous expressions and the results are presented here in graphical form for two cases. Figures 3-42 and 3-43 show the cavity transmission and reflection magnitude response curves for 85% and 95% reflectivity mirrors, respectively. The tune position was at the 50% point of the transmission port which equates to 25% of the light reaching the transmission detector and 75% of the light on the reflection detector. Note that signal component is a modulation of this DC-level.
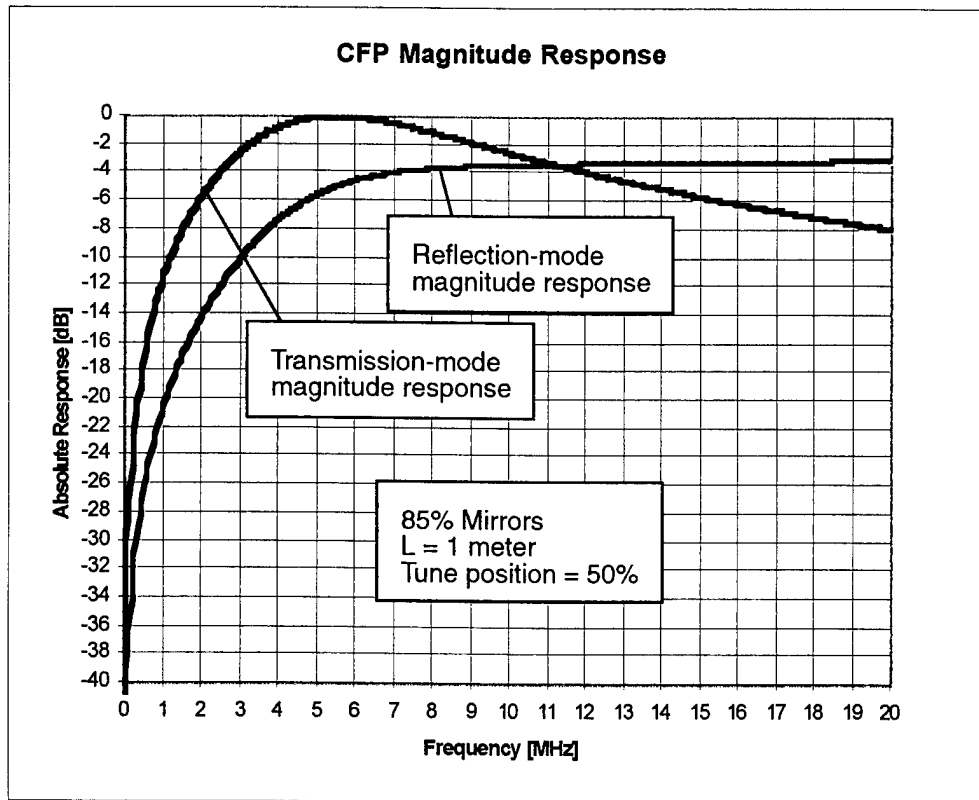
Figure 3-42 Initial design of DD-CFP had good response above 4 MHz.

The 0 dB point is the theoretical limit for the optical detection of ultrasound and is reached in the transmission-mode curves at a single frequency point. Note that the reflection-mode operates at typically 3x the light level of the transmission-mode and the signals are actually larger. However, the reflection-mode has a lower SNR until the point where the signals are 1.73x the amplitude of the transmission-mode (at about 6MHz for the 85% mirrors).
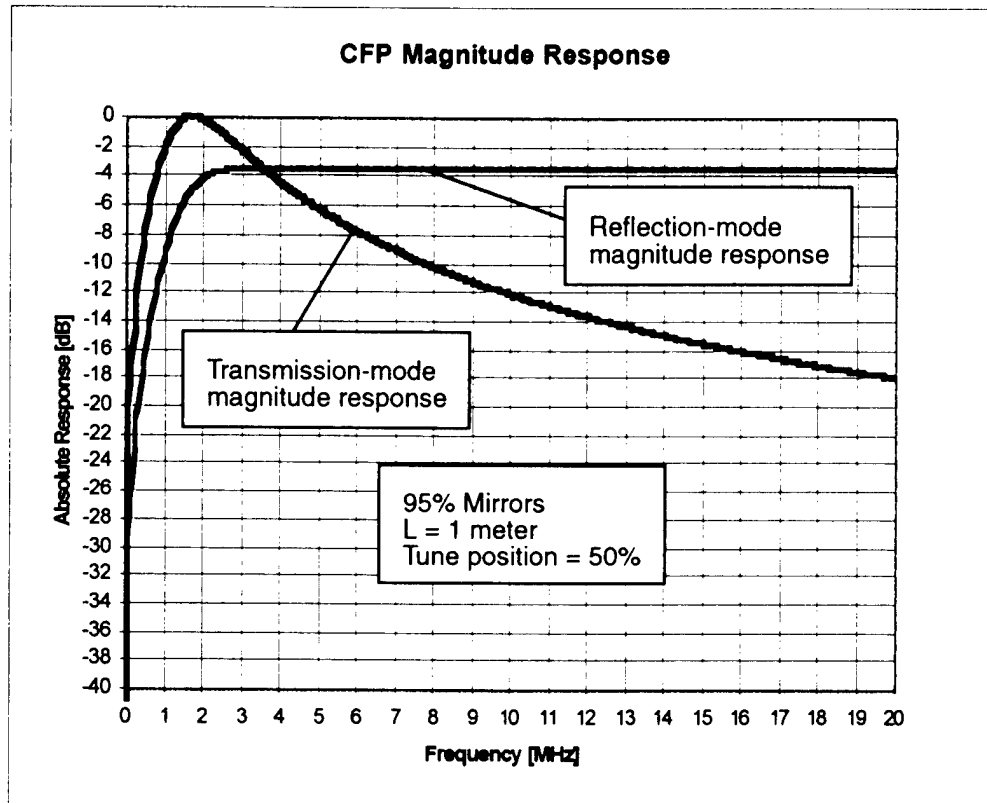
Figure 3-43 Modified DD-CFP improves performance at lower frequencies.

With the proper combination of the signals, it is possible for a DD-CFP to achieve sensitivities from 1MHz to 20MHz that are within 3dB or 4dB of the theoretical limits and can reject common-mode noise. This means there is very little room for improvement in absolute sensitively beyond that provided by the system described here.

There is a practical issue regarding the tuning of the DD-CFP for the best SNR condition. Also of concern is how sensitive the system is to de-tuning effects caused by less than optimal conditions.

The contour plots in Figures 3-44 and 3-45 show the SNR as a function of frequency and linear tune position for the transmission-mode and reflection-modes of operation. A tune position of 0.5 would be half-way up the transmission resonance curve and half-way down the reflection resonance curve as shown in Figure 3-40.
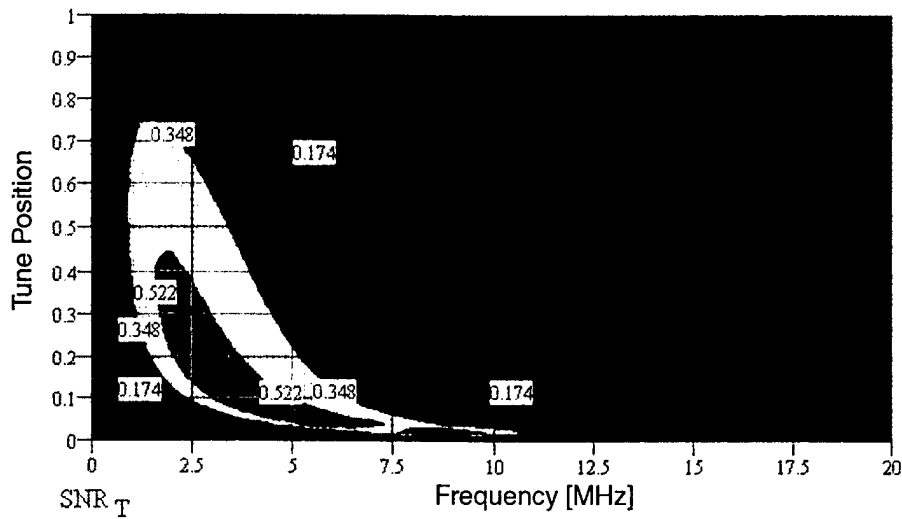
Figure 3-44 Contour plot of DD-CFP transmission-mode SNR.
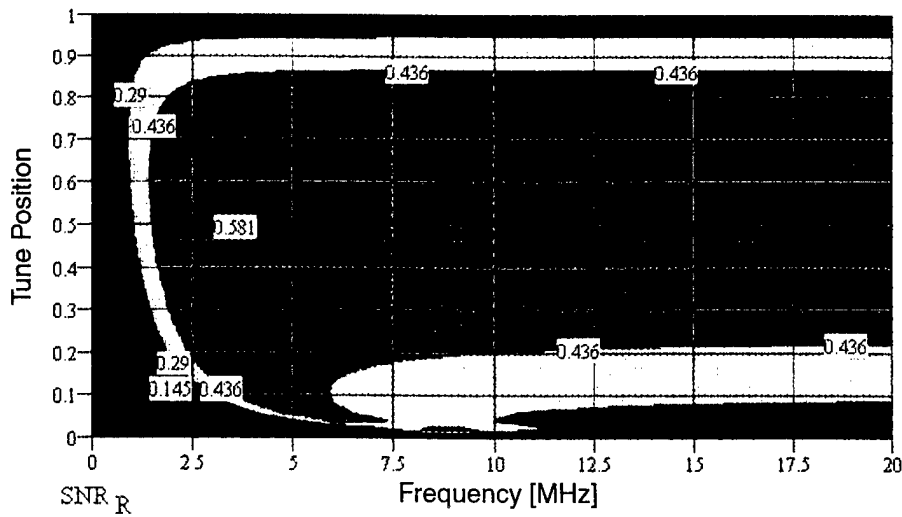
Figure 3-45 Contour plot of DD-CFP reflection-mode SNR.

67

3.2.5.3 Fabry-Perot Spatial Imaging Analysis

Optical fiber bundles were designed for use with spatial imaging to increase the inspection rate. The fiber optic bundles consist of a total of four individual optical fibers. Each fiber has a core/clad diameter of 300mm/330mm (AFS300/330). One fiber bundle is a coherent bundle that will be used to transport light from the image plane of the LAC to the CFP interferometer (see Figure 3-46A). Another fiber bundle with four separated legs (see Figure 3-46B) will be used to transport light from the CFP to four individual photodetectors. With this setup, the light from one laser shot can be imaged into four spots thereby quadrupling the inspection rate. Figure 3-47 is a photograph of the multi-fiber bundle to be used for spatial imaging.
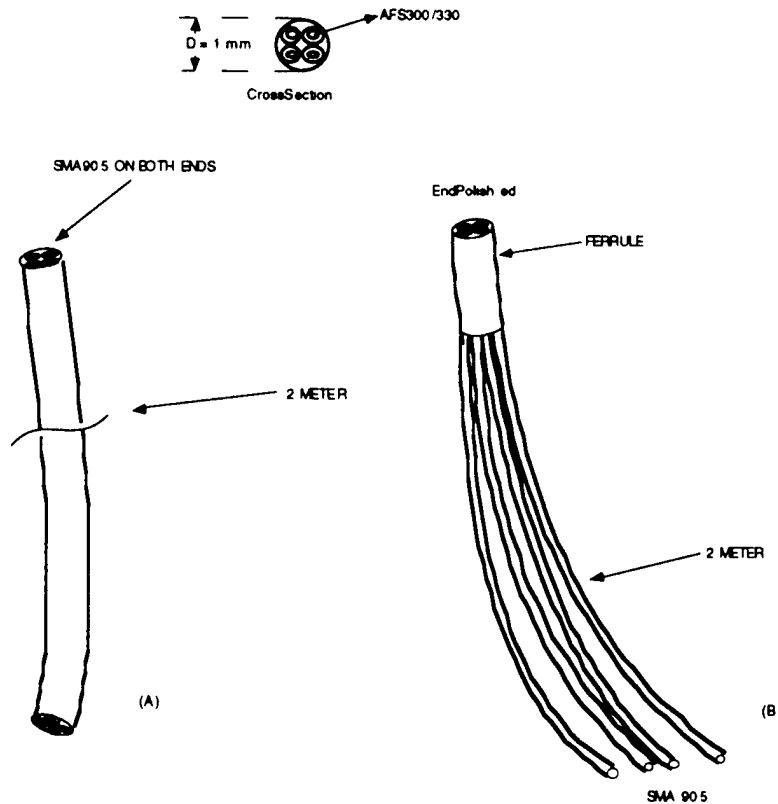
Figure 3-46 Spatial imaging requires two coherent fiber bundles.
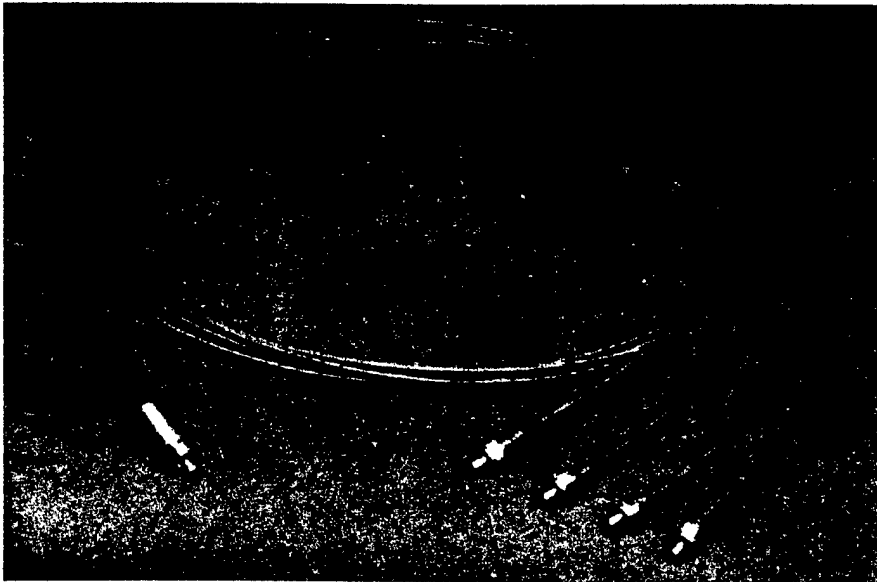
Figure 3-47 Photograph of spatial imaging multi-fiber bundle.

3.2.5.4 Optical Detection of Ultrasound: Signal-to-Noise-Ratio Analysis

Noise in the optical detection process can be associated with many different possible sources. Each noise source is considered as either coherent or incoherent depending on the fundamental process that created the noise. Incoherent noise is by definition a source that will not show any correlation between simultaneous measurements of the event. This just means that the noise is random in nature and independent measurements will not show identical results. Coherent noise, in comparison, will have a very strong correlation between simultaneous measurements. If we assume that a single measurement is performed and there is no correlation between the different noise sources then the distinction between the two types is not important. In this case, the total noise is the square-root of the sum of the squares of each of the noise terms. Any source of noise will dominate if it is 3 to 4 times larger than any other term.
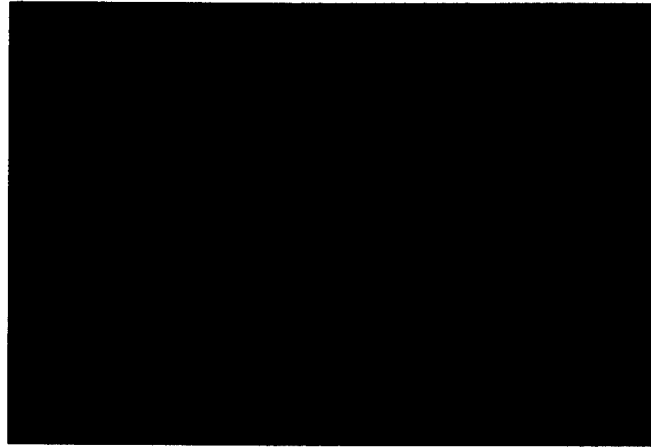
Figure 3-48 Typical configuration for optical detector circuit.

The objective is to maximize the SNR. First consider the signal component. In our analysis we will not consider the actual ultrasonic signal extracted by the interferometer but just the generic signal produced in the optical detection process.

$$V_{signal} = R_f R_\lambda P_D$$

(3.2.5-1)

Here the signal (voltage) is a function of the detector responsivity at the desired wavelength R_λ, the optical power on the detector P_D, and the conversion of the photocurrent produced by the detector with a feedback resistor R_f in an ideal transimpedance amplifier (this could also be a simple load resistor tied to ground).

Next consider quantum or shot noise in the photodetection process. Note that, in all of the noise equations below, the expression is for an equivalent voltage. The actual noise source is a fluctuation in current that we have converted to a voltage by use of a feedback resistor R_f. The only real variables are the choice of R_f and the optical power reaching the detector P_D because the charge of the electron q is a constant, the detector responsivity R_λ does not vary much, and the band-

70

width BW is defined by the frequency content of the ultrasonic signal (about 20 MHz). This noise term is unavoidable and is considered the limit for any optical detection process.

$$V_{\text{shot noise}} = R_f \sqrt{2q R_\lambda P_D BW} \qquad (3.2.5\text{-}2)$$

Johnson, or thermal noise, is a function of Boltzman's constant, the temperature, the value of the resistance, and the bandwidth. This term will be dominate at low light levels. The objective of a good design is to maximize the SNR by increasing R_f because the signal improves linearly with R_f while the noise only increases at $\sqrt{R_f}$ for a net improvement of $\sqrt{R_f}$. Dynamic range limitations will define what the largest value of R_f can be before the signals become too large for the amount of optical power (signal) anticipated.

$$V_{\text{thermal noise}} = \sqrt{4kT R_f BW} \qquad (3.2.5\text{-}3)$$

Noise in the electronics used to amplify the signal can be given either as an equivalent resistance or directly as a voltage value. Either way, the noise is actually just another source of thermal noise. Care is taken in the design to keep this term at or below the R_f term.

$$V_{\text{amp noise}} = (\text{amp voltage noise}) \sqrt{BW} \qquad (3.2.5\text{-}4)$$

All of the above noise terms are incoherent which means that if multiple detectors were operated simultaneously, there would be no correlation between the instantaneous noise value. Laser noise is a coherent corruption of the desired signal. Multiple simultaneous measurements would measure the same amplitude event. Without further processing, there is no distinction between signal and laser noise. They are both time varying optical power intensities reaching the photodetector. The differential confocal Fabry-Perot interferometer can remove laser noise because the desired signals are produced out-of-phase while the noise remains in-phase. For the discussion here we can combine laser noise with the other noise terms because there is no coherence between shot

noise, thermal noise, and laser noise.

$$v_{\text{laser noise}} = R_f R_\lambda \, (\text{laser RIN}) \, P_D \sqrt{BW} \qquad (3.2.5\text{-}5)$$

As noted above, the total noise for uncorrelated sources is the square-root of the sum of the squares (i.e. add the powers and convert back to amplitude).

$$v_{\text{noise}} = \sqrt{(v_{\text{shot}})^2 + (v_{\text{thermal}})^2 + (v_{\text{laser}})^2 + (v_{\text{amp}})^2} \qquad (3.2.5\text{-}6)$$

As an example, the SNR plot shown in Figure 3-49 is for a detector responsivity of $R_{1064\text{nm}} = 0.4 \, \text{amps/watt}$, a feedback resistance $R_f = 2000 \, \Omega$, an amplifier with $1.7 \times 10^{-9} \, \text{volt}/(\sqrt{\text{Hz}})$ noise figure, and an average laser RIN of $-142 \text{dB}/(\sqrt{\text{Hz}})$ over the 10MHz measurement bandwidth.
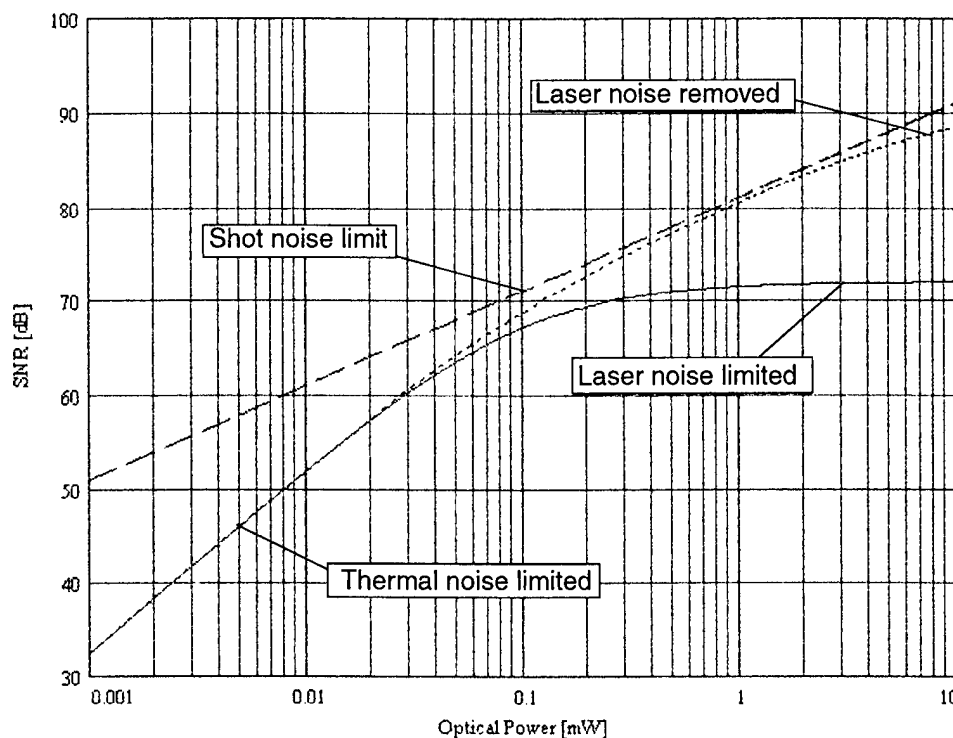
Figure 3-49 The SNR is a function of the electronics, laser, and light level.

This design was clearly chosen to operate at high light levels where laser noise is dominate because thermal noise begins to dominate at optical powers below 100 microwatts. Rejection of common-mode (coherent) laser noise is critical for operating at the higher light intensities shown.

3.2.5.5 Optical Detector Design And Analysis

A low-noise detector circuit was fabricated based on an Analog Devices AD829 operational amplifier with a YAG100A detector in a transimpedance configuration (Figure 3-50). The AD829 has an outstanding input voltage noise of only $1.7 nV/\sqrt{Hz}$, current noise of $1.5 pA/\sqrt{Hz}$, a gain bandwidth product of 750MHz, and can directly drive the 50Ω digitizer up to the required $\pm512mV$.

Analysis of a this circuit shows that Johnson noise in the feedback network is the dominate noise

73

term for this application, and the SNR will improve with the $\sqrt{R}$. A design with a large feedback resistance will improve SNR, however, the circuit must maintain sensitivity to the small ultrasonic signals, while avoiding saturation by the large signals from the Nd:YAG laser pulse. The maximum feedback resistance value is determined by the anticipated light level of the laser pulse and the maximum allowable drive voltage of the circuit. Our design assumes a peak pulse power of 10mW, a detector responsivity of 0.4 A/W and a maximum voltage into a high impedance load of < 10V for the AD829. These criteria indicate that a 2000 Ω feedback load would be appropriate for the detection of the laser pulses.

Instead of a single feedback resistor, a "T" feedback network (Figure 3-50) was used to provide a lower gain at low frequencies and a larger gain at ultrasonic frequencies. This approach gives a single op-amp the dynamic range to measure the large pulse of the Nd:YAG laser without saturation, yet provides the high gain necessary for the ultrasonic signals. Analysis shows that with an appropriate design, the noise limit is established by the low frequency feedback resistance. The "T" network simply removes the need for a second low-noise op-amp and could increase noise if not properly designed.

Figure 3-51 shows the frequency response of the detector circuit in linear and log scales along with the noise performance of the system without incident light. The spectrum analysis shows a response that is flat to within 1dB between 2 and 10 MHz and 3dB between 1 and 16 MHz. As a reference point, the detector background noise figure of -134 dBm/$\sqrt{Hz}$ is equivalent to the shot noise produced by less than 100 μW of laser power. Thus, this system approaches shot-noise-limited performance for optical powers above 100 μW.
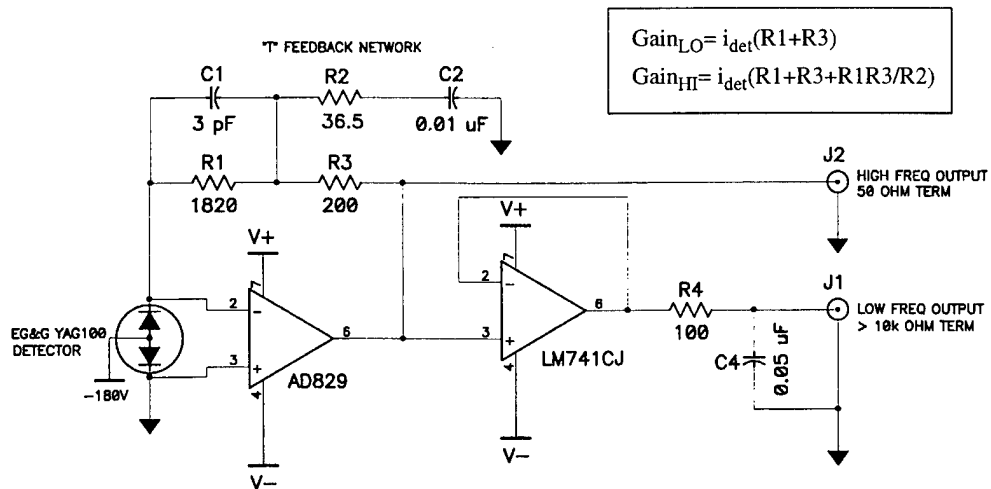
Figure 3-50 Final design of the detector circuit used a T-feedback configuration.
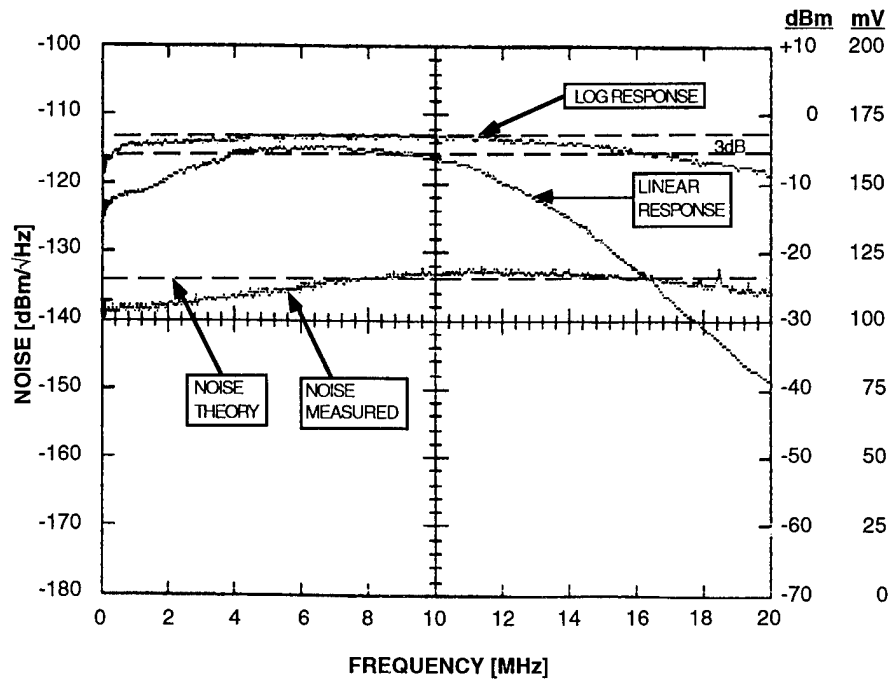
Figure 3-51 Measured noise and frequency responses verified the theory of the design.

3.2.5.6 Performance Testing of DD-CFP

The dual-differential confocal Fabry-Perot (DDCFP) interferometer was tested for absolute sensitivity and compared with theoretical predictions. Some results were not as precise as was hoped due to measurement uncertainties. These measurement problems will be corrected in the future by using phase and amplitude modulators to simulate an ultrasonic signal.

An ultrasonic displacement transducer was designed, constructed, and calibrated for measuring the absolute sensitivity of the DD-CFP. This consisted of a 5MHz ultrasonic transducer bonded to the back of a mirror as shown in Figure 3-52. The small 1-mm aperture assured consistent measurements from the same position on the mirror.
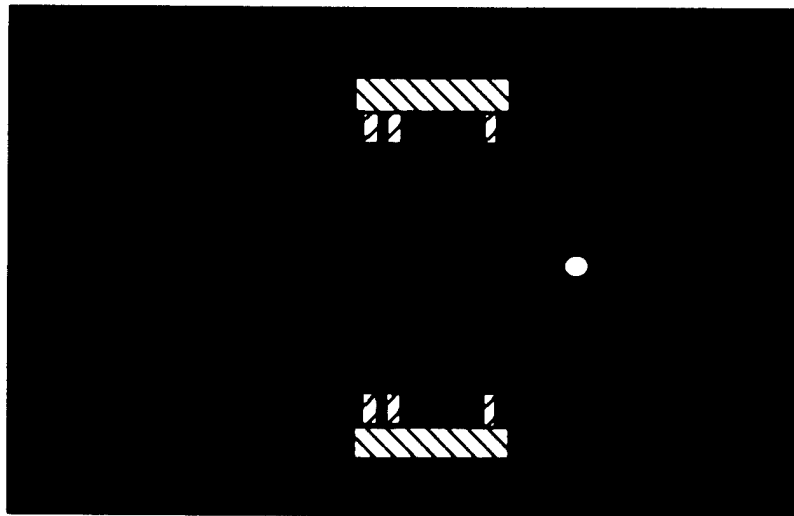
Figure 3-52 Ultrasonic displacement transducer used to test the interferometer.

A computer-controlled Michelson interferometer was constructed for primary calibration of the transducer assembly. The test setup used is shown in Figure 3-53.
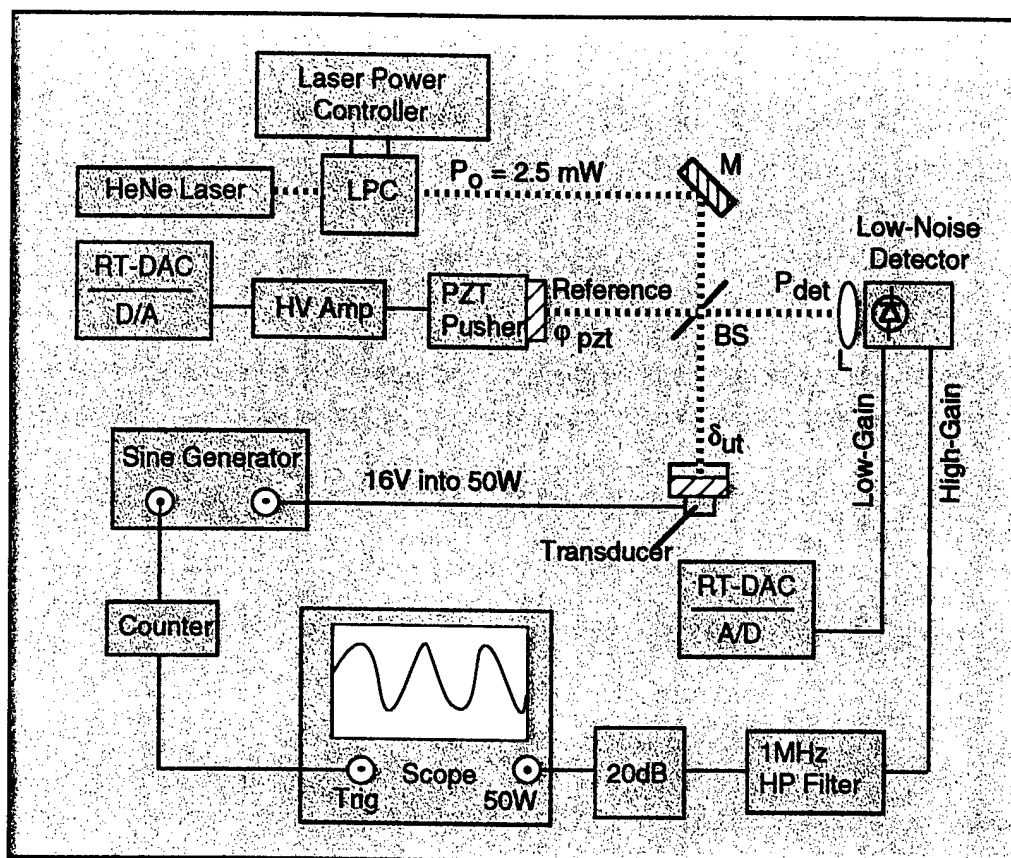
Figure 3-53 The transducer was calibrated with a Michelson interferometer.

The Michelson interferometer will produce the following power intensity at the detector:

$$(3.2.5\text{-}1)$$

$$P_{det} = \frac{1}{2} P_o \left[1 + \cos (\Delta\Phi) \right]$$

$$(3.2.5\text{-}2)$$

$$(3.2.5\text{-}3)$$

Where P_{det} is power at the detector, P_o is the power incident on the interferometer, and $\Delta\Phi$ is the phase difference between the reference and sample beams mixing at the detector plane. For this test arrangement the phase term will be modulated by the transducer mirror as $\Delta\Phi = 2k\delta_{ut} + \varphi_{pzt}$ giving:

$$P_{det} = \frac{1}{2}P_o \left[1 + \cos\left(2k\delta_{ut}\right)\cos\left(\varphi_{pzt}\right) - \sin\left(2k\delta_{ut}\right)\sin\left(\varphi_{pzt}\right) \right] \qquad (3.2.5\text{-}4)$$

$$(3.2.5\text{-}5)$$

Where $k = 2\frac{\pi}{\lambda}$ is the usual wave vector term, λ is the laser wavelength, δ_{ut} is the displacement

of the transducer mirror, and φ_{pzt} is the phase difference between the reference path length and

the transducer path length. The piezoelectric PZT pusher in the reference arm of the interferome-

ter is computer controlled by the RT-DAC to maintain the relative path difference such that

$\varphi_{pzt} = \frac{n\pi}{2}$, where n is any integer. This is called the quadrature position of the interferometer and

is the most sensitive operating point. The quadrature condition now has the following response

function:

$$P_{det} = \frac{1}{2}P_o \left[1 \pm \sin\left(2k\delta_{ut}\right) \right] \qquad (3.2.5\text{-}6)$$

The sign is determined by which of the two possible quadrature conditions are satisfied (odd or

even integer solution). If the transducer mirror displacement is such that $\delta_{ut} \ll \lambda$, then:

$$P_{det} = \frac{1}{2}P_o \left[1 \pm \frac{4\pi\delta_{ut}}{\lambda} \right] \qquad (3.2.5\text{-}7)$$

The Michelson interferometer response function contains a DC term and a modulation term that is

linear with displacement. Note that the response is not frequency dependent and has no phase dis-

tortion. If the transducer is driven by a sine wave generator then $\delta_{ut} = U(\omega)\sin\left(\omega t\right)$ and Equa-

tion 3.2.5-7 can be solved for the displacement response function $U(\omega)$. This completes the

calibration of the transducer amplitude as a function of frequency.

The response of the DDCFP interferometer was tested by reflecting a low-power Nd:YAG laser

off of the calibrated transducer mirror and coupling the modulated beam into the interferometer.

Figure 3-54 shows the ratio of the reflected-mode interferometer amplitude response relative to

the transmission signal. Note the close agreement to theory. The interferometer was stabilized such that 25% of the light was transmitted and 75% reflected, thus the SNR will be the same for both modes at the point the amplitude response ratio is $\sqrt{3}$ (recall that shot-noise is proportional to the square root of the DC intensity). This SNR crossover between the two modes occurs near 6MHz.
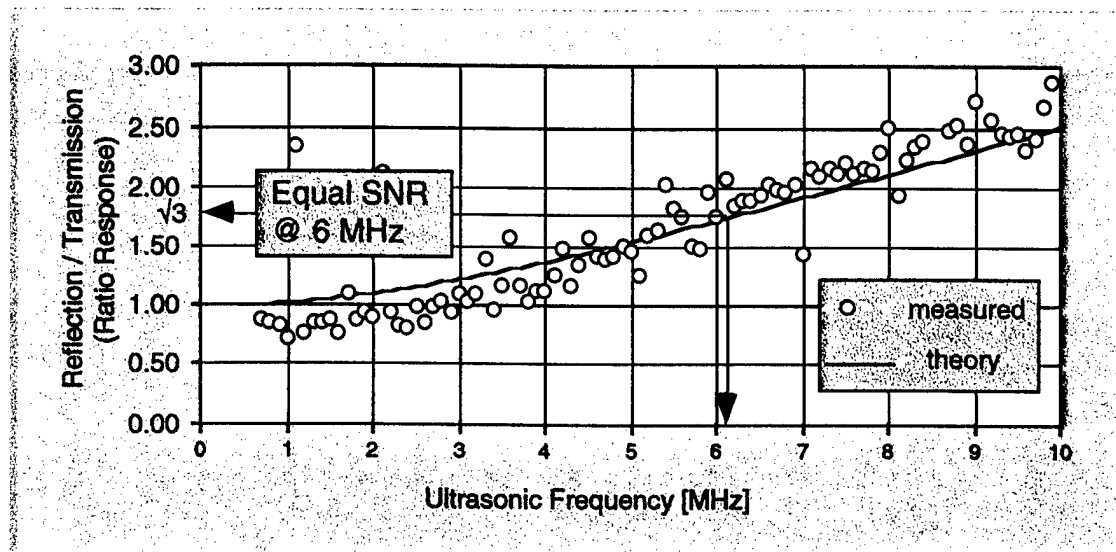
Figure 3-54 The relative amplitude response shows good agreement with theory.

Figure 3-55 is the delta phase response of the transmission-mode relative to the reflected-mode. Accurate phase data is necessary for removing distortions prior to the differential combination of the reflection-mode and transmission-mode data. The phase measurements did not agree with the original theory nearly as well as the amplitude response. There is little error at low frequencies, but the difference reaches about 35° above 6MHz. We discovered an error in the original calculations that did not account for the time delay between the reflection-mode and transmission-mode signals. The modified theory corrected this problem.
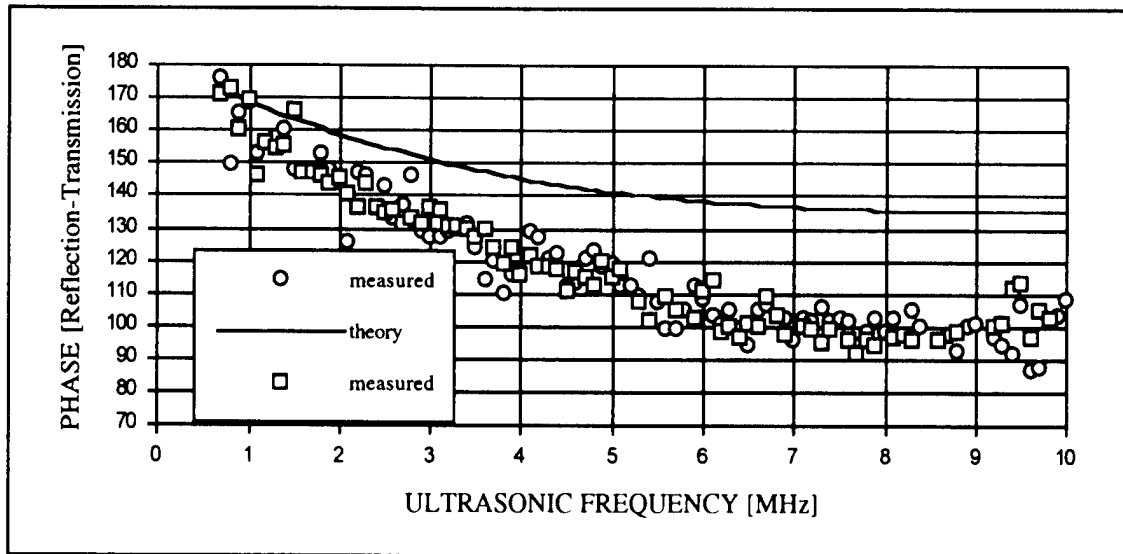
Figure 3-55 Transmission-Mode Phase Response

The absolute amplitude response of the interferometer was measured and is shown in Figure 3-56. The transmission-mode (U_{trans}) and reflection-mode (U_{refl}) plots represent the computed displacements using the theoretical response functions to convert the measured signals into absolute displacement. If this theory is correct, the amplitude values will match the U_{cal} determined from calibration of the transducer with the Michelson interferometer, as discussed above. The large oscillations are caused by undamped resonance of the mirror and are unimportant for this analysis. The DD-CFP data does generally match with the predicted values, but some variances are noted.

Figure 3-56 Absolute measurements were complicated by transducer resonance.

3.3 DATA ACQUISITION AND COMPUTATIONAL SYSTEMS
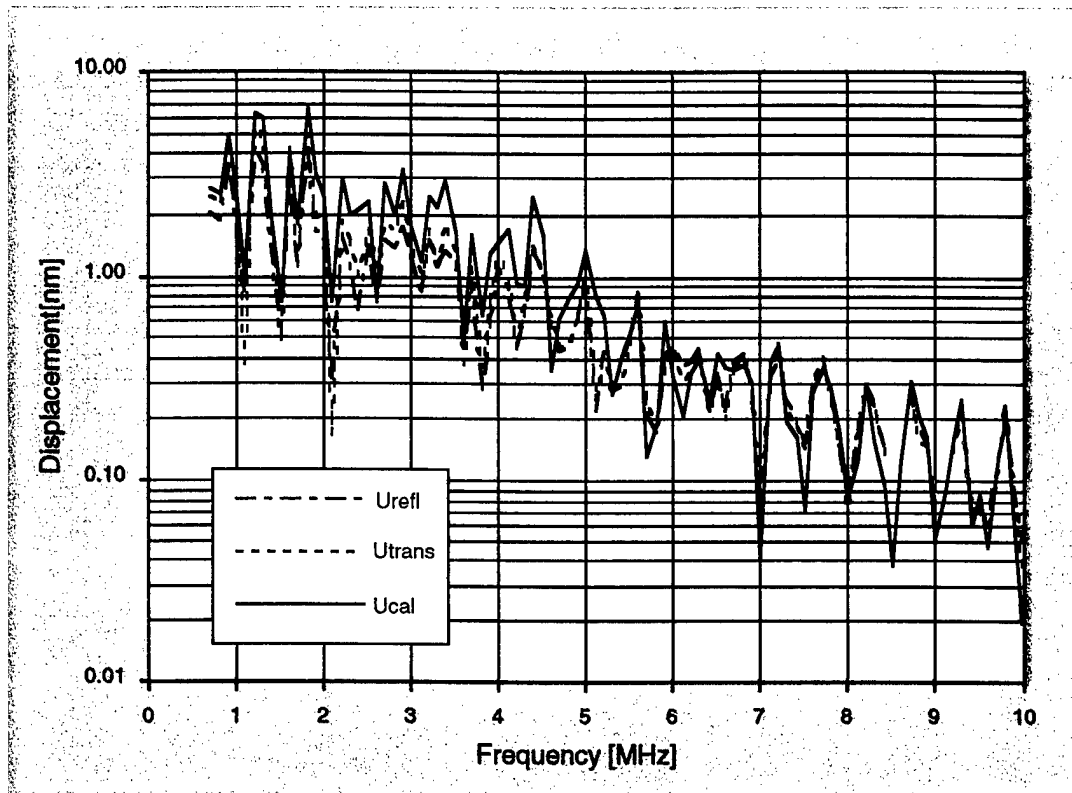
The LACIS prototype system design integrates the laser and optical components discussed in the previous section with a sophisticated real-time data acquisition/control computer (RTDAC), digital signal processors, array processors, reflective memory, and a high-end graphics workstation (SGI). The overall design emphasizes a "loosely-coupled" architectural approach, segmenting the complex design required to create an automated ultrasonic inspection system into manageable software and hardware components. The primary goal was to create a system that could be rapidly modified to support a laboratory environment. The key components, discussed in detail in the subsequent sections, make up a system that utilizes 9 separate CPU's running over 25 processes in 5 different operating system environments.
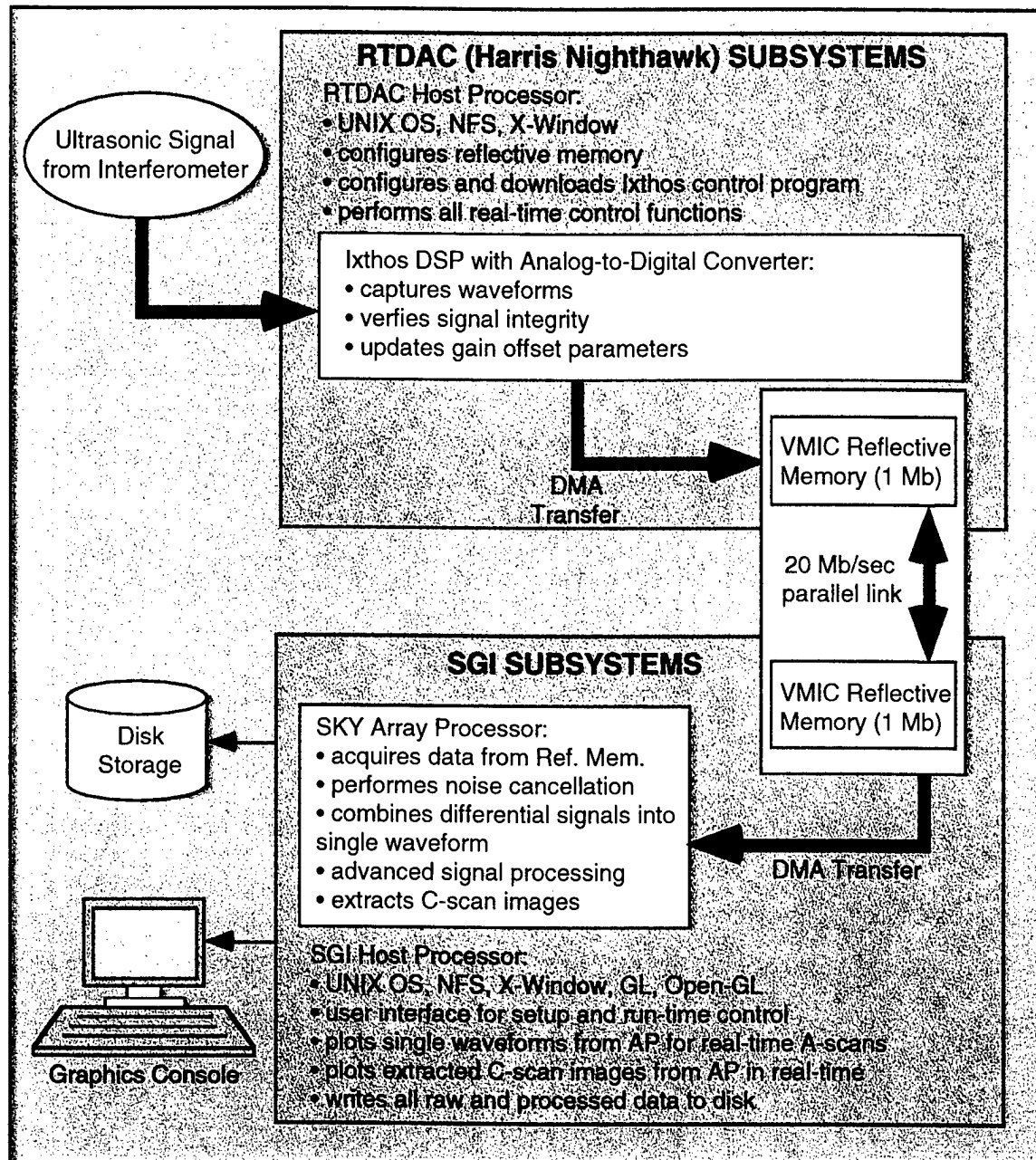
Figure 3-57 This shows a simplified description of the ultrasonic signal dataflow.

3.3.1 Dataflow Overview

Prior to examining the key components of the LACIS prototype's hardware/software design, it is necessary to understand the basic dataflow of the system. Figure 3-57 presents a simplified view of the dataflow for a system that acquires, processes, displays, and stores over 400Kb of data every second (sustained) during the course of a scan that could last for several hours.

Starting with the "ultrasonic signal from interferometer" input box, four raw ultrasonic signals flow into a pair of Ixthos DSP (digital signal processor) boards housed in a Harris Nighthawk chassis. Each board is equipped with multiple 8-bit, 50 MHz, analog to digital converters in addition to an Analog Devices 21020 digital signal processor. The raw signals are converted to digital data, some preliminary processing is done, and the data is transferred via DMA (direct memory addressing) to the VMIC Reflective Memory board. The reflective memory is actually a pair of 1Mb memory-mapped 6U VME boards, one in the Harris Nighthawk and one in a Silicon Graphics Crimson. The boards are connected via a 50 ft. parallel data cable. Control logic on each of the boards causes all "writes" to a particular board to be immediately and transparently transmitted ("reflected") to the other board via a 20 Mb/sec parallel link. Once the waveform data arrives in the SGI systems VMIC reflective memory board, the SKY array processor acquires the data via DMA transfer. After reading the data into its own local memory, the AP uses noise cancellation algorithms to combine the four raw signal into a single waveform. Additional signal processing algorithms are then employed to optimize the signal for data visualization and prepare the signal for defect extraction. Finally, the array processor uses simple "time-of-flight" gating techniques to extract an image from the waveform data. All raw data, processed data, and extracted image data are then placed in an area of AP memory visible to the host SGI. The SGI, which serves as the user's primary interface console, concludes the process by acquiring the data from the AP, continuously drawing quasi-real-time (delayed by approximately 250 milliseconds) A-scans and C-scans to the user console and storing all of the data to disk.

Now that a general overview of the system's dataflow (and thus the basic operation) has been discussed, it is possible to take a closer look at each component of the system and it's function in the LACIS prototype design.

3.3.2 Real-Time Data Acquisition and Control Computer (RTDAC)

The RTDAC is responsible for controlling and coordinating all setup and scan-time activity. It's primary responsibility is to serve as the host and controller of the various real-time components of the LACIS prototype system. It's chassis houses the Ixthos DSP boards, the VMIC reflective memory board, and various VMIC low speed A/D's, D/A's, and digital I/O boards. The low speed A/D's, D/A's, and digital I/O boards are also connected to a custom I/O control/distribution box that houses special circuitry developed by the LACIS team.

The primary tasks of the RTDAC are:

- Fabry-Perot interferometer stabilization and control
- Nd:YAG laser light level control
- Configuration and initialization of the Ixthos DSP boards
- Configuration of VMIC reflective memory board
- Configuration of the initial parameters for the time dependent gain amplifier

3.3.3 Digital Signal Processors with High-Speed A/D

All ultrasonic signals are captured by dual 8-bit, 50 MHz, analog to digital converters mounted on Analog Devices 21020-based Ixthos digital signal processing boards. Each board has two (2) 33-MHz 21020 processors, 128Kb of local memory, 512 Kb of global memory visible to the host Harris Nighthawk, 192Kb of program memory, and supports up to four (4) 8-bit, 50 MHz A/D input channels. The DSPs are capable of performing a 1024 point complex FFT in 580 microseconds. Programming the DSP requires developing a C or Assembly language program on a pc, using a cross compiler to generate 21020 code, and an EPROM source generation utility to create a stack file suitable for "burning" (writing) into a ROM. At this point, either a ROM can be "burned" and installed on the Ixthos board or the file can be transferred to the Harris Nighthawk for downloading into the Ixthos DSP's program memory via the VME bus.

Upon acquiring the signals, the DSP's time stamp the data and perform some limited initial signal processing. They also use information contained in the signals to dynamically adjust time dependent gain amplifier parameters prior to the next trigger. By filling the maximum range of the digi-

tizer without clipping, the optimum signal quality can be achieved. After all preliminary processing has been done, the ultrasonic waveforms are copied into reflective memory via DMA.

3.3.4 Time Dependent Gain Amplifier

A four-channel time dependent gain (TDG) amplifier was designed and constructed to extend the dynamic range of the 8-bit data acquisition system. A photograph of the prototype is shown in Figures 3-58 through 3-60.
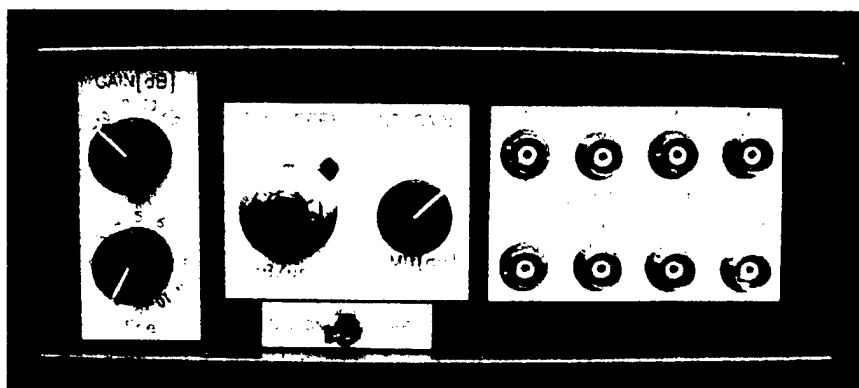

Figure 3-58 The time dependent gain (TDG) amplifier was critical for signal control.

Figure 3-59 The TDG amplifier is controlled by the host computer via analog inputs.
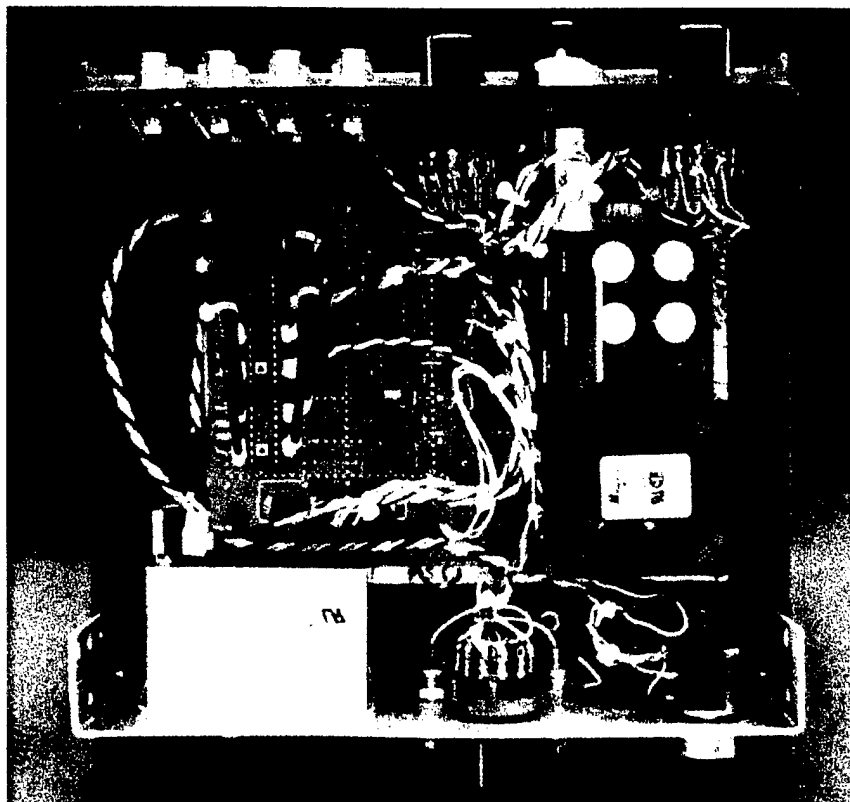
Figure 3-60 The custom TDG amplifier was very reliable although clearly a prototype.

.

The TDG amplifier allows manual or external control of the following parameters:

- Gain offset between -10dB and +30dB

- TDG from 0 to 10dB/μs

- TDG Delay from 1.5 μs to 10 μs

- Gain limit from 0dB to +30dB

An example TDG signal is shown in Figure 3-61. The measured 5MHz signal is only slightly below the 3dB/μs curve on a linear scale indicating the TDG amplifier is calibrated to within a fraction of a dB. Frequency response measurements show a 3dB bandwidth from DC to 40MHz. The noise figure of the amplifier is -134 dBm/√Hz and is gain independent. Note that this noise figure matches the low-noise detector circuit.

Figure 3-61 TDG tests showed minimal gain error.

3.3.5 Low Speed A/D, D/A, and Digital I/O

The low speed activities (anything needing less than a 100KHz sample rate) required to control the LACIS prototype system are performed by a collection of VMIC VME-bus A/D, D/A, and digital I/O boards. These cards, in conjunction with the custom I/O control and distribution box, are used by software running on the host Harris Nighthawk to perform closed-loop stabilization of the Fabry-Perot interferometer, real-time detection laser light-level control, and configuration of the time dependent gain box.

3.3.6 Custom I/O Control and Distribution box

Figure 3-62 shows a schematic diagram of the LACIS prototype inspection system along with the logic in the Control I/O Distribution Box (I/O-Box).
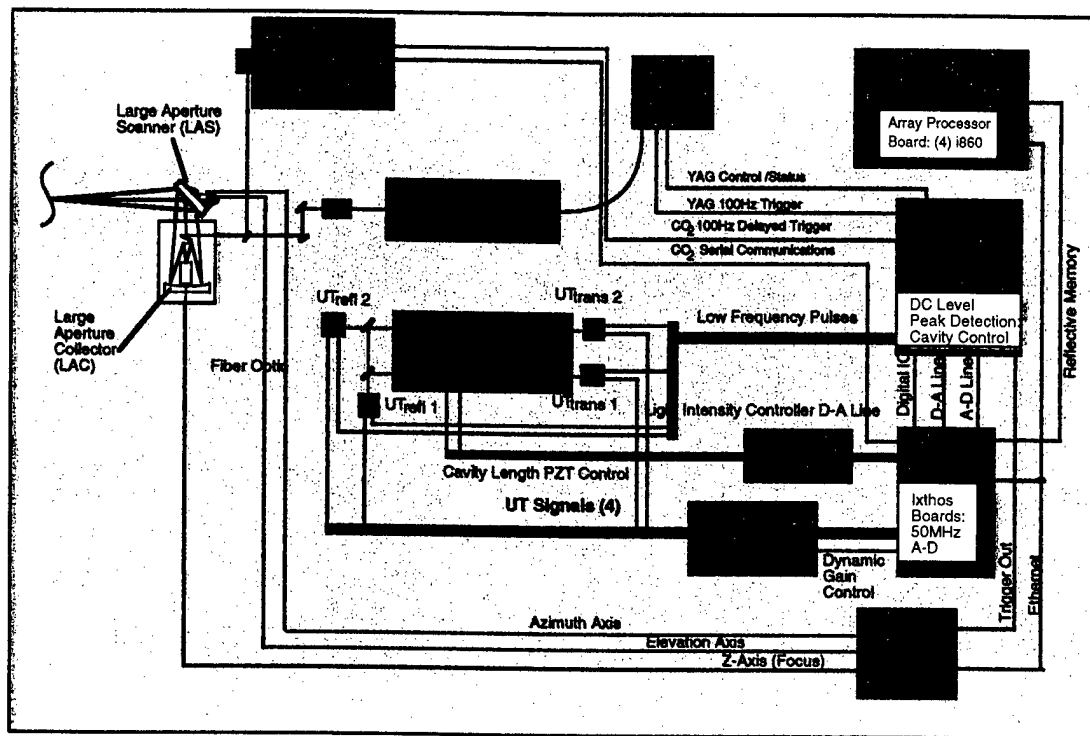
Figure 3-62 System Schematic with Control Lines

This box provides computer interfacing between the various subsystems. For example, the peak detection circuitry converts the Nd:YAG laser pulses into continuous DC voltage levels for use in closed-loop stabilization of the interferometer. The I/O Box also provides time delay circuits to accurately synchronize CO_2 laser triggers with peak pulsed detection laser intensity. There are three computer controlled operation modes for the system based on the state of the I/O Box:

1. Scan Mode
* Both the Nd:YAG and CO_2 lasers are enabled
* All system triggers are received from the LAS during the scan
* Detection laser intensity is computer controlled
* Interferometer is stabilized
* Ultrasonic data is captured for each trigger
* System remains in this mode until LAS issues end-of-scan

2. Setup Mode

- User has full computer control of all subsystems
- Internal triggers are generated at 100 Hz
- CO_2 and Data triggers are divided down to 1 Hz

3. Test Mode

- Used to test data acquisition system at high speed (no laser triggers)

3.3.7 High-Speed Data Communications: Reflective Memory

Reflective memory serves as the primary conduit for data flow between the RTDAC and the SGI graphics workstation. The reflective memory interface consists of two VMIC 5550-210, 1 Mb, 6U-VME boards, connected via a 50' parallel data cable and is shown in Figure 3-63.
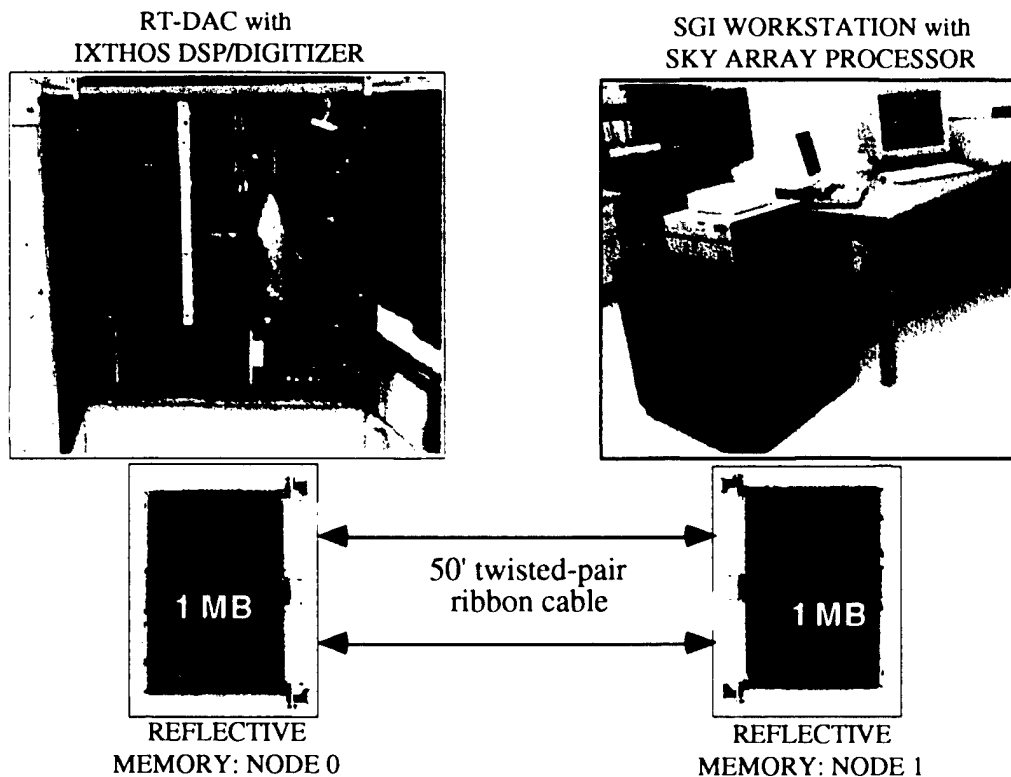

RT-DAC with
IXTHOS DSP/DIGITIZER

SGI WORKSTATION with
SKY ARRAY PROCESSOR

1 MB

50' twisted-pair
ribbon cable

1 MB

REFLECTIVE
MEMORY: NODE 0

REFLECTIVE
MEMORY: NODE 1

Figure 3-63 Reflective memory provides high-speed interface between computers.

Each board is an independent memory-mapped device sitting in A32 VME bus address space. As stated above, control logic on each of the boards causes all "writes" to a particular board to be immediately and transparently transmitted ("reflected") to the other board via a 20 Mb/sec parallel link.

The reflective memory interface between the RTDAC and SGI is established by initializing each board and creating a 1 Mb shared memory region in the each board's VME address space. Any process that maps into either of the shared memory regions now has a direct path for exchanging data with the other system. On the LACIS prototype, a section of the shared memory region is used to hold the waveform data and is treated as a simple circular queue. As the Ixthos board in the RTDAC acquires data, that information is placed in the circular queue and a counter is updated. A process running on the SKY array processor (inside the SGI) is responsible for retrieving the raw waveform data from reflective memory.

3.3.8 Array Processor

The SKY array processor board, a quad i860 processor system with 64Mb of local memory and 320 Mflops of compute power, serves as the primary real-time signal processing hardware for the LACIS prototype system. In our current design, the SGI initializes the AP board, assigns each processor a number 1 through 4, and loads each processor with a copy of the same program. The four processors then operate in a round-robin scheme acquiring and processing data. This begins with the first processor watching the waveform counter in reflective memory, waiting for new data to arrive, then reading it in via DMA. The processor continues acquiring data until a fixed buffer size of data has been received (typically 256Kb to 1Mb), then it passes a signal to the second processor, waking it up to begin it's own data collection. This continues through the third and fourth processor, with the fourth processor passing the "token" back to the first processor. In the meantime, the first processor has completed it's signal processing, data extraction, etc. and copied the raw waveforms, processed waveforms, and other results to an area of memory visible to the host SGI. This parallel algorithm allows much more complex operations to be performed as all data acquisition is overlapped with data processing. Given sufficient memory and more CPUs, this algorithm would scale to allow very complex signal processing and data compression to be per-

formed on the ultrasonic data, all in real-time.

In our current signal processing algorithms, each AP receives four input waveforms per inspection point. These signals represent the transmission and reflection mode signals from each of the two interferometric cavities. Using noise cancellation algorithms, these four signals are combined, creating a single ultrasonic waveform. The software then examines the combined waveform, searching for an ultrasonic front-surface signal. If one is found, the waveform is then considered valid. All valid waveforms are then processed using an analytic transform to enhance data visualization and improve defect detection capability. Although more complex algorithms may be employed later, a simple time-of-flight gate is used real-time to extract a c-scan image of the specimen. A time-of-flight gate starts immediately after the front surface and runs through the back surface. The depth and amplitude of the largest reflection that breaks the gate is extracted. This works very well for finding thickness changes, delaminations, debonds, and inclusions where the foreign material has a significant impedance mismatch with the composite specimen (i.e. teflon in Gr/Ep). The results of this algorithm is part of the information passed on to the host SGI.

3.3.9 Graphical Workstation and Data Visualization

The SGI graphics workstation is a 100 MHz MIPS R4000 processor system equipped with VGX graphics and 128Mb of local memory. It is responsible for performing both scan-time tasks such as real-time a-scan/c-scan display and data storage as well as off-line activities like data analysis, data visualization, reprocessing, and archival.

All software was developed in C using X11R5 and Motif graphics for portability. Routines requiring either real-time or complex graphics were developed using Silicon Graphics mixed model programming (SGI's native IRIS GL programming inside an X/Motif window). This approach will allow for easy migration to OpenGL, the new 3D programming standard based on SGI IRIS GL. OpenGL was not used at the time of development because the SKY Array Processor's device driver did not support the version of IRIX (SGI's Unix OS) required for OpenGL.

3.4 OPERATION AND USER INTERFACE

Figures 3-67 through 3-79 show images of the user interface screen windows. Some of the various options available to the user include part setup parameters, remote cameras interface, scan setup parameters, automated gain control, multiple display and visualization options: e.g. a-scan, b-scan, c-scan.
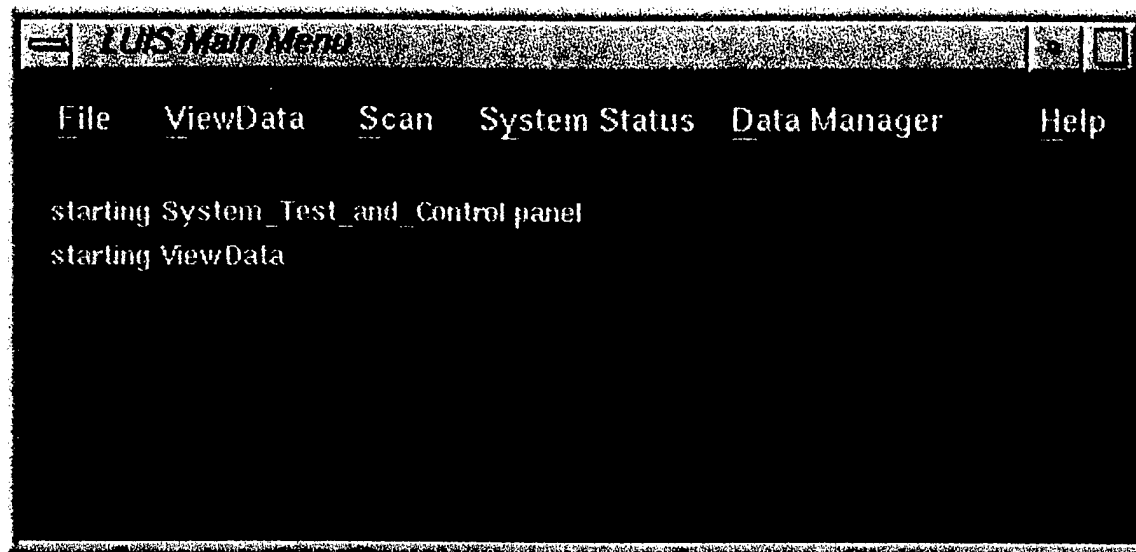

Figure 3-64 Main menu with status window.

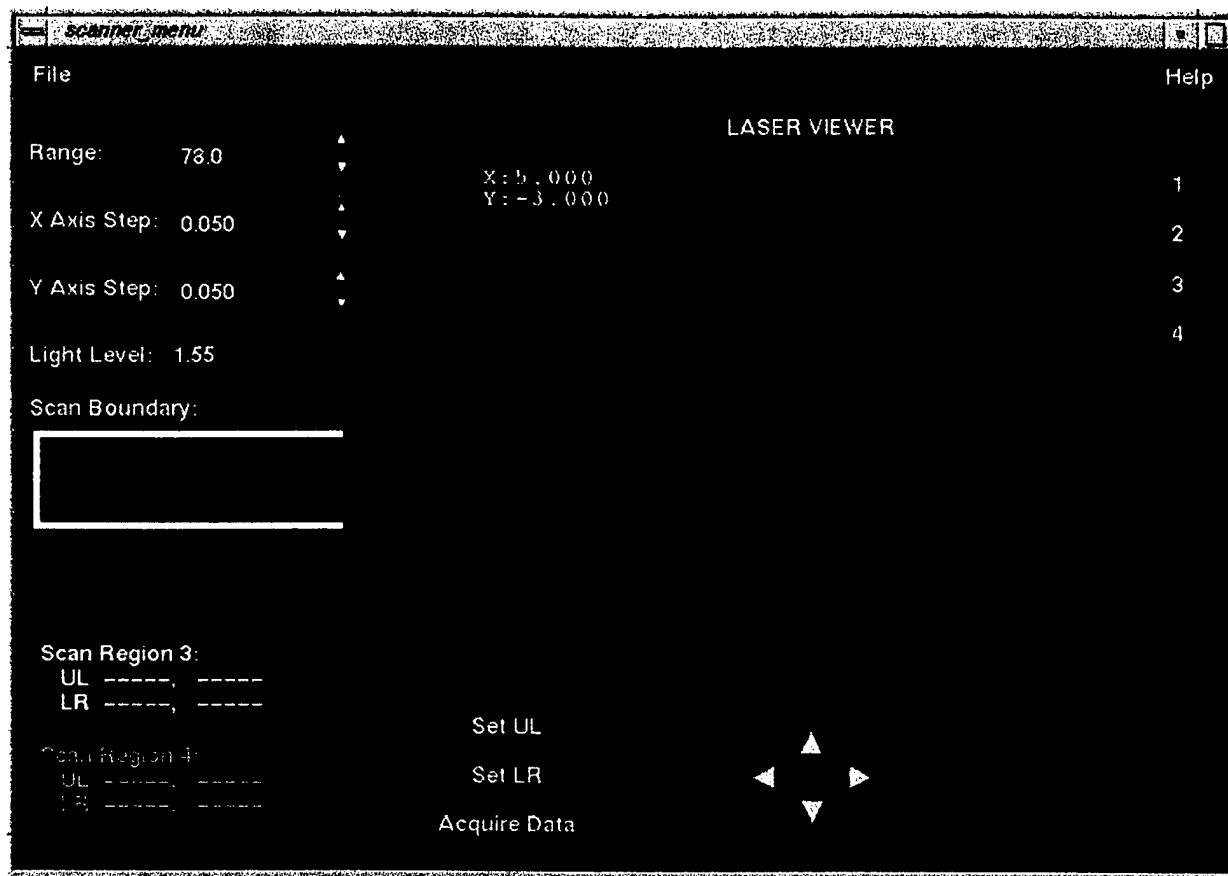**Figure 3-65 Primary scan setup menu with part and operator information.**

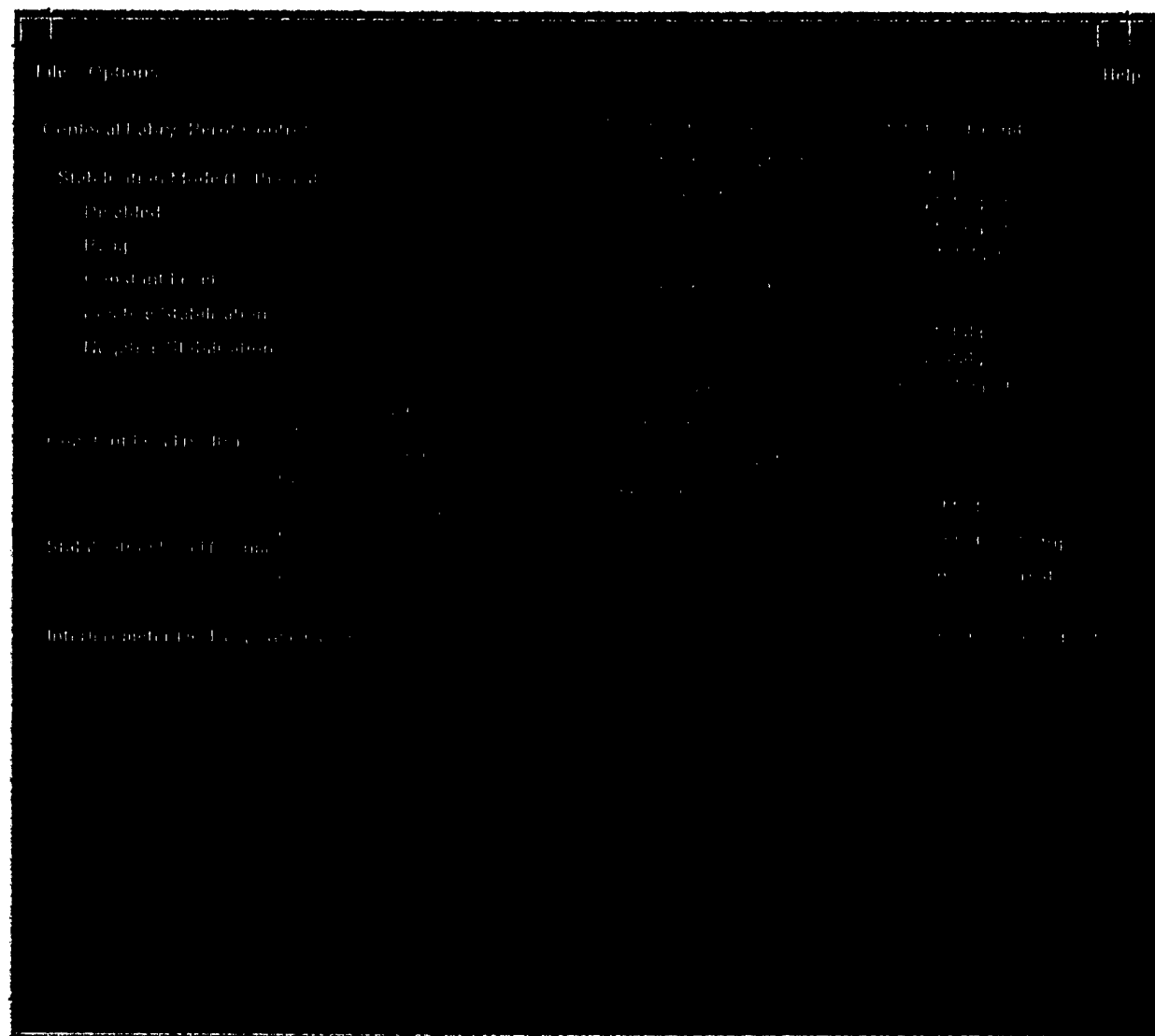**Figure 3-66 Scanner setup menu (live video image will be integrated in future).**

Figure 3-67 Test and control menu shows interferometer status in real-time.
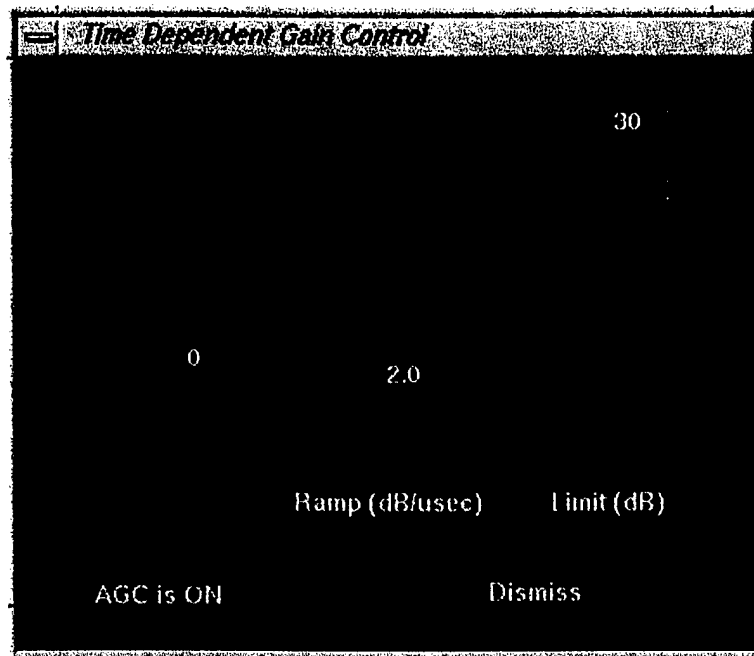
Figure 3-68 Time dependent gain control menu with automatic gain control.

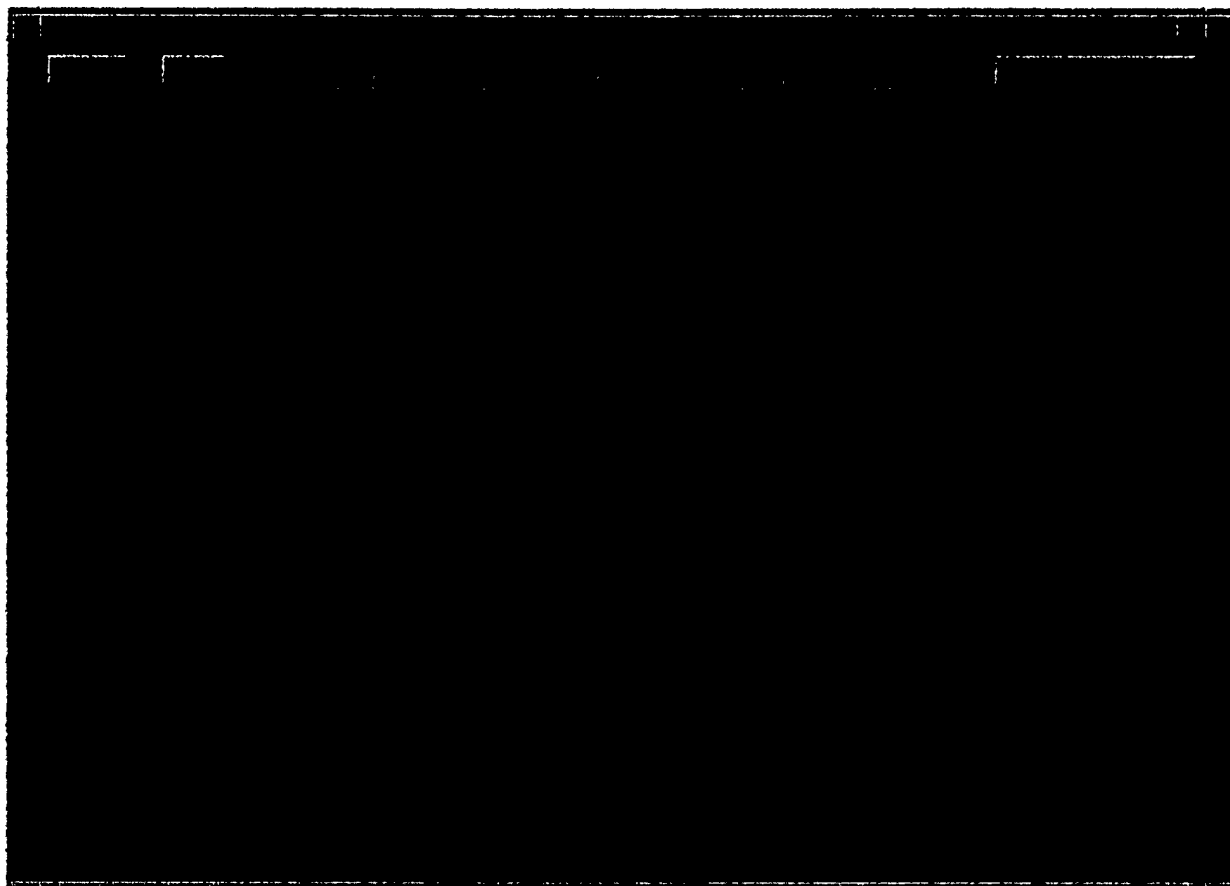Figure 3-69 Real-time a-scan signal viewer shows raw and processed signals.

Figure 3-70 User-friendly graphical file browser.

Project Name   F16

Part Name   1917226

Serial Number   S165420

Scan Number   ba 2

Scan Date Time   03 04 1996 10 09

Inspector   test inspector

Inspector ID   04162

Data Availability

Samples Per Waveform   512

Rows   161

Columns   470

File Version   1 00

Data Type   las rom 4

Sample Rate (GHz)   10

Bits Per Sample   1

Waveform Blocking Factor   0

Waveform Compression Method   None

Laser Rep Rate   400

Range to Target   24 00

X Axis Step Size   0 050

Y Axis Step Size   0 050

Done

Figure 3-71 All parameters describing a scan file are saved for future review.

Figure 3-72 C-Scan viewer can instantly display very large images.
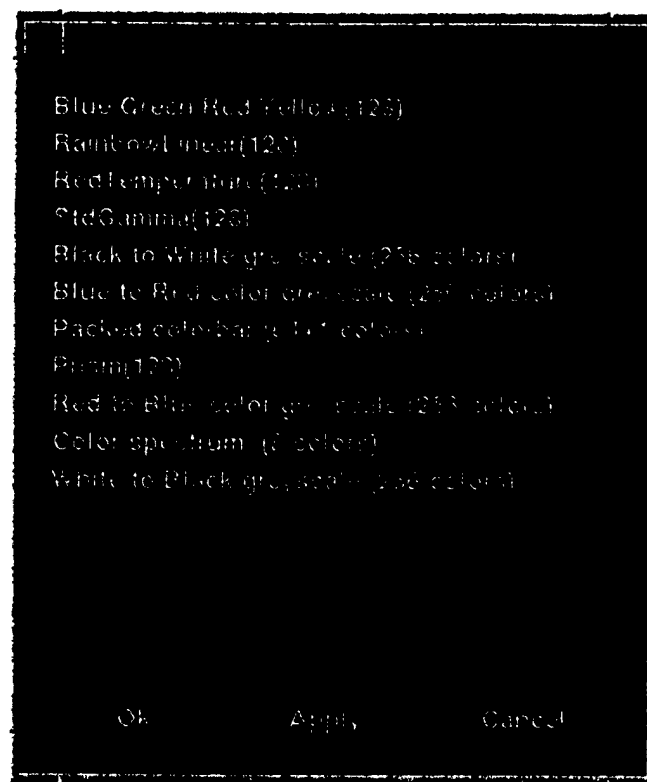
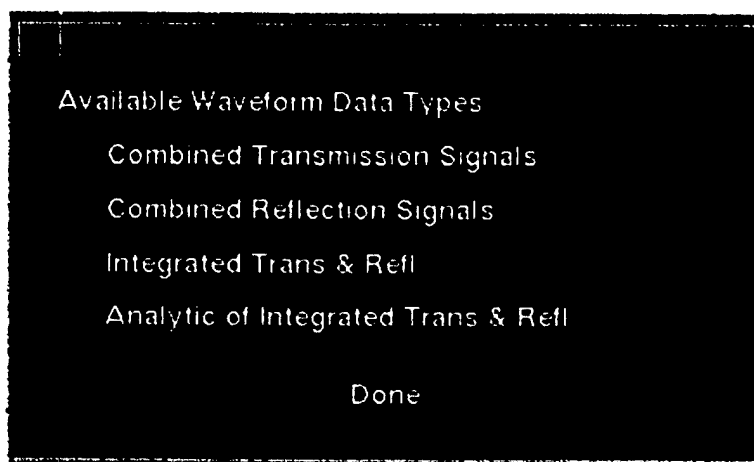**Figure 3-73 An interactive menu allows fast selection of viewdata color schemes.**

Figure 3-74 Different types of data can be selected for A-scan viewing
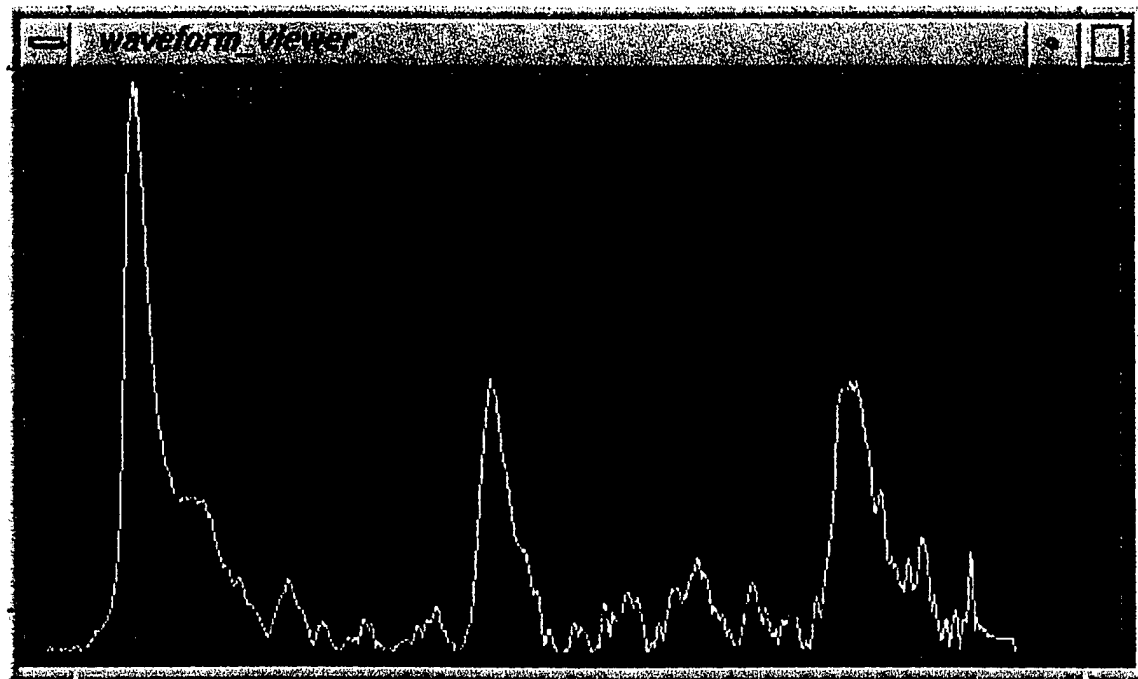
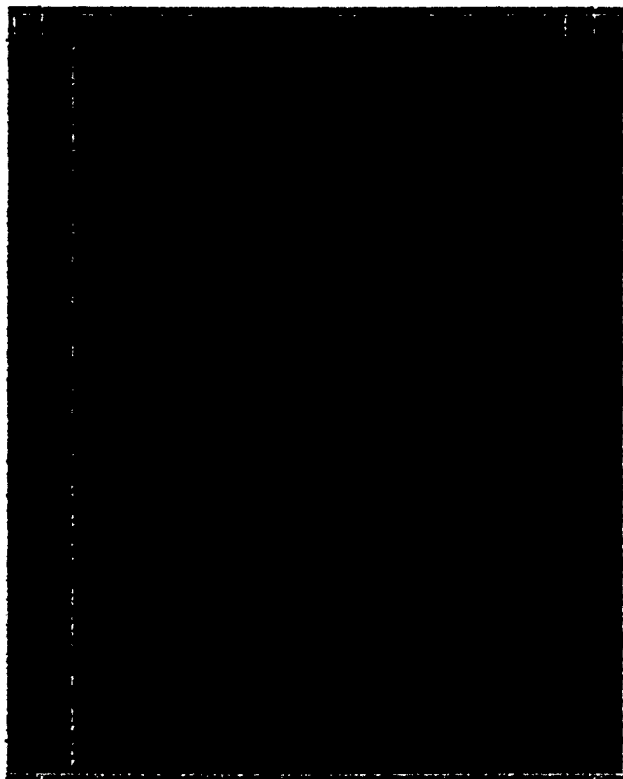**Figure 3-75 A-Scan viewer (showing analytic transformed signal)**

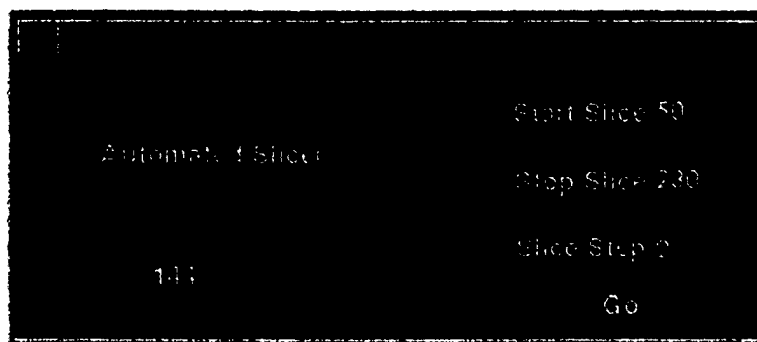Figure 3-76 The B-scan viewer shows thickness variations in a part.

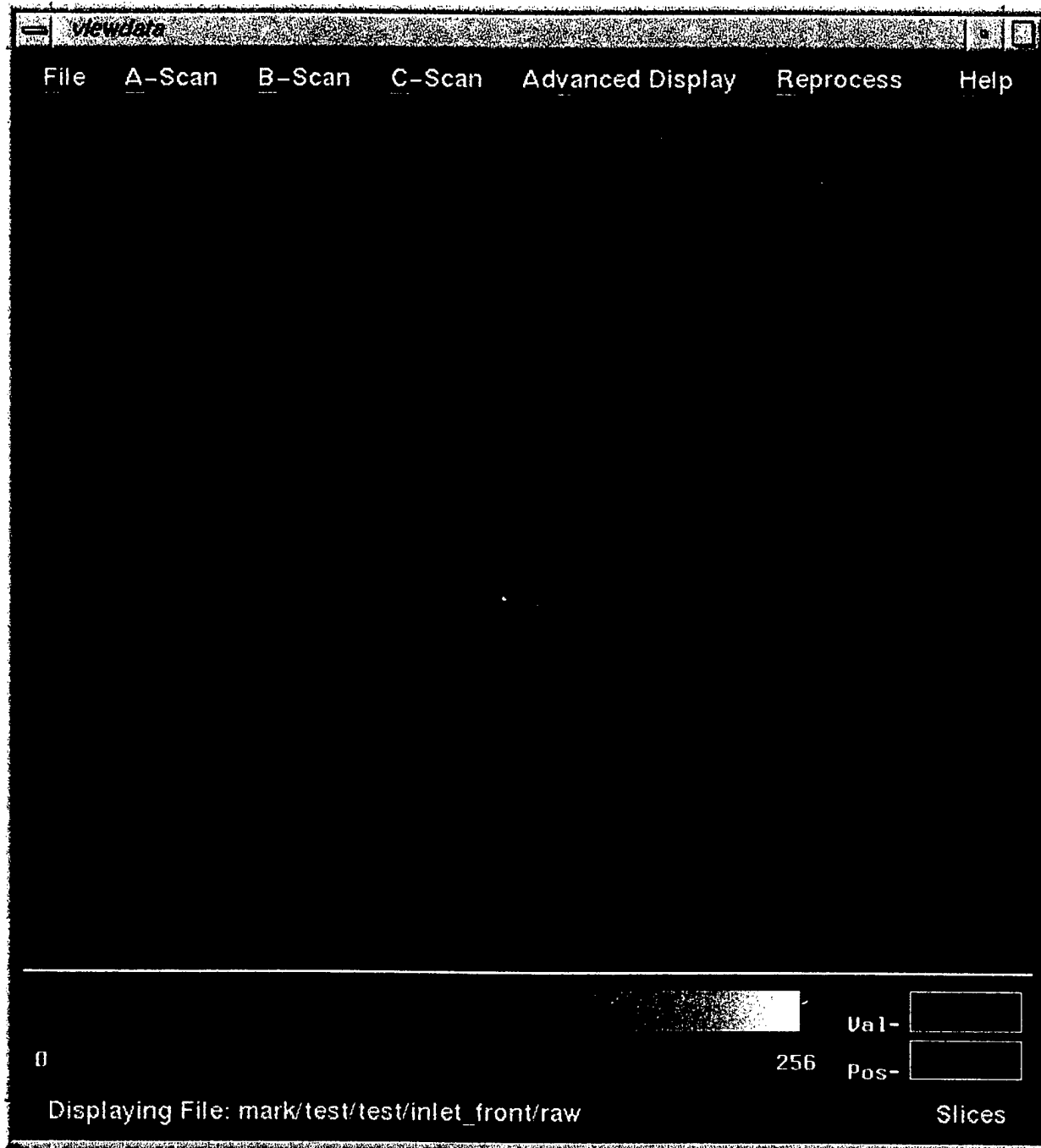Figure 3-77 The dataset slicer provides manual or automatic viewing of slice images

Figure 3-78 Slice images are quickly rendered in the C-scan viewer window.

Figure 3-79 Inspection results are quickly reprocessed with different extraction gates.

4.0 MATERIALS TESTING

4.1 GENERATION EFFICIENCY TESTING

Laser/Material interaction studies were conducted in an effort to determine the effectiveness of the generation of ultrasonic signals in staged (partially cured) laminates. The ability of this technology to detect inclusions and defects in composite laminates is highly dependent on the signal-to-noise ratio and in turn this depends greatly on the surface interaction of both the generation and detection lasers. For staged laminates, both of these can be difficult, but the primary restriction is the ability to effectively generate an ultrasonic signal. It is much more difficult generating an ultrasonic signal in an uncured laminate than in a cured one. In addition, the staged materials attenuate the ultrasonic signal much more than cured materials, especially at higher frequencies (2 -10 MHz).
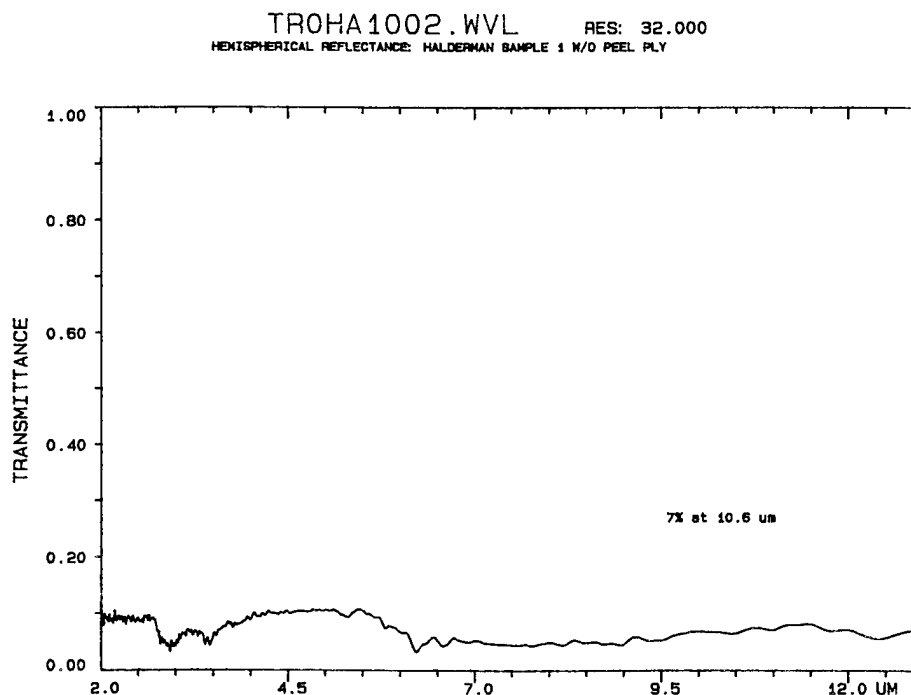
TROHA1002.WVL   RES: 32.000
HEMISPHERICAL REFLECTANCE: HALDERMAN SAMPLE 1 W/O PEEL PLY

Figure 4-1 Integrating sphere reflectance data for bare Gr/Ep (93% absorbed).
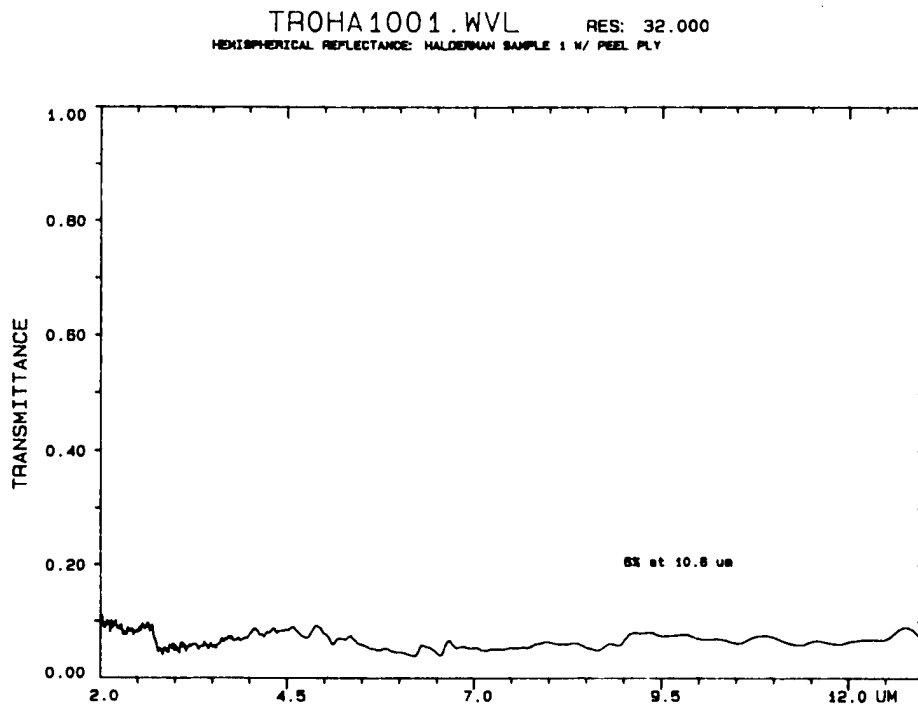
Figure 4-2 The sample with a peel-ply is very similar to the bare material.

Reflectance measurements were taken using a FTIR machine with an integrating sphere. The results for a bare Graphite/Epoxy laminate and a Graphite/Epoxy laminate with a surface peel-ply are shown in Figures 4-1 and 4-2, respectively. Note that the results are similar for both samples showing that approximately 93 to 94 percent of the energy at 10.6 μm is absorbed.

Laser Ultrasonic generation tests were done on two types of staged laminate materials with several different surface conditions. The two laminate materials were IM7 graphite fiber with BASF 5250-4 Bismaleimid (BMI) resin, and T300 graphite fiber with Fiberite 976 epoxy resin. The BMI composite was tested with two surface conditions: bare composite and with a polyester fabric peel-ply. The epoxy composite was tested with four surface conditions: bare composite, polyester peel-ply, 181 weave glass peel-ply, and a 128 weave glass peel-ply. Glass and polyester peel-ply surfaces were also tested on fully cured panels as a baseline. Laser spot size and pulse energies

were identical for all tests. However, a range of spot sizes from 4mm - 9mm in diameter had no effect on the strength or shape of the ultrasonic signals. The pulse energy (with material interaction) determines the magnitude of the ultrasonic signal as long as the detection spot is large enough to integrate over the entire area. Care must be taken not to damage the material when deciding which spot size to use for tests on any given material.

The test setup (Figure 4-3) and procedure were as follows. A conventional 5 MHz ultrasonic transducer with a 1/4" thick acrylic buffer was coupled with water-based couplant to the back side of the laminate to be tested. The 5 MHz transducer was chosen because the interferometer in the Laser Ultrasonic system has peak sensitivity at 5 MHz. For the initial setup on each material the transducer was first connected to a pulser/receiver. The signal from the pulser was used to check for good transducer contact with the material by verifying a proper interface signal. After testing, the data was corrected to account for the buffer impedance mismatch with the tested material.
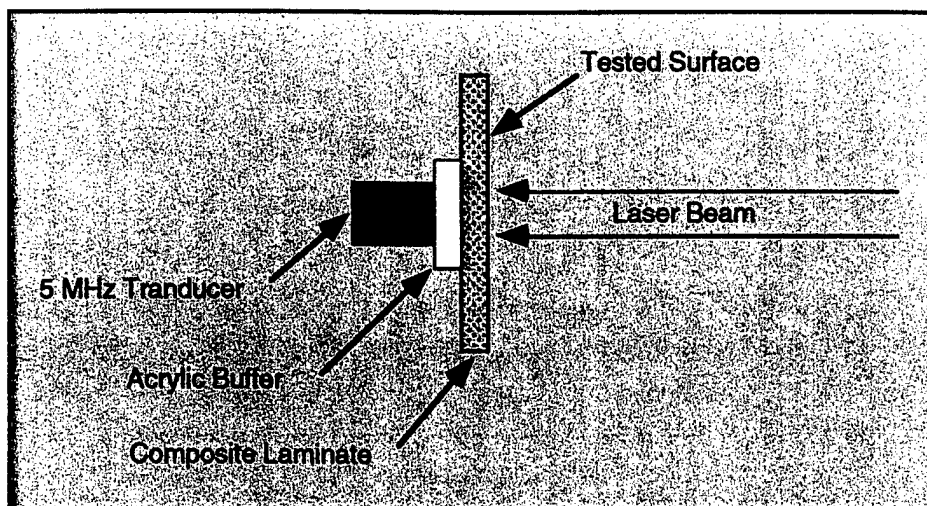

Figure 4-3 Laser generation tests were performed to test different materials.

Table 4-1 lists the materials, stagings, and surface conditions for the laminates tested.

Table 4-1 Laminate Test Conditions

Test	Material	Staging	Surface
1	IM7/5250-4 BMI	200°F/60min	Bare
2	IM7/5250-4 BMI	200°F/60min	Polyester Peel-Ply
3	IM7/5250-4 BMI	260°F/90min	Bare
4	IM7/5250-4 BMI	260°F/90min	Polyester Peel-Ply
5	T300/976 Epoxy	220°F/15min	Bare
6	T300/976 Epoxy	220°F/15min	128 Glass Peel-Ply
7	T300/976 Epoxy	220°F/15min	181 Glass Peel-Ply
8	T300/976 Epoxy	Cured	181 Glass Peel-Ply
9	T300/976 Epoxy	220°F/15min	Polyester Peel-Ply
10	T300/976 Epoxy	Cured	Polyester Peel-Ply

Only the graphs from Tests# 3, 4, and 7 - 10 are presented here for brevity. Other tests showed similar results. Figures 4-4 and 4-5 show the signal strength comparison of the cured laminate vs. the staged laminate for the polyester and glass peel-plies, respectively (Tests# 7 - 10). Notice the distortion and increased level of low frequency noise in the staged material as well as the much reduced signal strength and the broadened signal. The difference in signal strength is roughly an order of magnitude in both cases. These general features are typical of all of the staged materials tested. Also compare the strength of the glass and polyester signals in both the staged and cured condition. Glass peel-plies are typically much harder for the generation laser to couple into the material and produce an ultrasonic signal. The difference in signal strength in these cases is approximately a factor of 5. Differences of these magnitudes can produce serious difficulty in the ability to generate and detect ultrasonic signals in staged materials. A difference of approximately a factor of 50 exists between a cured panel with polyester peel-ply and a staged panel with glass peel-ply.
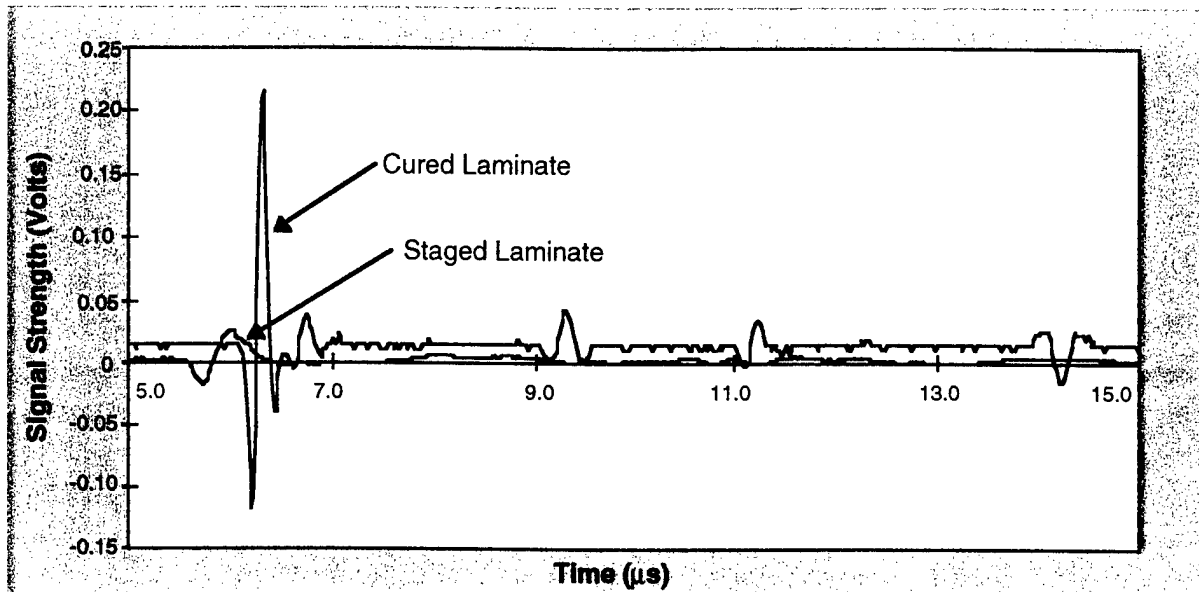
Figure 4-4 Cured and staged epoxy laminate comparison with polyester peel-ply.
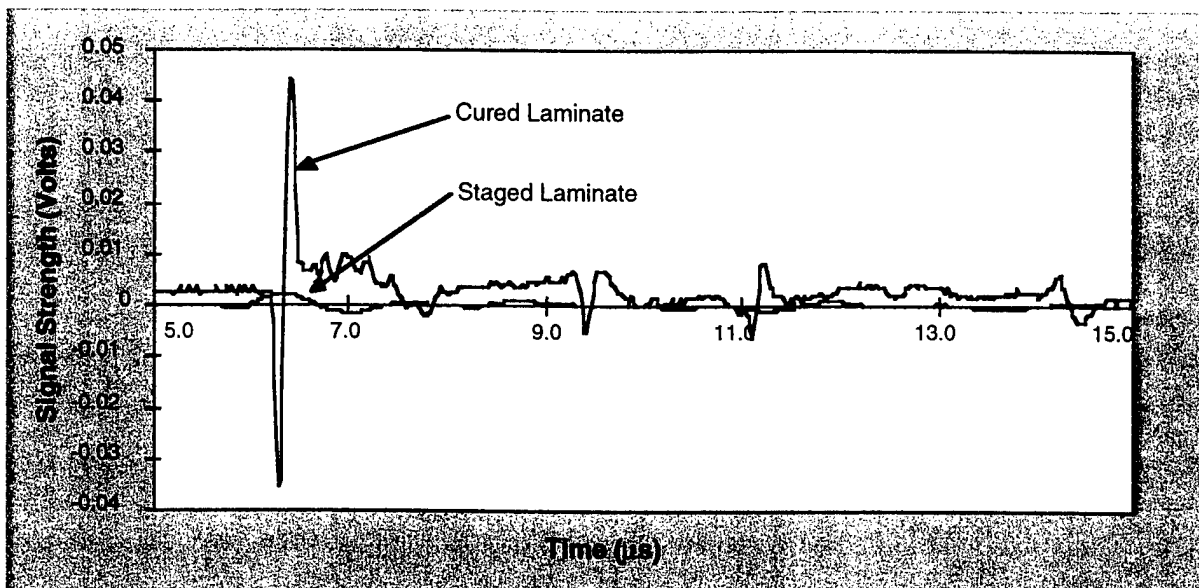

Figure 4-5 Cured and staged epoxy laminate comparison with 181 glass peel-ply.

Figure 4-6 shows the comparison of the generated signals in the BMI for bare composite and polyester peel-ply (Test# 3 and 4, respectively). These panels were in a much higher cured stage than the previous tests and therefore show larger signal strengths. Note again the difference in signal between the bare and peel-ply surfaces. Test# 4 with the polyester peel-ply is very close to being within the ability of the Laser Ultrasonic system to effectively test for inclusions. One more major system improvement is planned in the next two months which should increase system sensitivity by a factor of two. This may bring Test# 4 as well as some of the others into testing range.
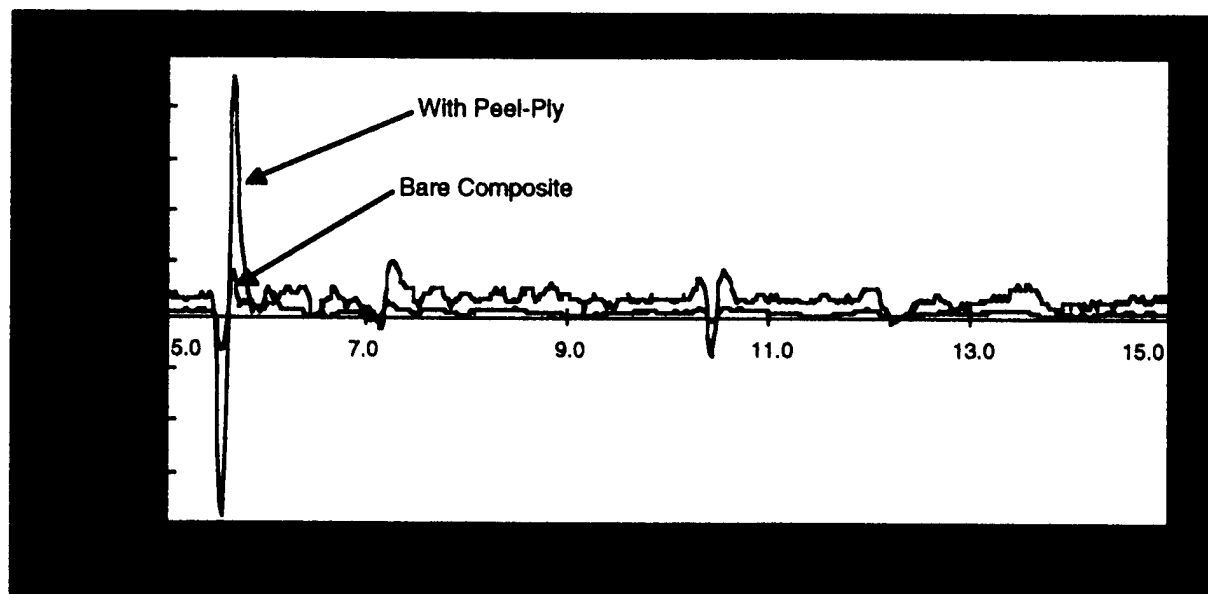

Figure 4-6 Comparison of bare composite and polyester peel-ply for staged BMI.

The general conclusion is that it is very difficult for the Laser Ultrasonics system to test staged materials effectively. The longer stagings increase the ability of detection and provide larger signal strengths and clearer signals. In addition, the surface condition (peel-ply, etc.) is extremely important in determining the signal condition. Glass peel-plies and bare composite are generally much more difficult than the finer weave polyester fabric. Near-term improvements in the system may provide enough sensitivity to effectively test some of the longer staged materials either bare

or with polyester peel-ply. This work was also funded in part under ARPA's Affordable Polymer Composite Program: Cure Form Processing, Contract F33615-95-C-5021.

4.2 F-16 TESTS

4.2.1 Inspection Reference Test Part: *Simulated Delaminations*

A 52-ply graphite/epoxy laminate, representative of F-16 structures, was tested and is shown in Figure 4-7 with flat-bottom holes simulating internal delaminations that might occur in-service. The holes range in size from 0.125", 0.25", 0.50" to 0.75" at depths representative of near-surface and far-surface delaminations. A polyester peel-ply is attached to the front surface. Actual in-service applications would typically have painted surfaces that generally enhance results due to improved laser generation of ultrasound.
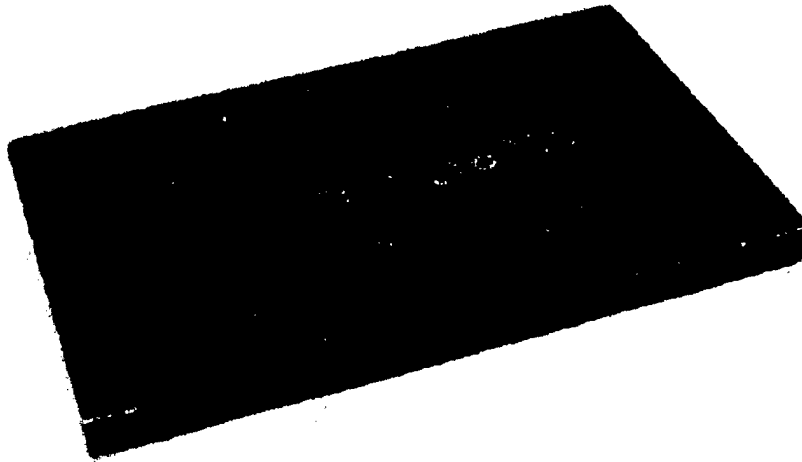

Figure 4-7 Photograph of test part with simulated delaminations (flat bottom holes).

This part was scanned at a resolution of 0.05" and results from the inspection are shown in Figure 4-8. The A, B, and C-scan images show sufficient resolution for the detection of delamination defects in this material.
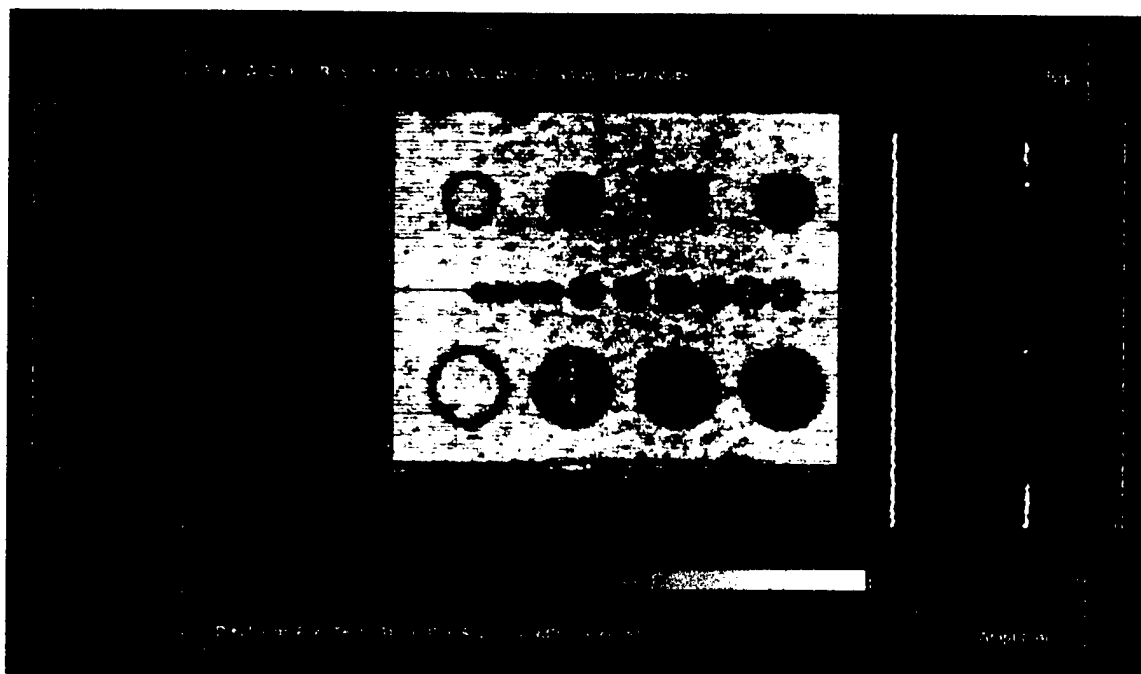
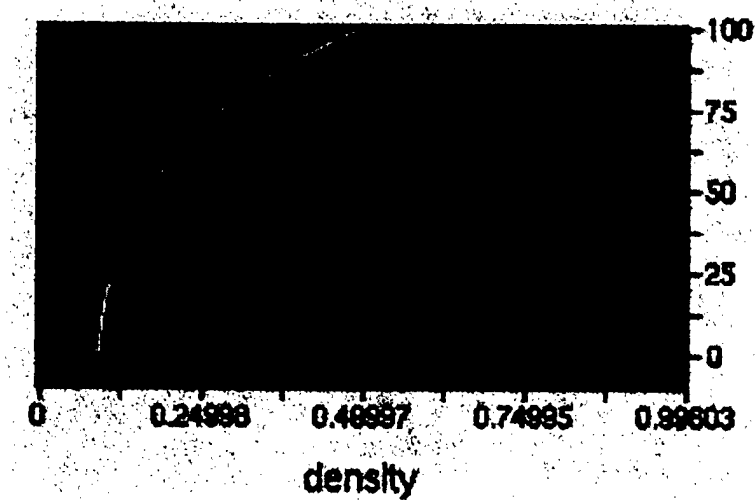**Figure 4-8 Visualization analysis of the flat bottom hole test part.**

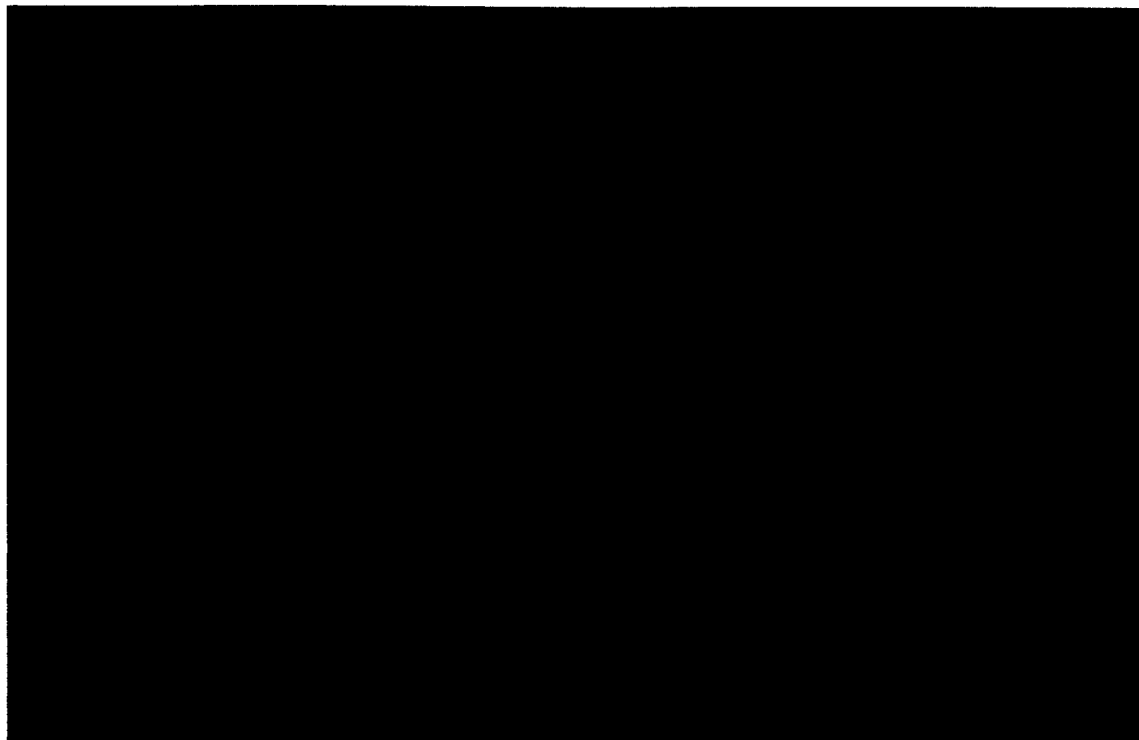**Figure 4-9 Voxel opacity function encodes data as a function of signal intensity.**

114

Figure 4-10 Volume rendered image shows defects <u>without</u> user defined gates.
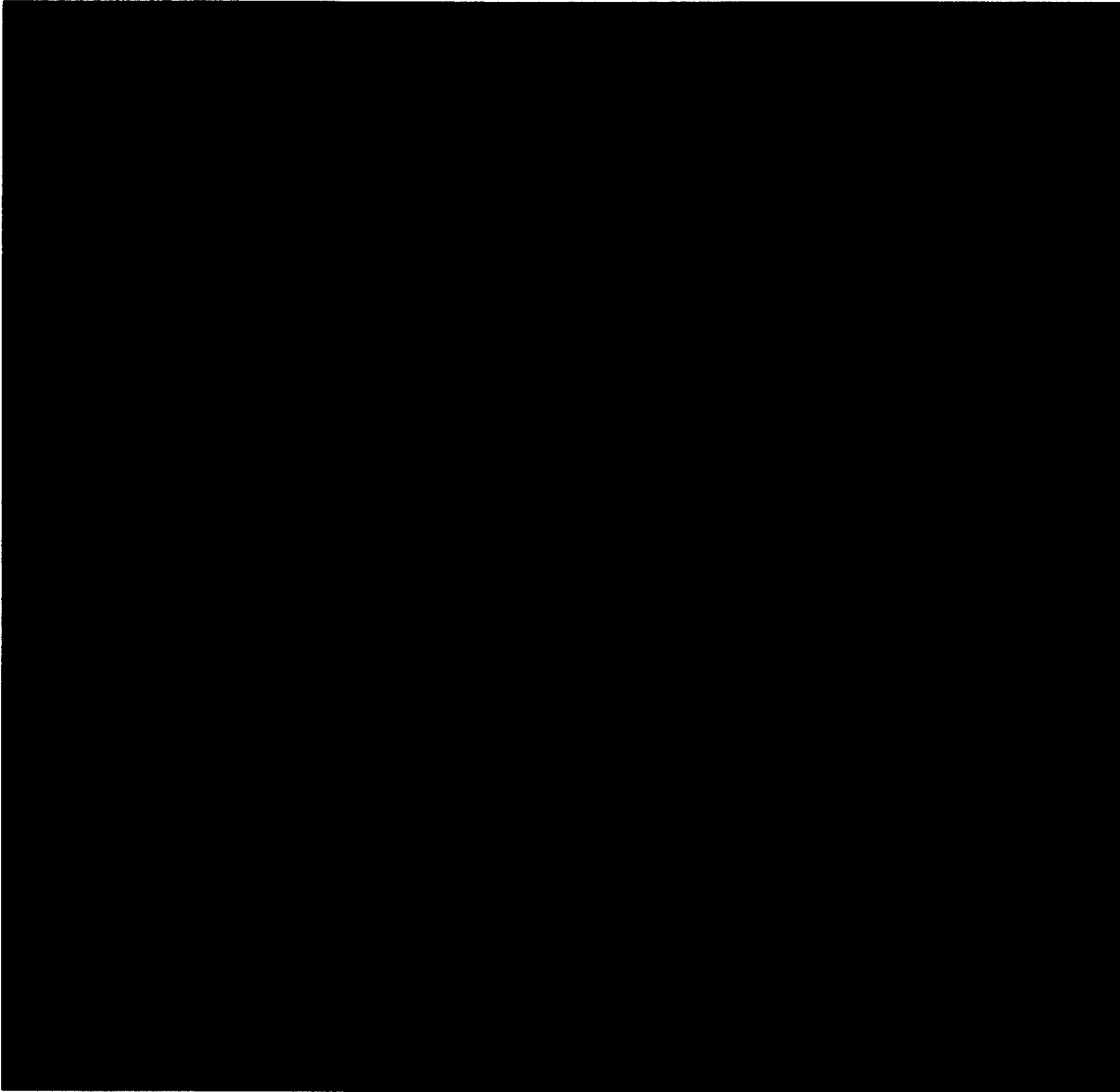
Figure 4-11 Volume rendered image shows defects in 3D perspective.

4.2.2 Horizontal Stabilizer Skin: *Real Delaminations*
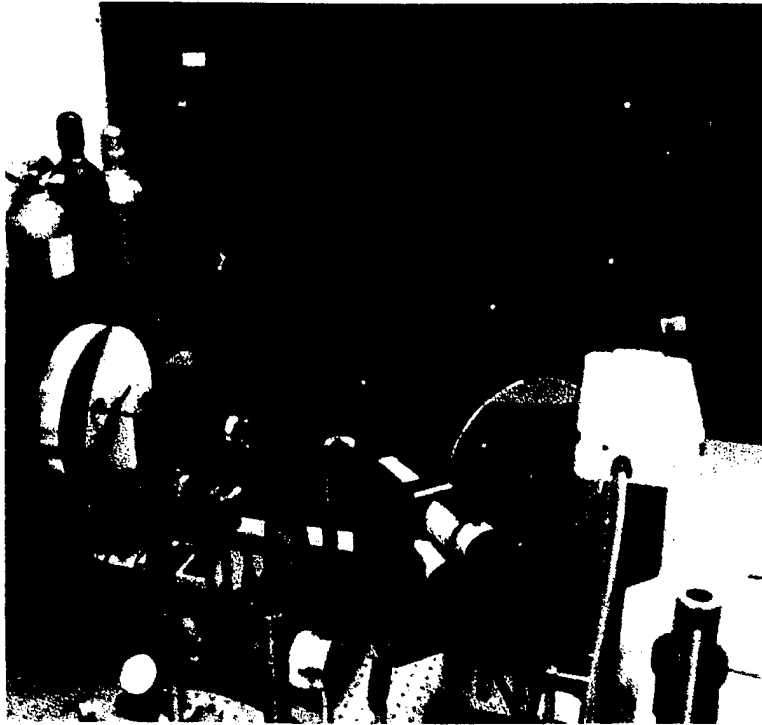
Figure 4-12 Photograph of system testing a large F-16 horizontal stabilizer skin.

Material Type: Fiberite HYE1076 Graphite/Epoxy laminate.

Surface Condition: Polyester peel-ply (Airtech release ply G).

Comments: Delamination around fastener holes.

Figure 4-13 F-16 materials show good signal-to-noise ratio of system.
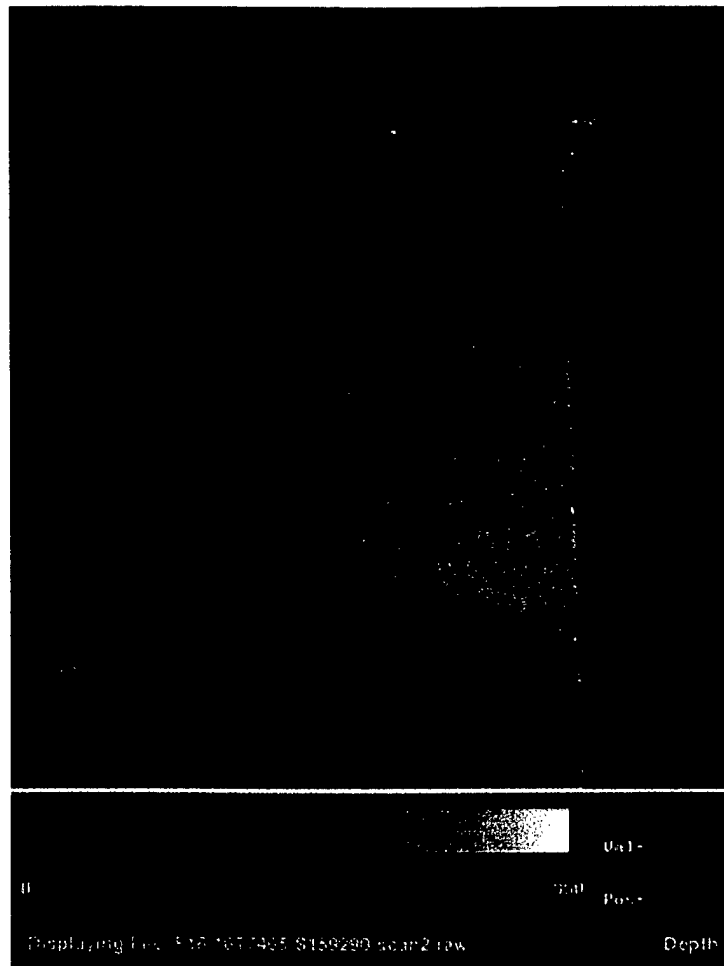
Figure 4-14 C-scan depth image results show excellent defect detection resolution.

Figure 4-15 The part thickness profile and delaminations are visible in this B-scan.

4.2.3 Vertical Stabilizer Skin: *Porosity*

Figure 4-16 Laser UT can rapidly detect multi-level porosity.

Material Type: Fiberite HYE1076 Graphite/Epoxy laminate.

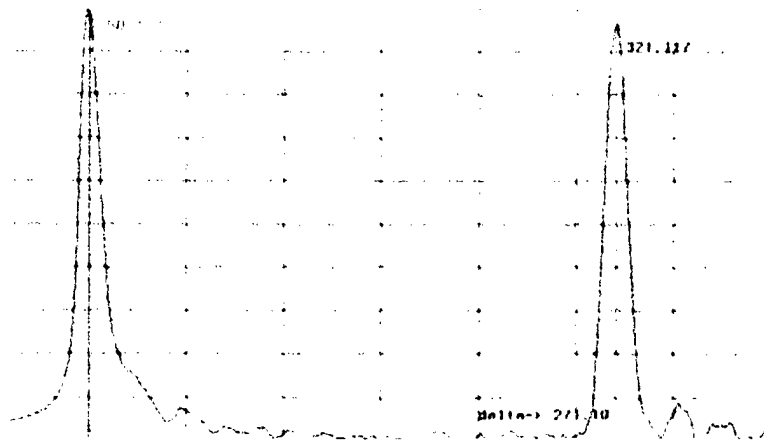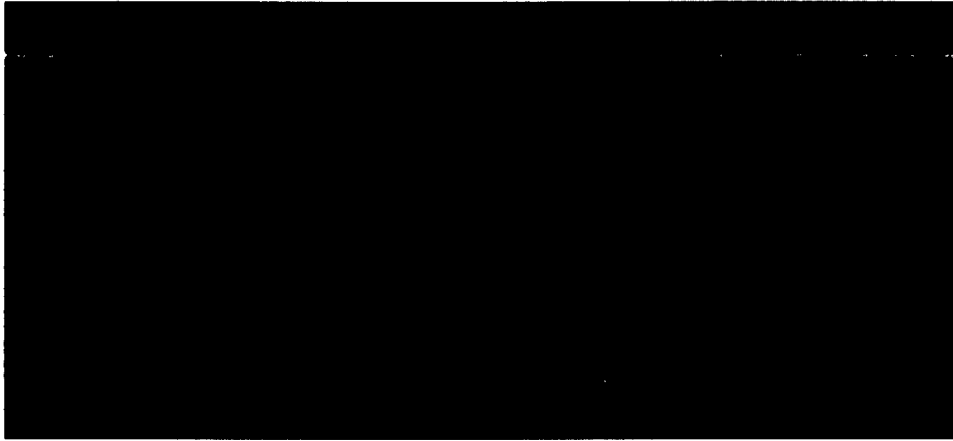Surface Condition: Polyester peel-ply (Airtech release ply G).

Comments: Porosity in surface layers.

4.3 F-22 TESTS

The F-22 fighter aircraft has many large composite structures with highly complex geometries integrated into the design. Large fuselage skins, inlet duct skins, and weapons bay doors are only a few. Materials for these structures range from IM7/977-3 Graphite/Epoxy to IM7/5250-4 BMI to Radel thermoplastics. Both tape and fabric materials are used in the layup of many of these structures. Fig.4-17 shows a front view of a large F-22 Inlet Duct Skin made of IM7/5250-4 BMI. Figure 4-18 shows views from either side of the inlet clearly showing the highly contoured surface. Current conventional squirter technology requires approximately 24 man-hours for setup and testing of this part. Testing of first articles for complex parts often takes as long as two weeks to setup and test. This part was tested in 2 hours, including setup and data analysis, using the LACIS prototype.

4.3.1 Inlet Duct Section: *Complex Contour*

Figure 4-19 shows an amplitude c-scan plot of the Inlet Duct Skin shown in Figures 4-17 and 4-18. This part was rejected in production for wrinkles that occur near the ply transitions of the windowed areas. These wrinkles cannot be seen well in the photograph but are clearly evident in the amplitude c-scan and show up as dark lines running roughly vertically in the middle of the windows. Figure 4-20 shows a close-up view of wrinkles in the ply transition areas. Figure 4-21 shows a depth c-scan image of this same part. Note that conventional systems will typically drop data in the ply transition areas which then must be hand-scanned, whereas the Laser Ultrasonic system does not. A B-scan view (perpendicular cut through the laminate) is shown in Figure 4-22
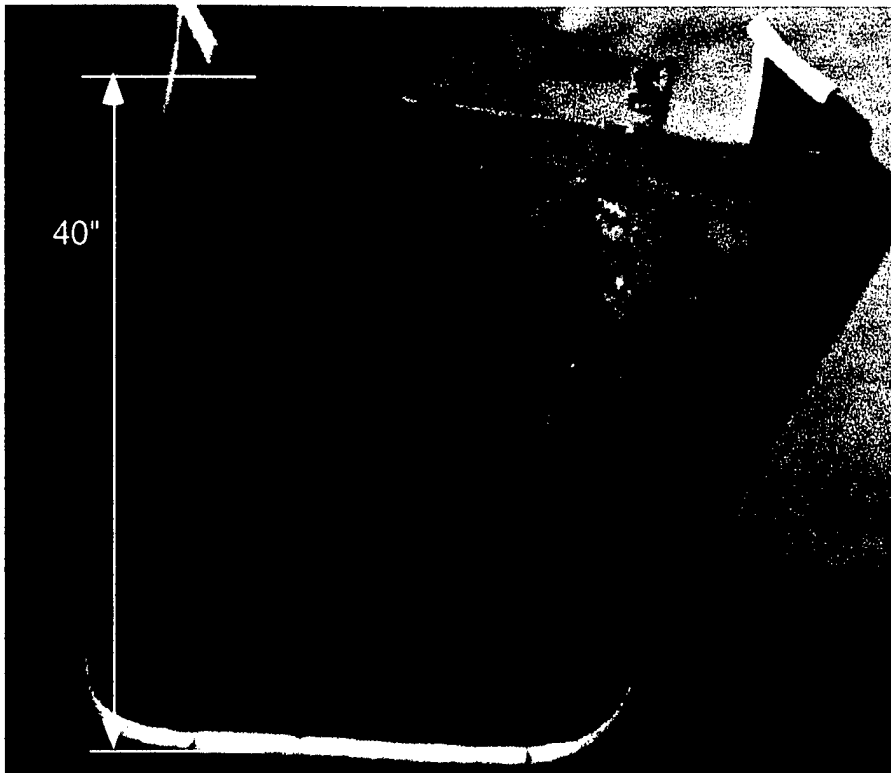
Figure 4-17 This "risk-reduction" F-22 inlet section was rejected for surface wrinkles.
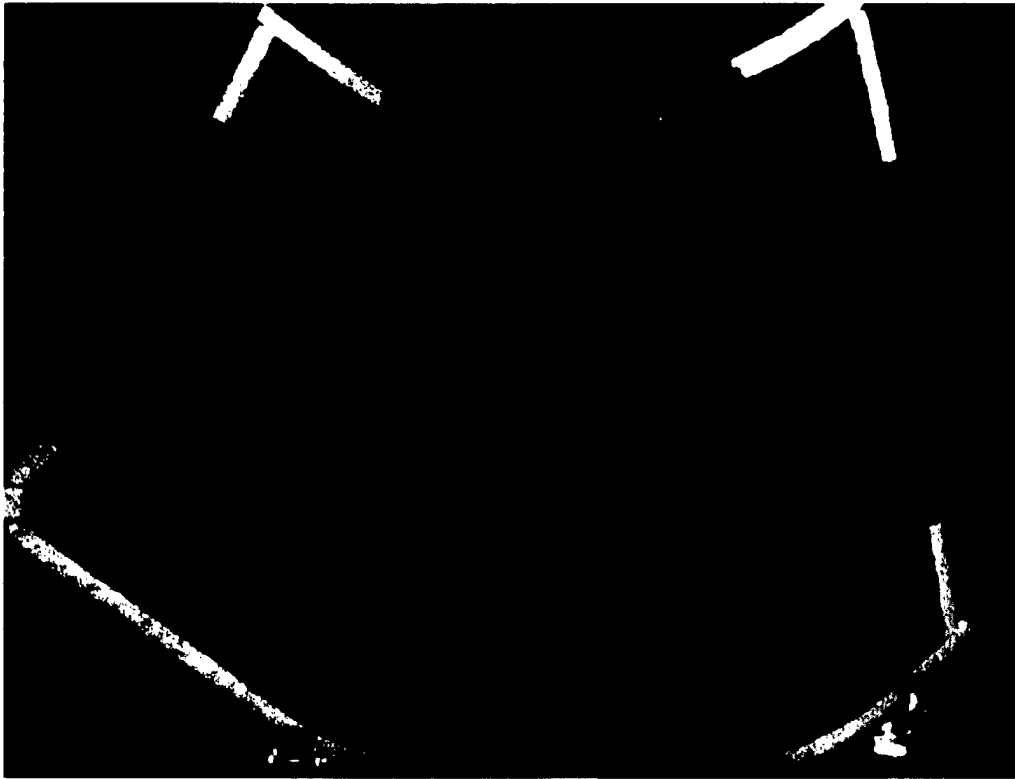
Figure 4-18 Rotation of the part allows full coverage of the contoured surface.
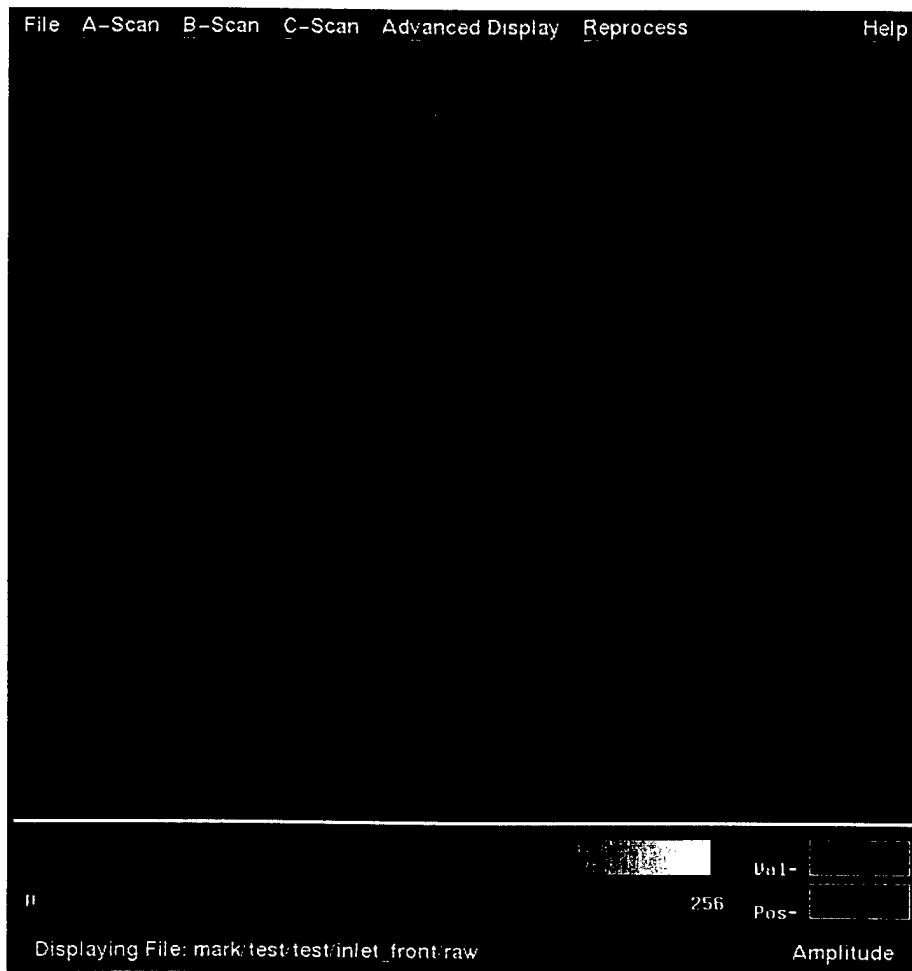
Figure 4-19 C-Scan image shows high resolution (paint markings are visible).

Figure 4-20 Surface wrinkles are visible in this zoom image.
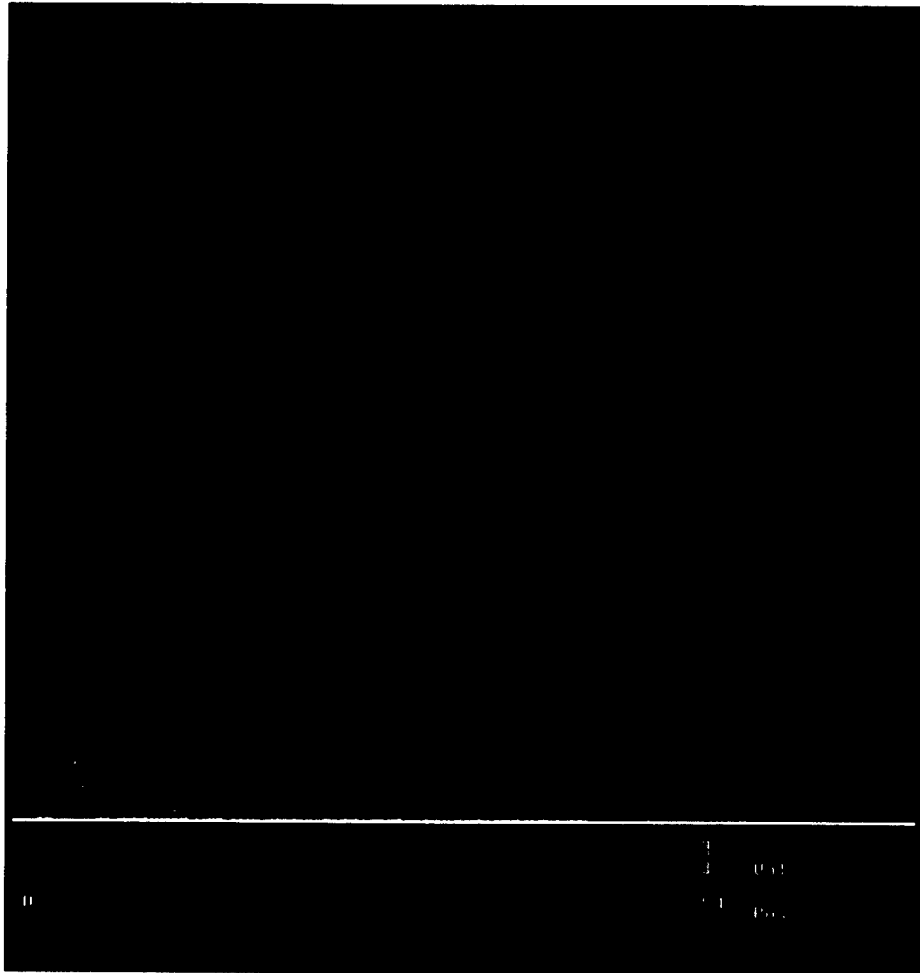
Figure 4-21 Uniform results were obtained over the highly contoured surface.
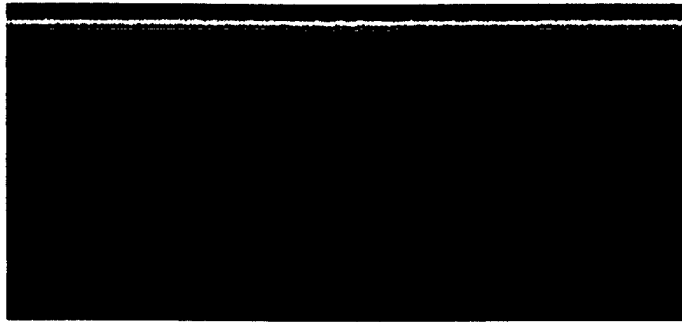
Figure 4-22 This B-scan slice shows the part thickness profile.

Figure 4-23 The inlet was rotated and scanned to inspect the sides.
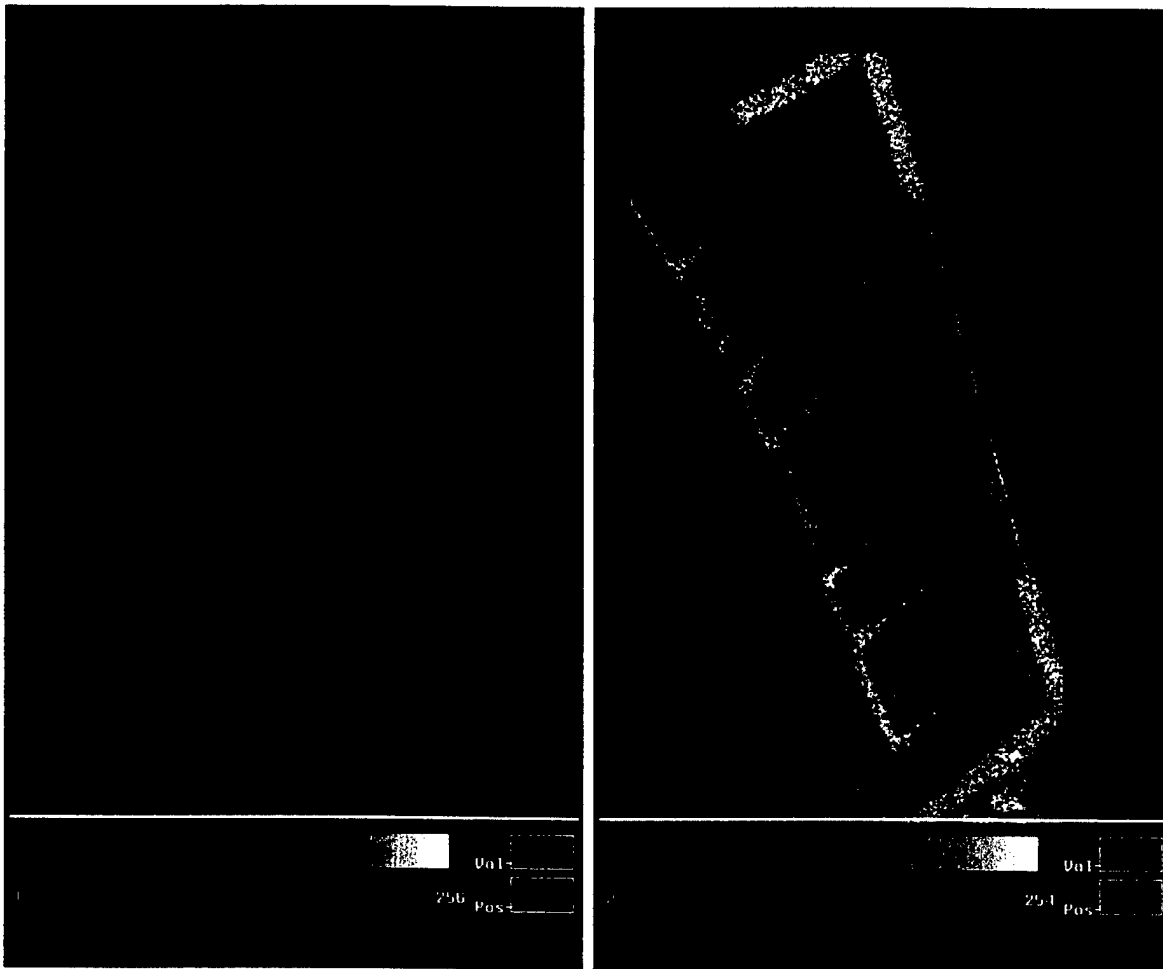
Figure 4-24 Laser UT reduced the inspection time from 24 hours to less than 2 hours.

4.3.2 Duct Splice: *Complex Contour with Real Inclusion*

Figure 4-25 shows an inlet duct splice composite laminate that was rejected in production due to an inclusion that can be seen in the c-scans. Figures 4-26 and 4-27 show c-scans for comparison between the LK production squirter system and the LACIS prototype. The laminate material is IM7/977-3 Graphite/Epoxy. Again, note the loss of data in the ply transition areas around the window in the LK c-scan. The LACIS prototype maintains data in all these areas as well having better registration of the scan which produces much sharper lines.
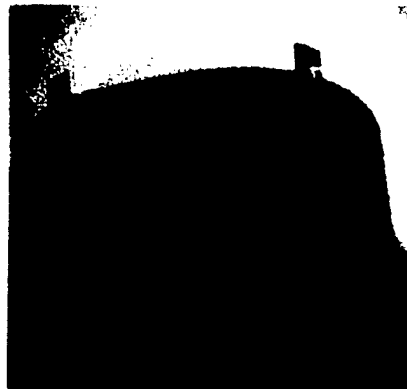
Figure 4-25 Photograph of F22 Duct Splice Component
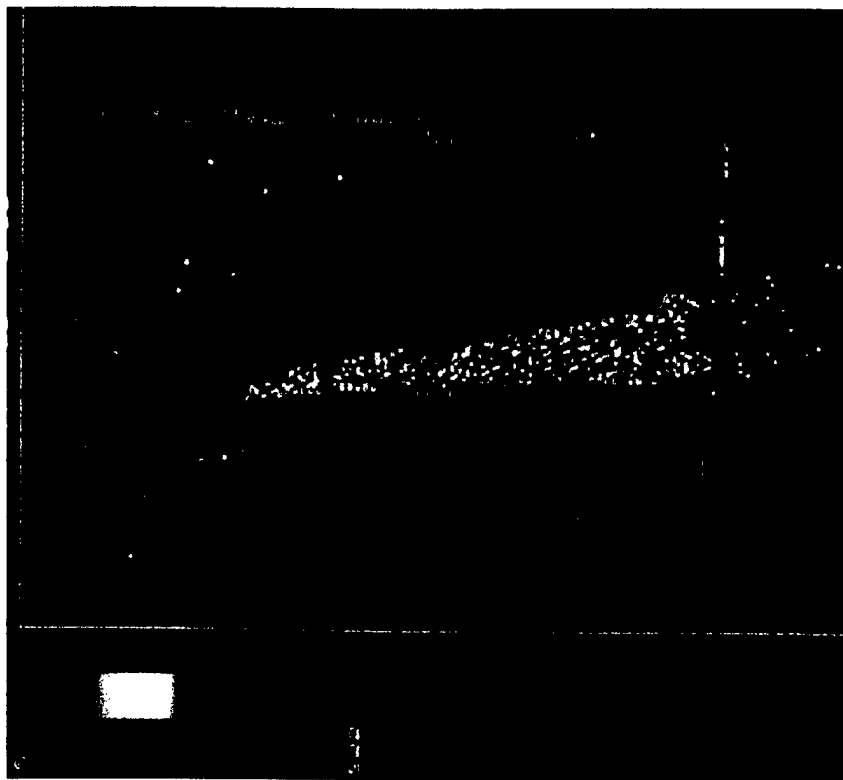
Figure 4-26 Inspection by a conventional system is slow and shows poor data quality.
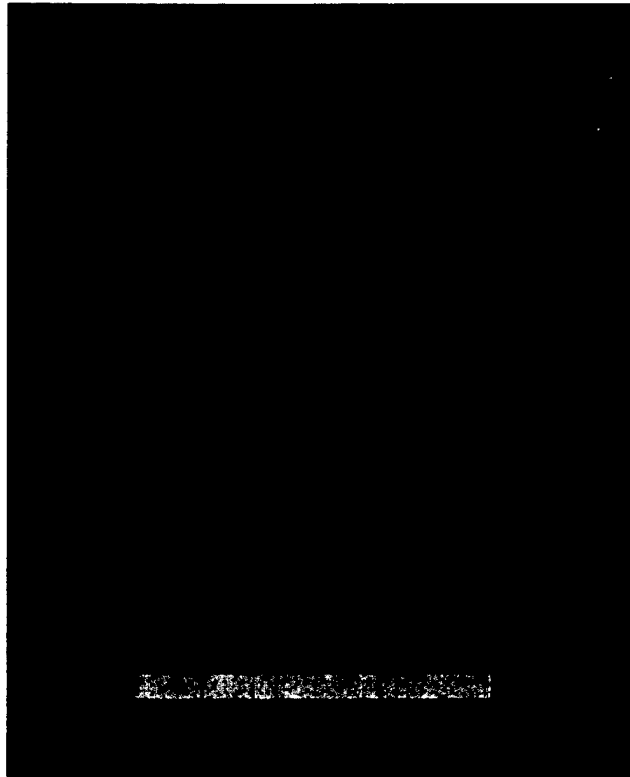
Figure 4-27 Laser UT detected the inclusion with improved speed and resolution.
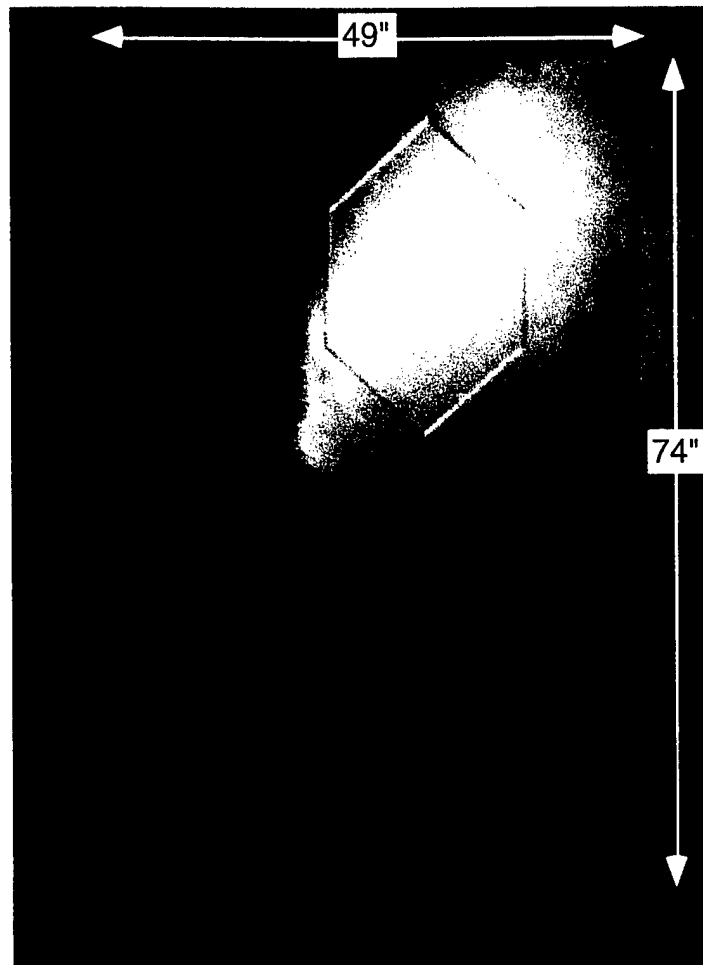
Figure 4-28 The F-22 "risk-reduction" mid fuselage skin pushed the size limits.

4.3.3 Mid Fuselage Skin: *Very Large, Complex, with Implanted Inclusions*

Another example of a large composite structure on the F-22 is the mid-fuselage skin shown in Fig.4-28 together with a depth c-scan plot extracted from data taken with the LACIS prototype. This part is a tape/fabric hybrid of IM7/5250-4 BMI with medium contours and many windowed areas and ply transitions. The c-scan image was produced with a single laser ultrasonic scan. This part was scanned from the side not seen in the photograph and therefore the c-scan image (Fig.4-29) is an inverted view. Note the slight loss of data at the bottom of the part which can be corrected with a repositioning of the part or a rescan of just that small area.

Figure 4-29 Amplitude C-scan images show inclusions.

4.3.4 Pivot Shaft: *Very Thick and Attenuative*

The F-22 includes two large composite (IM7/977-3 Gr/Ep) horizontal stabilizer pivot shafts per ship set. These pivot shafts are approximately 9 feet in length and 9 inches in diameter, cylindrical in shape with one box end. The cylinder is hollow with wall thicknesses that vary from 1.5 inches to 2.5 inches. Fig.4-30 shows a section of a pivot shaft including a photograph and two wave-forms, one from the thick area and one from the thin area. In order for the current system to achieve even this level of signal quality in the thick area, the surface must be sprayed with a strip-pable vinal coating which enhances the generation properties of the surface. This was done purely

134

for testing purposes to measure the system's current capability.
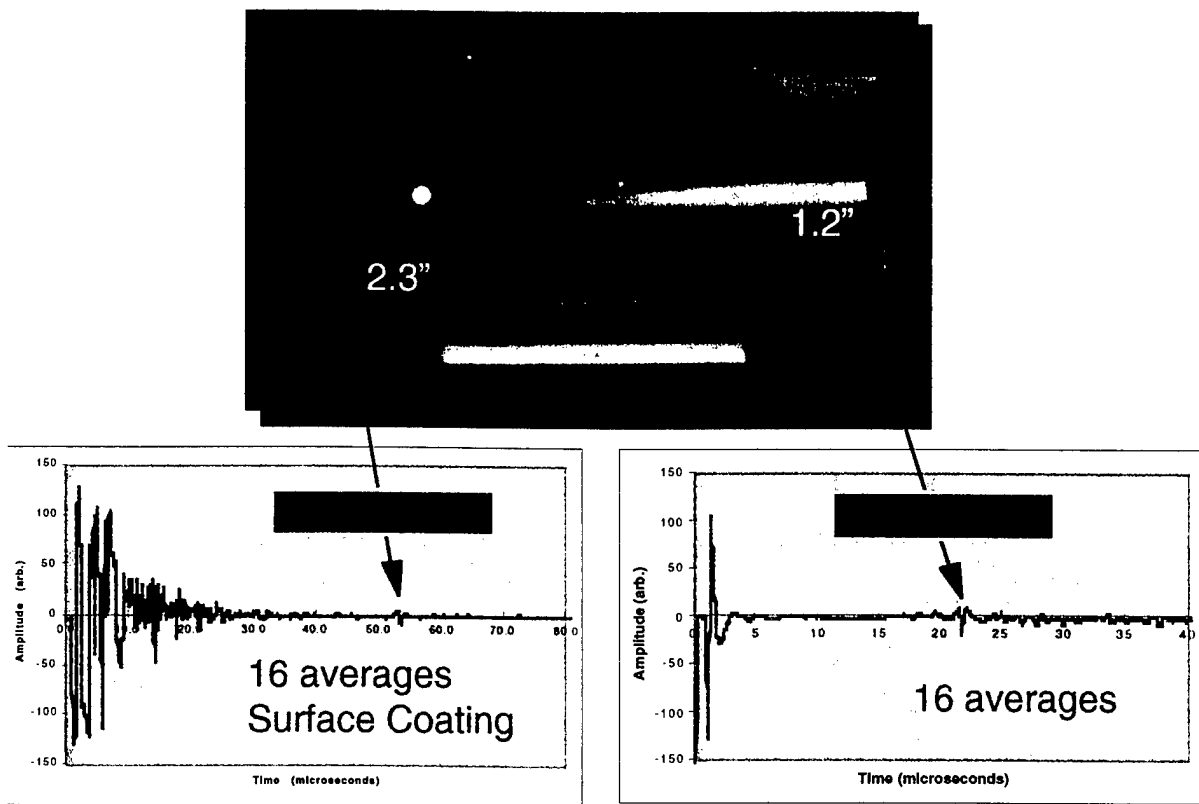
Figure 4-30 Laser UT results from the thick F-22 composite pivot shaft.

4.4 Joint Strike Fighter (JSF)

4.4.1 JSF Composite Inspection Needs: *Low Life-Cycle Cost Fighter*

The Joint Strike Fighter is being designed as the next generation multi-role fighter aircraft for multiple services: Air Force, Navy, and Marines. With multiple configurations, including VTOL and carrier landings, as well as a high percentage of composite structure, affordability in the manufacturing process and low overall life-cycle costs is imperative.

4.4.2 Fiber Placement Component: *Complex Contour and New Technology*

The Joint Strike Fighter (JSF) is planned as the next large aircraft acquisition for the U.S. Military to serve as a joint service multirole aircraft. There goal is to provide a highly capable fighter aircraft with a strong emphasis on affordability and maintainability. In line with these goals, much of the aircraft structure will be made out of composites. Laser Ultrasonics provides a highly affordable and efficient method of rapidly testing composite structures. In addition, it is currently the only automated method of ultrasonic inspection suitable for testing at the fabrication level as well as at the depot level. Figure 4-31 is photo of a JSF fiber-placement skin (Fiberite IM7/977-3) that was tested with the LACIS prototype. Figure 4-32 is an image of two depth c-scans of this part that have been tied together.

Figure 4-31 Photograph of JSF fiber placement skin.
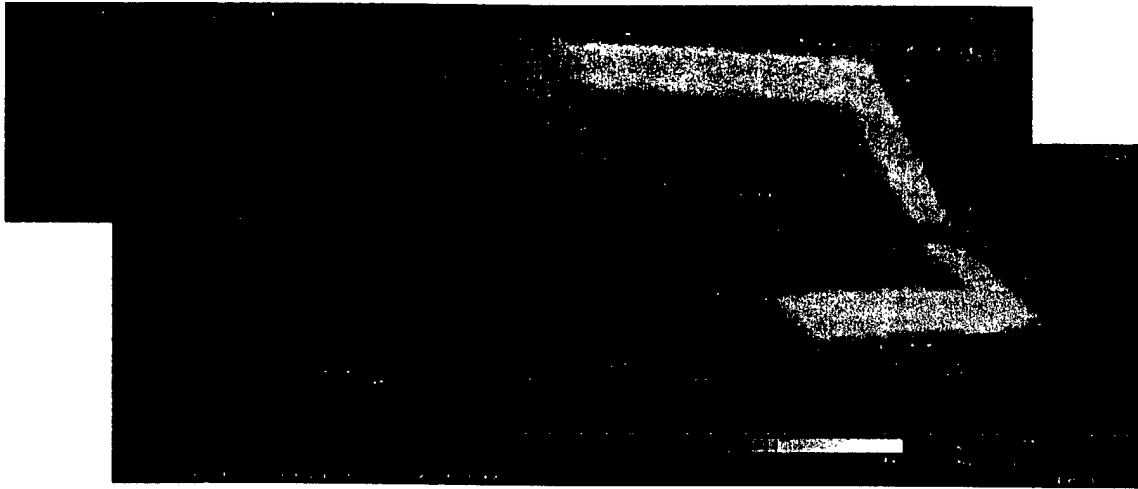
Figure 4-32 Full coverage required two inspections.

4.5 MISCELLANEOUS OTHER TESTS

4.5.1 Inclusion Tests
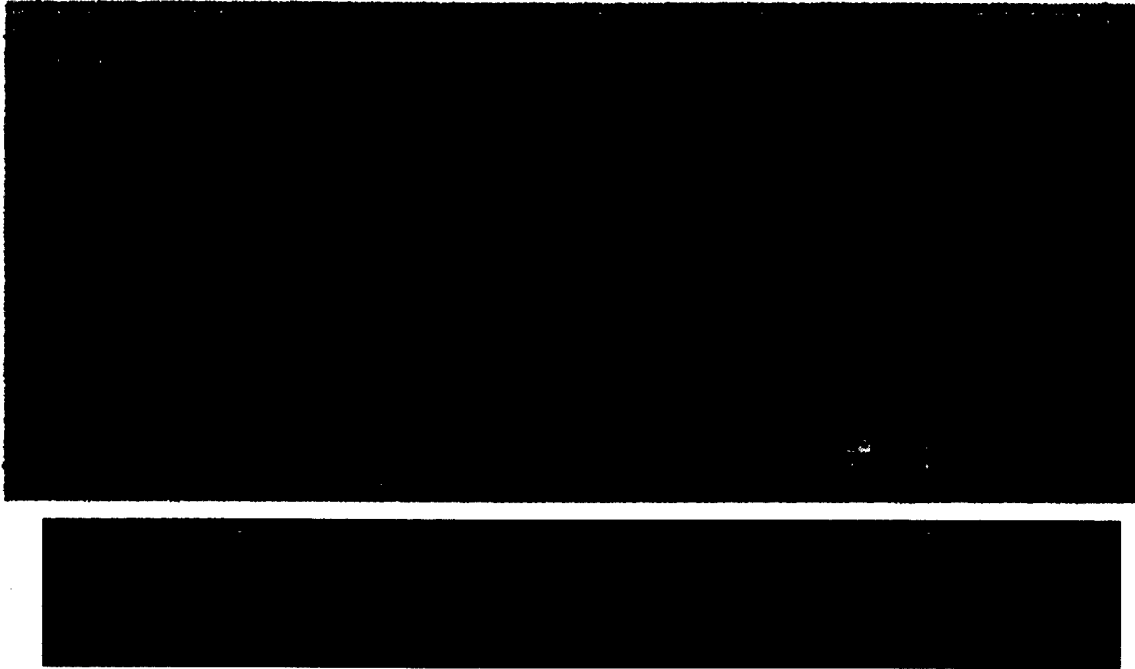
Figure 4-33 All of the inclusions were detected in this Gr/Ep test part.

Material Type: Fiberite HYE1076 Graphite/Epoxy laminate.

Surface Condition: Polyester peel-ply (Airtech release ply G).

Comments: Implanted defects consisting of: backing paper, blue polyethylene film, mylar, teflon, and grafoil. Laminate was B-staged prior to final cure.

4.5.2 Cure-Form Process Frame Component

Figure 4-34 Composite frame produced with the cure-form method.

Material Type: Fiberite IM7/977-3 Graphite/Epoxy laminate.

Surface Condition: 128 weave fiberglass peel-ply.

Comments: Cure-form processed.
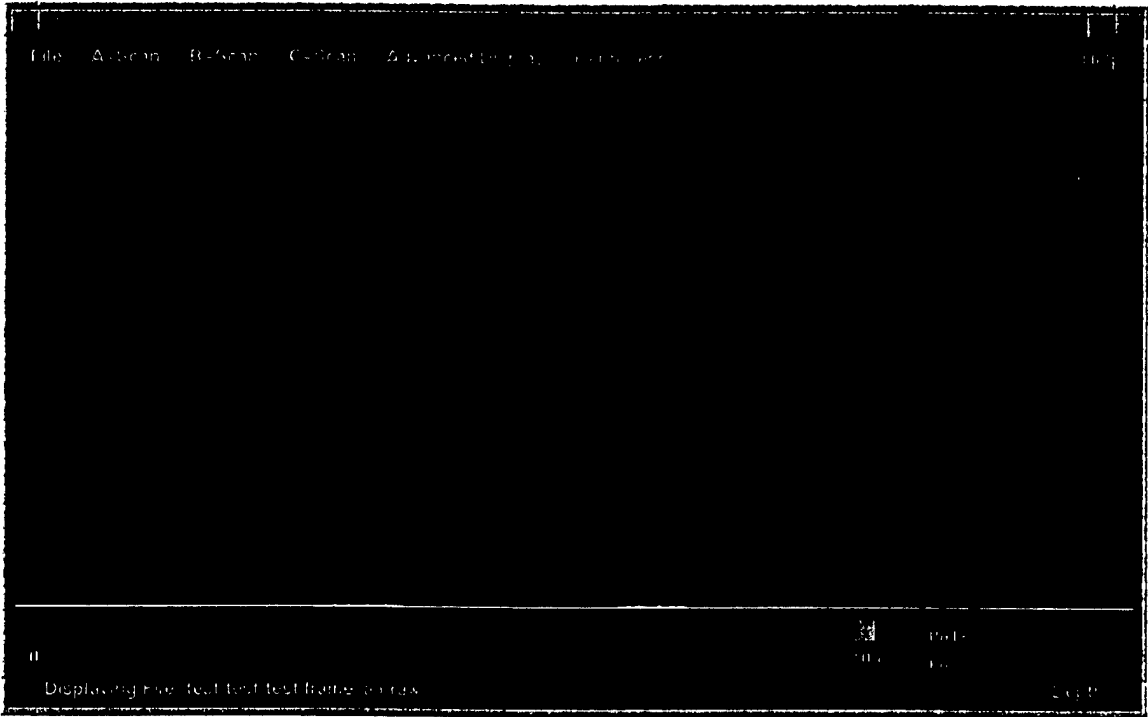
Figure 4-35 Depth C-scan of Cure-Form frame.
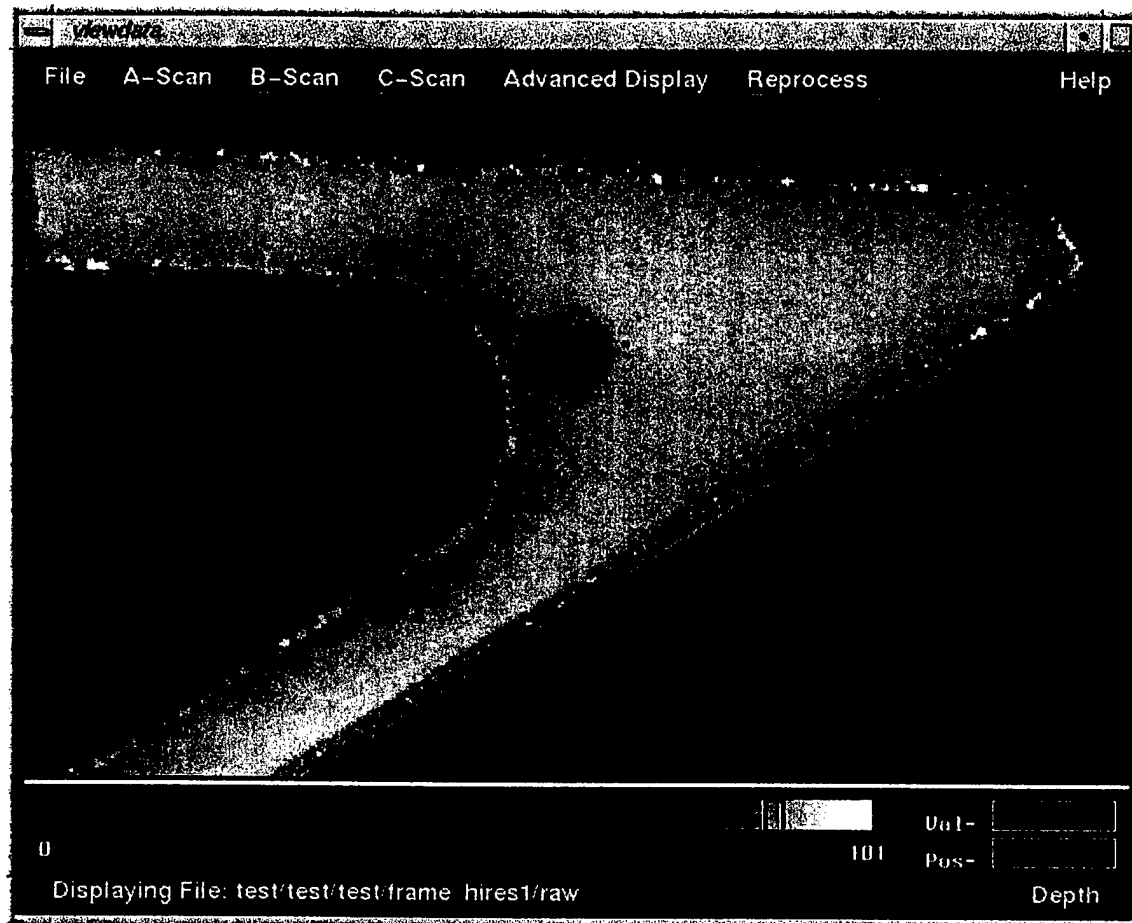
Figure 4-36 High-resolution depth plot of radius area.

4.6 RADII TESTS

4.6.1 YF-22 Composite Frame: *Delaminations in Radius*

B-scan of good radius
(note thinning).

B-scan of a defective radius
(note loss of signal).
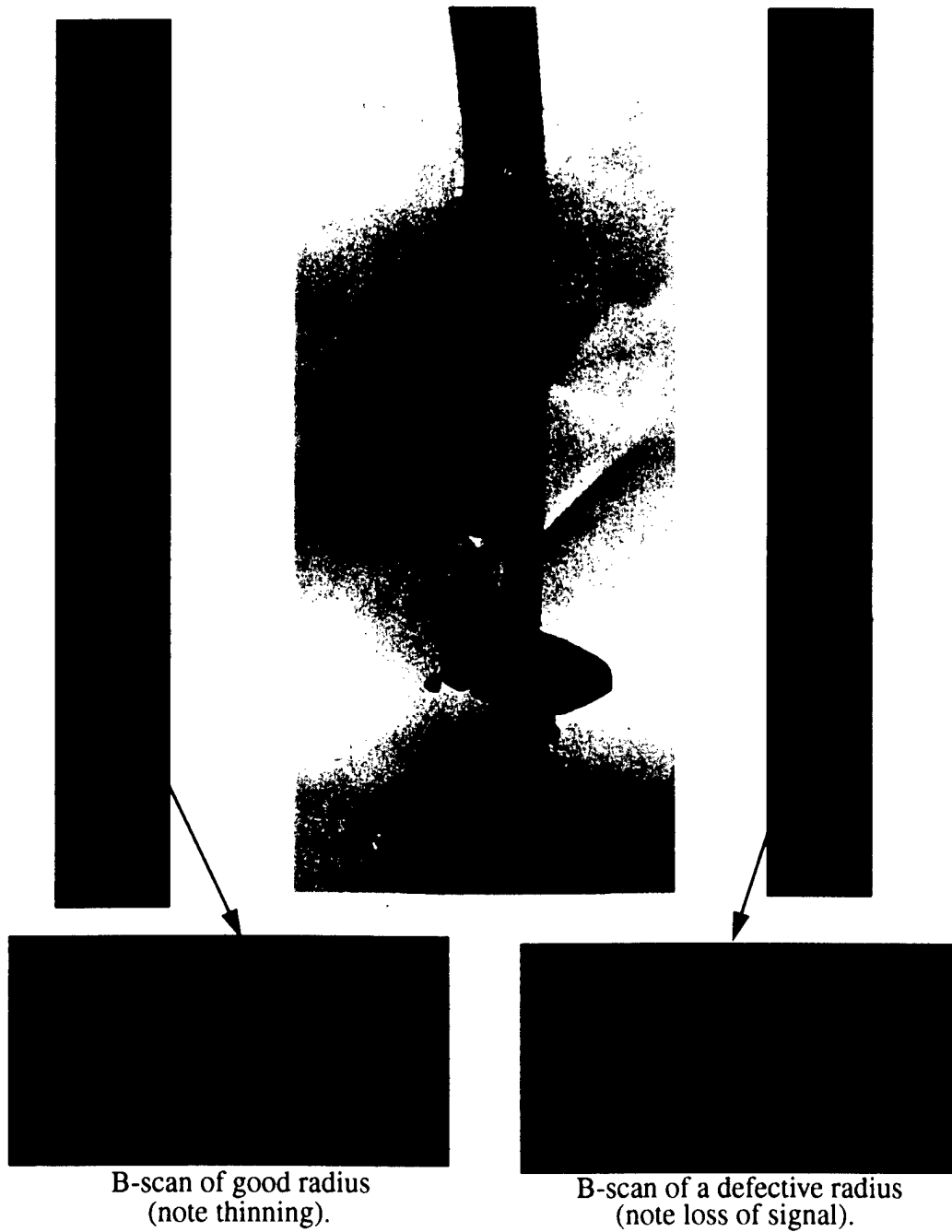
Figure 4-37 Laser UT can inspect tight radii such as this YF-22 spar.

Material Type: Fiberite IM7/977-3 Graphite/Epoxy laminate.

Surface Condition: 128 weave fiberglass peel-ply.

Comments: Delaminations in radius areas.

4.6.2 Hat Stiffener: Thinning in radius areas.

Figure 4-38 This amplitude C-scan shows weak signals in the radius area.

Figure 4-39 B-Scan analysis profiles the thickness reduction in the tight radius.

Material Type: Fiberite IM7/977-3 Graphite/Epoxy laminate.

Surface Condition: 128 weave fiberglass pee-ply.

Comments: Thinning of laminate in the radius areas during processing.
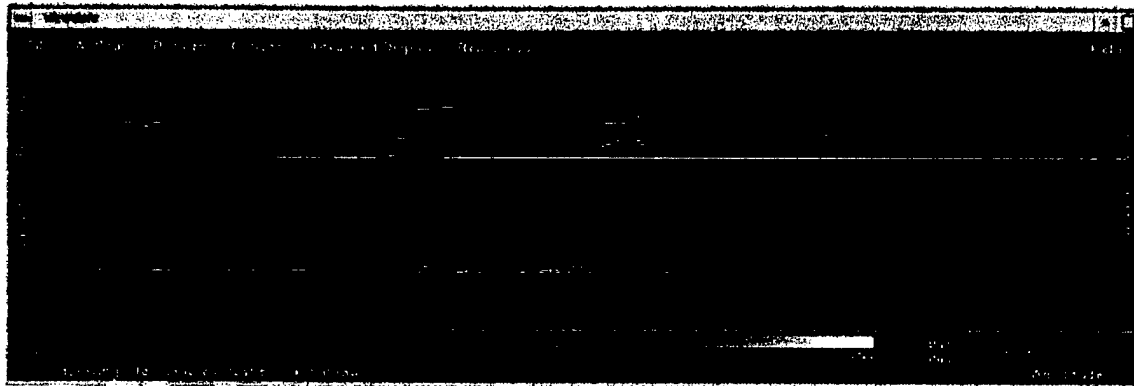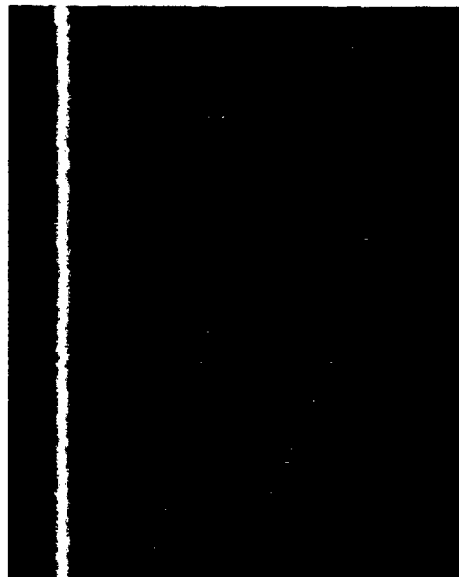
4.7 RADAR ABSORBING MATERIAL TESTING

4.7.1 Introduction to problem

Radar absorbing material (RAM) is commonly used at various locations on a modern fighter air-craft. Ultrasonically, the material is typically very attenuative, especially to high frequency components. This makes ultrasonic testing of composite or metallic structure beneath RAM coatings difficult in the manufacturing process but especially in-service. In service, the inspector will have only single-sided access to a often complex shaped structure, making Laser UT the perfect auto-mated ultrasonic test for these applications. Typical in-service testing of problem areas often includes stripping off of the RAM coating, performing the ultrasonic inspection, and then reapplying the RAM coating. These procedures are very time consuming and costly. An automated in-service ultrasonic test with Laser UT would be an ideal solution and would dramatically reduce inspection costs at the depot level. The following tests were performed to obtain a baseline for testing of composite structure under RAM coatings using Laser UT.

4.7.2 RAM Coated Composite: *Highly Attenuative Material*

Two test panels with implanted defects were inspected as part of another Wright Labs program, Nondestructive Evaluation (NDE) for Stealth Affordability, Contract# F33615-95-C-5222 and in conjunction with this program. One panel was IM7/5250-4 Graphite/BMI and one was IM7/977-3 Graphite/Epoxy. Material implants included Grafoil, McDonnell Douglas A3000, 2 mill thick Teflon, Bell Textron Tedlar, and 10 mil thick Blue Poly (polyethylene film). The implants were of two different diameters, 1/4 inch and 1/2 inch, placed at several different depths in the material. Both panels were inspected at three different stages to test for sensitivity differences caused by surface condition: 1) prior to RAM application as a baseline, 2) after RAM application, and 3) after topcoat (paint) application. Only the BMI panel is reported here. Results from the Epoxy panel are very similar. Figure 4-40 shows an amplitude c-scan image extracted from the laser

ultrasonic data of the Graphite/BMI panel prior to RAM application. Note that all implants are clearly discernible.
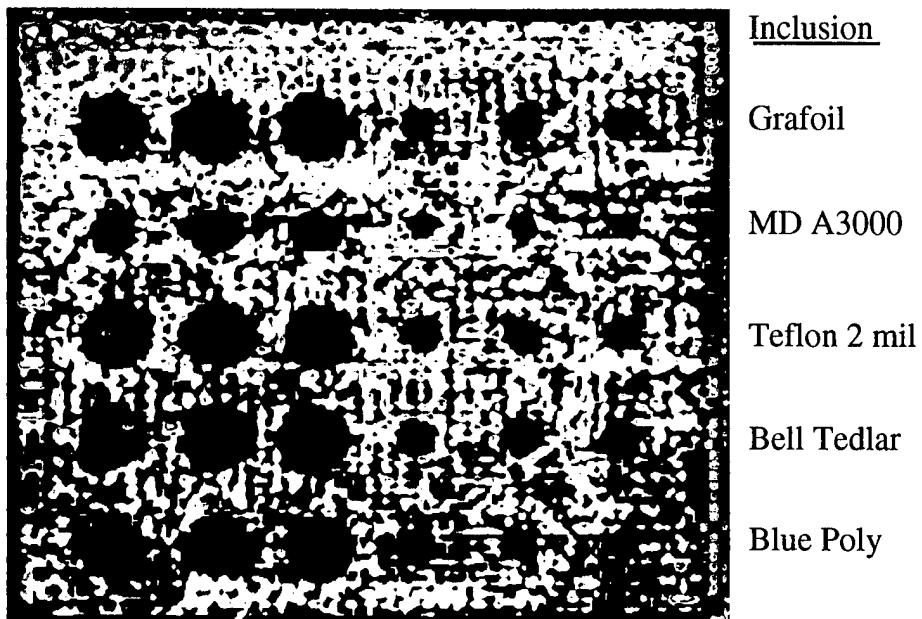
Figure 4-40 BMI Test Panel Prior to RAM Application.

Figure 4-41 shows an amplitude c-scan image extracted from the laser ultrasonic data of the Graphite/BMI panel after RAM application.

Inclusion

Grafoil

MD A3000

Teflon 2 mil

Bell Tedlar

Blue Poly

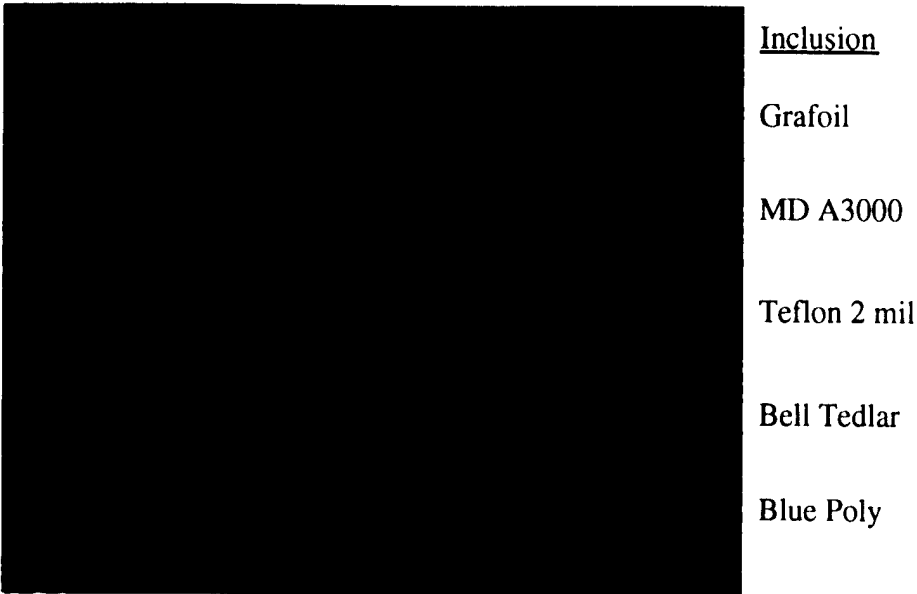**Figure 4-41 BMI Test Panel After RAM Application.**

Figure 4-42 shows an amplitude c-scan image of the BMI test panel after topcoat application. Note the enhanced sensitivity to defects due to the improved absorption of the generation laser in the topcoat.

Inclusion

Grafoil

MD A3000

Teflon 2 mil

Bell Tedlar

Blue Poly

Figure 4-42 BMI/RAM test panel after topcoat application.

5.0 APPENDIX

5.1 Large Aperture Collector Design Data

```
GENERAL LENS DATA:

File Name                 : LAC6-23
Lens Title                : LARGE APERTURE COLLECTOR
Number of surfaces        :              6
Effective Focal Length :          280.7097
System Aperture Type      : Entrance Pupil Diameter
Image Space F/#           :          0.935699
Working F/#               :          1.309672
Object Space N.A.         :        0.03995322
Entrance Pupil Diameter:               300
Entrance Pupil Position:          251.3932
Exit Pupil Diameter       :          87.46116
Exit Pupil Position       :         -109.7405
Total Track               :          251.3932
Paraxial Magnification :         -0.1006657
Paraxial Image Height     :          1.006657
Primary Wavelength        :              1.064 microns
Stop Surface              :              2
Units                     : Millimeters

Defined Fields            : 4
Field number 1            : 0.00, 0.00 mm  weight:   1.000
Field number 2            : 0.00, 2.00 mm  weight:   1.000
Field number 3            : 0.00, 5.00 mm  weight:   1.000
Field number 4            : 0.00, 10.00 mm  weight:   1.000

Defined Wavelengths       : 1
Wavelength Number 1       :   1.064 microns    1.000 weight
```

SURFACE DATA SUMMARY:

Surf		Type	Radius	Thickness	Glass	Diameter	Conic
OBJ	STANDARD		Infinity	3500		20	0
1	STANDARD		Infinity	251.3932		281.2363	0
STO	STANDARD		-518.5757	-251.3932	MIRROR	298.3883	-0.7072915
3	COORDBRK		--------	0		0	--------
4	STANDARD		-206.9	36.44998	MIRROR	31.98328	-34.90439
5	STANDARD		Infinity	0		2.446021	0
IMA	STANDARD		Infinity	0		2.446021	0

```
SURFACE DATA DETAIL:

Surface    1      : STANDARD
 Aperture         : Circular Obscuration
 Minimum Radius :              0
 Maximum Radius :             25
Surface    3      : COORDBRK
```

```
Decenter X      :           0
Decenter Y      :           0
Tilt About X    :           0
Tilt About Y    :           0
Tilt About Z    :           0
Surface   5     : STANDARD
 Aperture       : Circular Aperture
 Minimum Radius :           0
 Maximum Radius :           1
```

MULTI-CONFIGURATION DATA:

```
Configuration   1:
Thickness   0 :           1800   Object distance
Thickness   4 :        80.09905  Focal position from the secondary


Configuration   2:
Thickness   0 :           1900
Thickness   4 :        74.50766


Configuration   3:
Thickness   0 :           2000
Thickness   4 :        69.71825


Configuration   4:
Thickness   0 :           2100
Thickness   4 :        65.43497


Configuration   5:
Thickness   0 :           2200
Thickness   4 :        61.71987


Configuration   6:
Thickness   0 :           2300
Thickness   4 :         58.4284


Configuration   7:
Thickness   0 :           2400
Thickness   4 :        55.49333


Configuration   8:
Thickness   0 :           2500
Thickness   4 :        52.86081


Configuration   9:
Thickness   0 :           2600
Thickness   4 :        50.48726


Configuration  10:
Thickness   0 :           2700
Thickness   4 :        48.33785


Configuration  11:
Thickness   0 :           2800
```

```
Thickness    4 :      46.38051

Configuration  12:
Thickness    0 :         2900
Thickness    4 :      44.59261

Configuration  13:
Thickness    0 :         3000
Thickness    4 :      42.95849

Configuration  14:
Thickness    0 :         3100
Thickness    4 :      41.44362

Configuration  15:
Thickness    0 :         3200
Thickness    4 :      40.05123

Configuration  16:
Thickness    0 :         3300
Thickness    4 :       38.7612

Configuration  17:
Thickness    0 :         3400
Thickness    4 :      37.56403

Configuration  18:
Thickness    0 :         3500
Thickness    4 :      36.44998
```

SOLVE AND VARIABLE DATA:

```
Thickness of   1   : Variable
Curvature of   2   : Variable
Thickness of   2   : Solve, pick up value from 1, scaled by -1.00000
Conic of   2       : Variable
Curvature of   4   : Variable
Conic of   4       : Variable
```

INDEX OF REFRACTION DATA:

```
Surf      Glass      1.064000
  0                 1.00000000
  1                 1.00000000
  2     MIRROR      1.00000000
  3                 1.00000000
  4     MIRROR      1.00000000
  5                 1.00000000
  6                 1.00000000
```

GLOBAL VERTEX COORDINATES AND DIRECTIONS:

```
Surf      X coord      Y coord      Z coord      X direc    Y direc    Z direc
  1      0.000000     0.000000   3500.000000   0.000000   0.000000   1.000000
```

2	0.000000	0.000000	3751.393228	0.000000	0.000000	1.000000
3	0.000000	0.000000	3500.000000	0.000000	0.000000	1.000000
4	0.000000	0.000000	3500.000000	0.000000	0.000000	1.000000
5	0.000000	0.000000	3536.449979	0.000000	0.000000	1.000000
6	0.000000	0.000000	3536.449979	0.000000	0.000000	1.000000

ELEMENT VOLUME DATA:

Units are cubic cm.
Values are only accurate for plane and spherical surfaces.

5.2 Interferometer Response Measurement

The performance of the confocal Fabry-Perot was tested using an improved technique to compare measured results with theoretical predictions. These tests were performed after the completion of section 3.2.5.6 and are provided here as an Appendix to previous results.

The vibrating mirror technique discussed in Section 3.2.5.6 was inadequate for absolute measurement of the interferometer sensitivity due to the resonance of the transducer. This undesirable resonance caused large ambiguities in the exact surface displacement calibration procedure. Instead, an optical phase modulator was used to produce a precise signal on the laser beam as shown below. This device was calibrated to produced 180 degrees of phase modulation at 1064 nm for a drive voltage of 210V. For the test results shown, the modulator was driven with a power of 0 dBm into 50-ohms (this is about 0.4 nm of equivalent surface displacement). The modulator did suffer from some acoustical resonance at select frequencies, but the data is still considerably better than that obtained with the vibrating mirror. The detector response function was measured and normalized out of the data shown. All of the plots are in absolute scale with 0 dB representing the maximum obtainable sensitivity for any optical detection process.
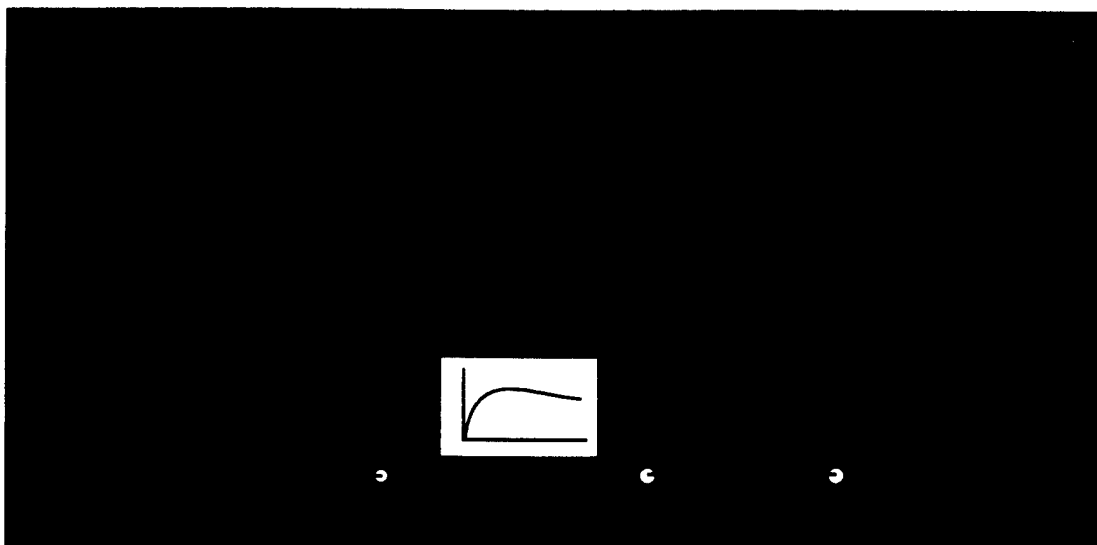

Figure 5-1 Test setup using an optical phase modulator to measure sensitivity.

The response function was measured using the following relationship for the time-varying component produced by a generalized optical detection process of a phase modulated input

$$V_{signal} = Gain \cdot V_{dc} \cdot (2ku) \cdot S \tag{5.2.0-1}$$

where the Gain term denotes the fact that our detectors had a 6x gain at ultrasonic frequencies compared to the DC-level (due to T-feedback construction), k is the usual wavevector, u is the ultrasonic surface displacement, and S is the response function. It is assumed that u is small compared to the measurement wavelength.

Next substituting the phase modulator for the vibrating surface we get the following relationship between the drive voltage and the depth of modulation.

$$2ku = \Delta\phi = \frac{V_\phi}{210} \cdot \pi \tag{5.2.0-2}$$

The response function, S, can now be measured using the following equation.

$$S = \frac{V_{signal} \cdot 210}{Gain \cdot V_{dc} \cdot V_\phi \cdot \pi} \tag{5.2.0-3}$$

Note that a response magnitude of S=1 (or 0 dB) denotes a perfect response function that represents the maximum obtainable sensitivity. A Michelson interferometer operated at balanced quadrature will have S=1 for all frequencies.

This is the preferred way to compare various interferometer designs. The light gathering power of the interferometer should be separated out to provide a clear distinction between sensitivity and SNR performance.

The measured detector response showed that the design goal of a flat response (to 1 dB) was obtained from 1 to 10 MHz. For frequencies out of this band the detector response must be normalized out of the interferometer response function. A typical response curve is shown below.
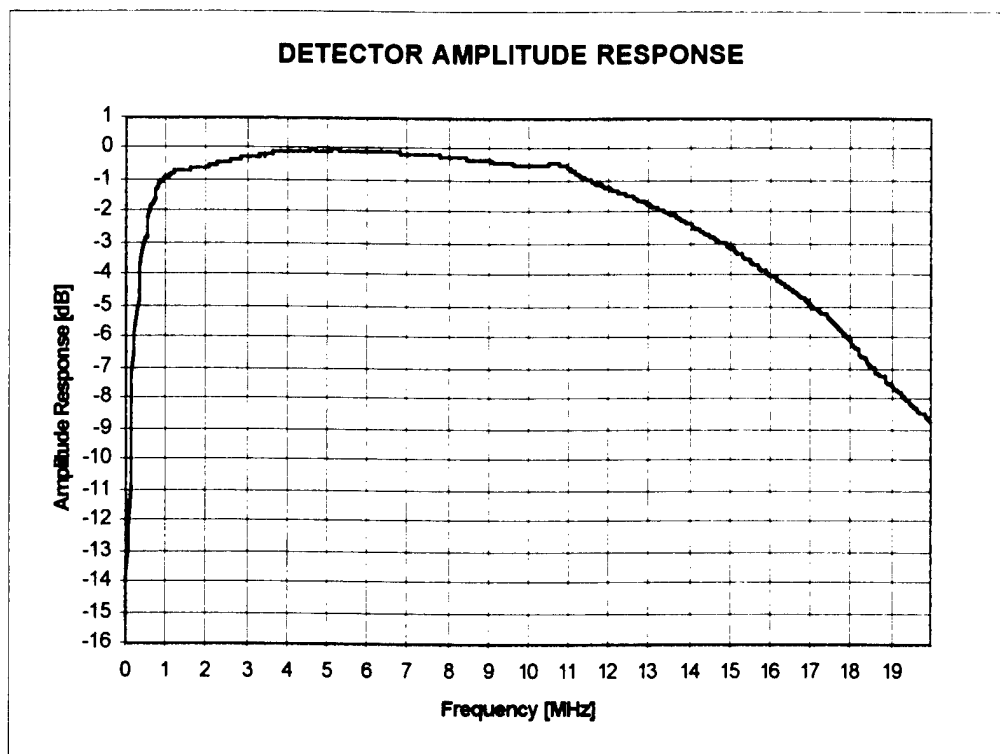
DETECTOR AMPLITUDE RESPONSE

Figure 5-2 EG&G YAG100 detector with T-feedback response curve.

The interferometer analyzed was a 1-meter CFP with 93% mirrors (they were specified as 95% but measured only 93%). Note that for frequencies above 3MHz the magnitude response agreement is to better than 1 dB. At lower frequencies the magnitude response predictions was in error by as much as 3-4 dB. This was explained by the fact that the interferometer was over filled and the etendue was exceeded. A check of the finesse verified this fact and indicated a DC-level equivalent to 90% mirrors. A curve fit for 90% mirrors matches the measured data to better than 1 dB.
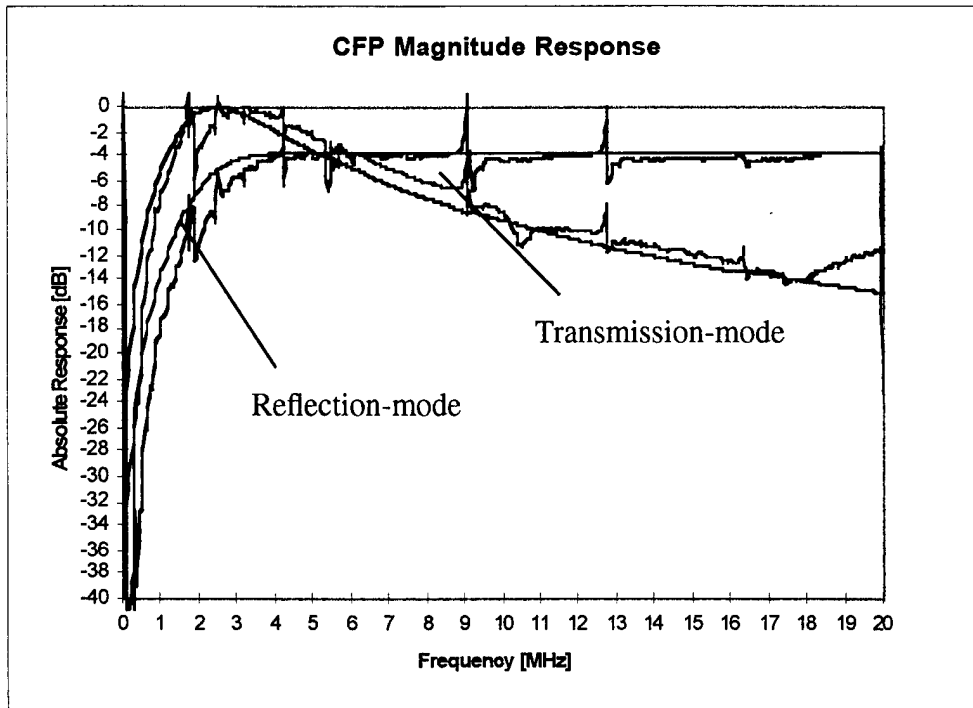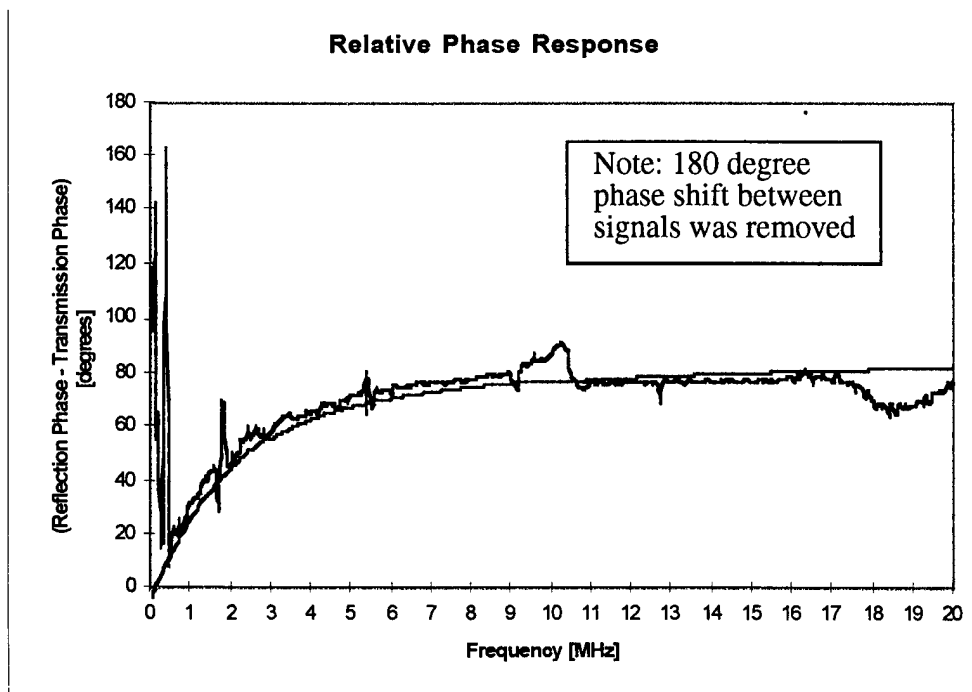
Figure 5-3 Measured and theoretical magnitude response.

Figure 5-4 Measured and theoretical phase response.

155

The finesse for a CFP is given as:

$$F = \frac{\pi R}{1 - R^2}.$$

(5.2.0-1)

As the mirror refelectivirt, R, approaches unity we find:

$$F \approx \frac{\pi}{2(1 - R)}.$$

(5.2.0-2)

Working backwards from the resonance curve shown below we find that the measured fineese represents a mirror reflectivity of about 90% to 91%. Thus, operating the CFP beyond the etendue limits did reduce the low-frequency performance of the system. The solution for improved low frequency performance is to slightly lower the collection fiber core size to match the etendue of the CFP. Of course the collection efficiency will have a corresponding reduction as well.
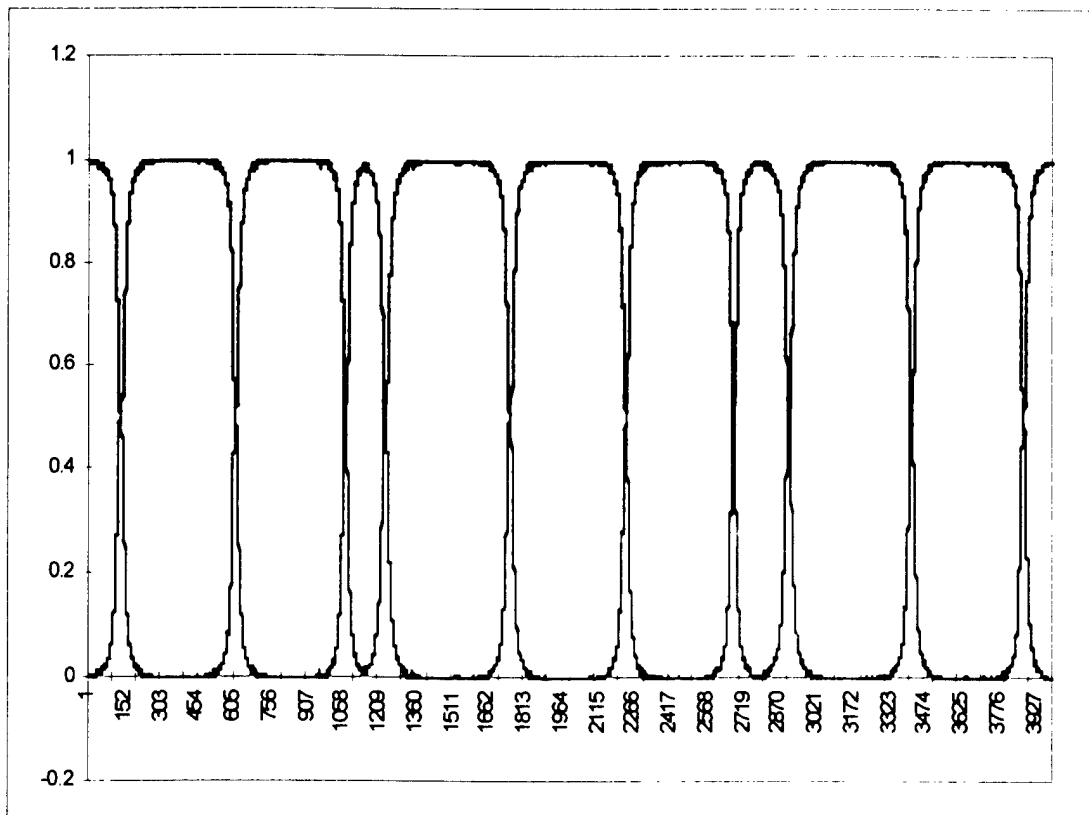

Figure 5-5 Resonance curves for the 1-meter 93% CFP.